Dynamical Quantum Phase Transitions, Scrambling and Quantum Simulations of Many-Body Neutrino Systems

Ramya Bhaskar

A dissertation
submitted in partial fulfillment of the
requirements for the degree of

Doctor of Philosophy

University of Washington

2025

Reading Committee:

Martin J. Savage, Chair

Lukasz Fidkowski

David B. Kaplan

Program Authorized to Offer Degree:
Physics

University of Washington

Abstract

Dynamical Quantum Phase Transitions, Scrambling and Quantum Simulations of Many-Body Neutrino Systems

Ramya Bhaskar

Chair of the Supervisory Committee:
Martin J. Savage
Physics

This dissertation covers three main topics: dynamical quantum phase transitions, the far-from-equilibrium phenomenon of quantum information scrambling, and quantum simulations on both trapped ion and superconducting qubit devices, all in the context of many-body neutrino systems.

For the dynamical quantum phase transitions study in the first chapter, the analysis of Loschmidt echos within dense neutrino systems yields insight into a system's initial state requirements needed to achieve a dynamical quantum phase transition (DQPT). Focus is paid to Loschmidt echo crossing distributions, which confirm the presence of two distinct classes of DQPTs in two-flavor neutrino systems. Further analysis reveals a nontrivial dependence on the coupling angle distributions chosen for the two-body interaction term. The results establish two distinct classes of DQPT's in two flavor neutrino systems, verfied via robust statistics.

Scrambling as diagnosed by the Out-of-Time-Ordered Correlator (OTOC) has been demonstrated in the Sachdev-Ye-Kitaev model, Transverse Field Ising Model, the transverse axial next nearest neighbor Ising model among many others. However they have yet to be characterized in many-body neutrino systems. Such systems are often modeled as all-to-all connected random-Heisenberg spin chains.

In the second chapter, this work demonstrates numerical evidence for scrambling's oc-

currence in two-flavor many-body neutrino systems. The results demonstrate dynamical quantum phase transitions (DQPTs) potential role as a witness for scrambling in many-body neutrino systems. We see what appears to be discreet modes of scrambling times corresponding to a system's first DQPT occurrence. We attempt to formulate an analytical argument resting on the concept of weak measurement schemes to explain how the DQPTs can serve as a witness for OTOCs in families of random-coupled two-flavor many-body neutrino systems in the forward scattering limit.

In the last chapter, quantum circuits for three flavor many body neutrino systems are constructed, for both qubit and qutrit devices. The qubit-based circuits are run on superconducting qubit devices with heavy-hex connectivity and trapped ion devices with all-to-all connectivity, demonstrating the one of the first quantum simulations of three flavor neutrino systems on two level devices. This work demonstrates a proof of principle for simulating three-flavor neutrino systems on two-level devices, the performance of the qubit circuits on each device, and calculation of physical observables off of the device.

TABLE OF CONTENTS

Page

LIST OF FIGURES

Figure Number Page

LIST OF TABLES

ACKNOWLEDGMENTS

Life is a series of bets and a PhD is a big one, stakes being: that you'll still love what you do after over half a decade, that others see value in it too, & that you'll find your way despite the multitude of forces that can peel you off-path. Over the course of this degree both the University of Washington (UW) and the InQubator for Quantum Simulation (IQuS) have provided uniquely stimulating environments where I was able to evolve into something significantly different than what I came in as.

I have sincere gratitude for my primary advisor, Martin J. Savage, whose advising and mentorship enabled me to grow scientifically so much during my graduate career. You allowed me to play at my own pace, gave me the great gift of a self-directed education, and pushed me to forge an ambitious path driven by independent scientific contributions. A piece of advice which I have come to really value has been your encouragement that I be my own person; coupled with the scientific latitude you gave me, this helped me shape my voice as an emerging theorist. While some of our most technical and scientifically speculative conversations remain unwritten, they helped define my approach to physics, gave me the confidence to build my own ideas, and instilled a lasting excitement for our field.

To the following out-of-ordered incomplete list, I'd like to thank: David B. Kaplan for his persistent advocacy for my education, nurturing my budding interest in quantum information scrambling after my first reading course with Martin, and serving as a role-model throughout my PhD, Alessandro Roggero for his critical mentorship early on, opening the door into many-body quantum dynamics & dynamical quantum phase transitions and sparking my rogue interest in tensor networks back in my third year, Natalie Klco for encouraging me to follow my curiosity and entertaining abstract questions, Jason Detwiler, Niklas Mueller, Ann Nelson & Kenneth Roche for their warm support, and Silas Beane, Lukasz Fidkowski, Kai-Mei Fu, Shih-Chieh Hsu, Charles Marcus, Miguel Morales, Duff Neill, Ermal

Rrapaj, Jessica Werk, Nathan Wiebe & Larry Yaffe for their thought-partnering at various stages throughout my PhD. I'm thankful of my reading committee, (David B. Kaplan, Lukasz Fidkowski, Martin J. Savage) for their feedback in the construction of this thesis, and to my general & defense committees (Silas Beane, Jason Detwiler, Miguel Morales & Jessica Werk). This all began with my kind undergrad mentors (John S. Conway, Benjamin D. Shaw, David M. Wittman) who ignited my passion for physics, neural networks, computer vision, and encouraged grad school. Benjamin in particular: thank you for prodding me to take my nascent interest in quantum computing seriously.

After over a year of remote work, it was energizing to return to campus with Niklas Mueller, Hersh Singh, Francesco Turro, Xioajun Yao, Anthony Ciavarella, Ivan Chernyshev, Fabio Anza, Roland Farell, Henry Froland, Jeremy Hartse, Marc Illa, Zhiyao Li, Sarah Powell, Nikita Zemlevskiy & everyone else I had the privilege of sharing IQuS office space with. All of the IQuS, Institute for Nuclear Theory (INT), Los Alamost National Laboratories (LANL) postdocs I crossed paths with over the years (Hersh Singh, Joshua D. Martin, Yukari Yamauchi, Scott Lawrence & others) contributed non-trivially to my professional development. The eye-opening IQuS & INT workshops lead by the various capable and accomplished organizers objectively upgraded my education. Administratively, Megan Baunsgard, Alexis Hall, Katie Hennessy, Paris Nguyen & Catherine Provost all made the administrative complexities of a PhD much less painful.

The Office of Graduate Student Equity & Excellence (GSEE) team—especially Kayla Newcomer & Fernando Puga—provided me with critical support in making my final internship year possible, and the Research University Alliance team of Chris Mantegna (and her exceptional organizational skills), Julia Parrish & Jane Dolliver enabled me to further expand my horizons. I also greatly appreciated the HYAK staff and operational team for providing much needed HPC computing support as I hurtled towards my deadlines, in particular Kristen Finch, Kaichen Xie, and Seunguk Shin. I would like to extend thanks also to the International High Performance Computing Summer School's iteration in Kobe, Japan for allowing me to further develop my HPC skillset (in particular Dennis Willsch & Aly

Badran), as well as LANL's Duff Neill for hosting me for an intellectually stimulating visit with Ibrahim Abdurrahman, Chris Lee, Joshua D. Martin & Ingo Tews all enhancing my stay and broadening my scientific field of view.

During my last year, I had the fantastic opportunity to split my time as a Quantum Information Science R&D intern at Sandia National Laboratories. The unique immersion scaled-up my field view of quantum computing and gave me new perspectives I didn't have access to otherwise. I am grateful to my knowledgeable mentor Andrew Zhao and his willingness to pursue ambitious projects, my manager Janine Bennet for her level-headed support, staff scientists Andrew Landahl (and his friendly group at large), Riley Chien, Alicia Magann, Max Porter, Antonio E. Russo, Mohan Sarovar and the broader Quantum Algorithms and Applications Collaboratory (QuAAC) team for providing a welcoming environment abundant with mentorship and creativity.

My love for science was further amplified because of my family, friends & loved ones, including: Bethany Baldwin-Pulcini who's stuck by me since we were physics undergrads, childhood & undergrad friends Jennifer Stevens, Ted Studley, Alejandra Martín, Kristina Mardinian, Bobby Girardi, Arianna & Chris Huppertz for believing in me, and Ian Docherty for his love, support & reminding me to not just study nature but play in it as well. I'm indebted to Natalie Klco for wholeheartedly welcoming me into theoretical physics, Anthony Ciavarella, Francesco Turro & Jesse Stryker for humor & new reference frames, as well as Mariya Bashkatova, Marcelene Bonilla, Drew Byron, Ruby Byrne, Jeffery Commons, Chloe Huber, Arnab Manna, Ian McConachie, Zach Montague, James Scargill, Sydney Ward, Wan Jin Yeo & everyone else whom I couldn't fit, for their positive influence. There is no better place for completing a doctoral degree than the Pacific Northwest; all of the biking, skiing, sailing, paddleboarding, and beautiful weddings helped offset the intensity of a PhD. The staff at Eastlake Coffee, Copper Tree, and Pete's—Steven, Jae, Lisa, Casey, Emma Howeiler, Serena Young—fueled the hard writing days.

Lastly, to my parents who I love very dearly: thank you for encouraging me to pursue my dreams with full force. Despite the many barriers you both have faced, you instilled a

deep respect for education, teaching me that the pursuit of knowledge requires a nontrivial amount of bravery & humility in a world where it is not readily accessible for all. That theme has followed me throughout my studies, motivating me to give space to ideas that are both unfamiliar and uncomfortable, and has allowed me to experience education as the deeply transformative force it is.

The work presented in this thesis was financially supported in part by U.S. Department of Energy, Office of Science, Office of Nuclear Physics, InQubator for Quantum Simulation (IQuS) under Award Number DOE (NP) Award DE-SC0020970 via the program on Quantum Horizons: QIS Research and Innovation for Nuclear Science, the Department of Physics, the College of Arts and Sciences, and the Office of Graduate Student Equity & Excellence Awards Program, at the University of Washington. I want to recognize UAW 4121 for providing worker protections and negotiation of employment terms while I was at the University of Washington. Portions of this work were completed on Hyak, University of Washington's high performance computing cluster. This resource was funded by a University of Washington student technology fee grant to the Research Computing Club.

DEDICATION

to my family, friends, and anyone who reads this!

Chapter 1

INTRODUCTION

1.1 Neutrino Fundamentals & Background

For almost a century neutrinos have been of significant interest to the physics community since they were first proposed by Wolfgang Pauli for their modulating role in beta decay in the 1930's. Highly energetic, and with near-zero mass, neutrinos are the most notoriously elusive particles within the Standard Model (SM) to experimentally observe yet are one of the most abundant particles in the universe. Interest in the nature of neutrinos grew rapidly after experimental verification of their existence in the 1950's. Then, through a laboratory demonstration of neutrino's helicity (*handedness*), the chirality of one of the four fundamental forces–weak interactions–was discerned [4].

Soon after, as a solution the long-standing disparity between the number of ν_e predicted to be observed by standard solar models and the smaller, solar-originated, incoming ν_e flux measured on Earth in the 1960's (this disparity is known as the solar neutrino problem), a unitary object known as the Pontecorvo–Maki–Nakagawa–Sakata (PMNS) neutrino-mass mixing matrix was developed. PMNS matrix bridged the neutrino's mass eigenbasis to the flavor eigenbasis, the first formal tool articulating the process of a neutrino fluctuating between its three flavor eigenstates ν_i, $i = \tau, e, \mu$, a process called neutrino flavor mixing, and was later validated by the experimental measurement of neutrinos' very small, yet nonzero mass. Flavor evolution at low neutrino densities was robustly confirmed by ground-based experiments [5], first by the Super Kamiokande Collaboration [6].

Solar neutrinos' adiabatic flavor evolution was then established by ground-based experiments such as the the Sudbury Neutrino Observatory (SNO) [7, 8], a pivotal experiment which also determined the interesting phenomena that neutrinos can exist as a *mix* between their possible flavor eigenstates. Such large-scale operations witnessing their flavor oscillations further motivated the growing interest in their fundamental nature, particu-

larly because the measured phenomena of non-zero mass and flavor oscillations lay beyond Standard Model (SM) predictions.

With each experimental breakthrough, from discovery of each neutrino flavor (and existence of antineutrinos) to demonstrating flavor oscillation, the astrophysics, high-energy and related physics communities have expanded their understanding of the neutrino's pervasive role across a wide spectrum of physical processes. Large-scale stellar astrophysical dynamics–such as CCSN explosion dynamics[9], big-bang nucleosynthesis, gamma-ray bursts, nucleosynthesis, and galactic structure formation–involve a general theme of neutrinos serving as vehicles for physical observables such as energy and entropy. Beyond large-scale dynamics, neutrinos also play significant roles in determining the leptonic asymmetry of the universe and are a strong candidate for probing beyond SM physics.

We are particularly focused on large-scale dynamics and how neutrinos' fundamental ability to oscillate between flavor eigenstates can influence late-time entanglement structure and entropy generation in many-body systems. This has potential consequences for how much energy is transported via outgoing neutrinos in highly energetic environments such as CCSN, and can drastically change the outcomes of large-scale highly energetic astrophysical phenomena. Additionally, for simplicity, this introduction will first focus on the two-flavor approximation, which assumes two potential flavor eigenstates, $|\nu_e\rangle, |\nu_x = \nu_{\tau+\mu}\rangle$ (a simplification which is defended in the next section), before generalizing to the three-flavor neutrino model (possible flavor eigenstates being $|\nu_e\rangle, |\nu_\tau\rangle, |\nu_\mu\rangle$). We then dwell on the computational framework known as Tensor Networks, and its role in high-energy and nuclear physics studies, before arriving at the many-body neutrino system (MBνS) dynamics of interest to us.

1.2 The Two-Flavored Neutrino Hamiltonian

The Hamiltonian governing the behavior of N neutrinos in the two-flavored model consists of the three known forward interactions that each neutrino can possibly undergo at any time (see Refs. [10, 11] for a derivation). This is the forward scattering effective Hamiltonian, which is a subset of the SM Hamiltonian. The first is the vacuum oscillation interaction, where a single neutrino undergoes spontaneous mass-mixing between the three

possible flavors it can have, as a result of simply transiting through the vacuum. The second interaction is the neutrino-matter interaction, and the third is the neutrino-neutrino self-interaction term.

1.2.1 Neutrino-Vacuum Interaction

Before fully expounding on the vacuum oscillation effect, it is useful to first briefly consider a rather special quantity previously unanticipated by the SM: the neutrino flavor mixing angle θ_{mix}. The quantity θ_{mix} is a measurable physical observable connecting the mass eigenstates ν_1, ν_2, ν_3 to the flavor eigenstates ν_e, ν_μ, ν_τ, with three mixing angles for the three possible transitions: $\theta_{12}, \theta_{23}, \theta_{13}$. Prior to theoretical predictions of the PMNS matrix and successful measurements of θ_{mix}, it was assumed that only the weak interactions between quarks necessitated representation via a mixing matrix–specifically the Cabibbo-Kobayashi-Maskawa (CKM) matrix; the development and experimental confirmation of the PMNS matrix thus illustrated an important step in the field's understanding of beyond-SM lepton behavior.

The two-flavor approximation is not simply an artifice implemented solely to ease theoretical calculations. Experimental evidence has determined that θ_{13} is significantly smaller than θ_{12} and θ_{23}. The significantly smaller value of the transition probability of $\theta_{13} : \nu_e \to \nu_\mu$ allows us to reasonably approximate a two-flavor model, and effectively account for both channels $\nu_e \to \nu_\mu$ and $\nu_e \to \nu_\tau$ as one channel $\nu_e \to \nu_{x\approx\mu}$. The two-flavor mixing dynamics are described by the following transformation, when assuming an initial pure state:

$$\begin{pmatrix} \nu_e \\ \nu_{x\approx\mu} \end{pmatrix} = \begin{pmatrix} \cos\theta_{mix} & \sin\theta_{mix} \\ -\sin\theta_{mix} & \cos\theta_{mix} \end{pmatrix} \begin{pmatrix} \nu_1 \\ \nu_{23\approx 2} \end{pmatrix} \tag{1.1}$$

where $\theta_{mix} = \theta_{12}$ [12].

Before proceeding to incorporate the vacuum interaction into a Hamiltonian governing the interactions of N individual neutrinos, it would be useful to make explicit the probability of flavor oscillation in the flavor basis, as manifestation of this quantity introduces important sub-quantities which appear in the vacuum oscillation term. Via the Schrödinger equation any flavor or mass eigenstate evolves as: $|\nu_{\alpha'}(t)\rangle = e^{-iE_\alpha t} |\nu_\alpha(0)\rangle$. Referencing Eq. (1.1),

the probability of $\nu_e \to \nu_\mu$ when traversing a distance L with energy E [13] is then (with U being the amplitude of the particle when traveling across distance L), Above, time has been converted to units of length $L \approx ct$, continuing to adhere to the ultra-relativistic limit.:

$$\begin{aligned} P(\nu_e \to \nu_\mu) &= |U(\nu_e \to \nu_\mu)|^2 \\ &= |\langle \nu_\mu | \nu_e(t) \rangle|^2 \\ &= |(-\sin\theta_{mix} \langle \nu_1| + \cos\theta_{mix} \langle \nu_2|)(e^{-iE_1 t} \cos\theta_{mix} |\nu_1\rangle + e^{-iE_2 t} \sin\theta_{mix} |\nu_2\rangle)|^2 \\ &= \sin\theta_{mix} \cos\theta_{mix} (e^{-iE_1 t} + e^{-iE_2 t}) \\ P(\nu_e \to \nu_\mu) &= \sin^2 2\theta \sin^2(4\sin^2(E_2 - E_1)\frac{L}{2}) \end{aligned} \tag{1.2}$$

Now, when taking the ultra-relativistic limit $p \gg m_1, E \approx p$, where E is the energy for the entire wavepacket, $E_1 = \sqrt{p^2 + m_1^2} = p\sqrt{1 + \frac{m_1^2}{p^2}}$. Enforcing the first condition requires Taylor expanding the root, such that: $E_1 \approx p + p \cdot \frac{m_1^2}{2p^2} = p + \frac{m_1^2}{p^2} \approx E + \frac{m_1^2}{2E}$, where in the last step the second ultra-relativistic condition was enforced. This goes similarly for E_2.

With $E_{1(2)} \approx E + \frac{m_{1(2)}^2}{2E}$, we proceed:

$$\begin{aligned} P(\nu_e \to \nu_\mu) &= \sin^2 2\theta \sin^2(4\sin^2(\frac{m_2^2 - m_1^2}{2E})\frac{L}{2}) \\ P(\nu_e \to \nu_\mu) &= \sin^2 2\theta \sin^2(\frac{\Delta m^2 L}{4E}) \end{aligned} \tag{1.3}$$

The term $\Delta m^2 = m_2^2 - m_1^2$, where m_1 and m_2 correspond to the ν_e's and $\nu_{x \approx \mu}$'s masses respectively, is commonly referred to as the squared neutrino mass difference term.

When articulating the neutrino-vacuum interaction, the neutrino flavor mixing probability can be rendered as a normalized vector $\vec{B} = (\sin(2\theta_{mix}), 0, -\cos(2\theta_{mix}))$. In conjunction with the mass-squared difference term Δm^2 normalized by that particular i^{th} neutrino's energy E_i.

We have still not yet incorporated in the actual neutrino particles themselves; successfully doing so requires introducing the Pauli matrices for any j^{th} particle, which are as follows:

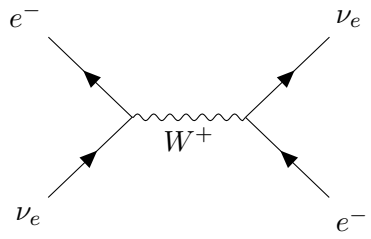

Figure 1.1: W boson mediating a neutrino-electron forward scattering for the neutrino-matter charged current interaction.

$$\sigma_j^x = \begin{pmatrix} 0 & 1 \\ 1 & 0 \end{pmatrix}, \quad \sigma_j^y = \begin{pmatrix} 0 & -i \\ i & 0 \end{pmatrix}, \quad \sigma_j^z = \begin{pmatrix} 1 & 0 \\ 0 & -1 \end{pmatrix}. \tag{1.4}$$

These matrices are closely related to the generators of $SU(2)$ via a factor of $\frac{1}{2}$. We encourage the reader to now shift perspective on how to view a neutrino's behavior, in light of their ability to oscillate between flavor eigenstates. Oscillation between the two flavors can be viewed as analogous to a quantum spin's ability to oscillate between its up state $|\uparrow\rangle$ and its down state $|\downarrow\rangle$, each spin state corresponding to flavor states $|\nu_e\rangle$ and $|\nu_x\rangle$ respectively. By modeling the two-flavor neutrino as a spin-$\frac{1}{2}$ particle oscillating between the $|\uparrow\rangle$ and $|\downarrow\rangle$ states, this mapping naturally follows an SU(2) algebra.

Projecting the two flavor neutrino system onto an $SU(2)$ flavor eigenstate basis provides a convenient lens with which to view collections of neutrinos oscillating between more than two flavors, as will be discussed later on, and particularly for the MBνS case. The Pauli matrices (a factor of $\frac{1}{2}$ removed from the $SU(2)$ generators) now represent each neutrino's internal degrees of freedom as an individual spin, and each neutrino is now defined as a sum of the standard Pauli operators $\vec{\sigma_i} = (\sigma_i^x, \sigma_i^y, \sigma_i^z)$ where i corresponds to the i^{th} neutrino, the degree of freedom being the flavors each neutrino (or individual spin in the spin system) can be a mixture of. The complete vacuum oscillation term in the two-flavor model in the flavor basis now looks like:

$$\mathcal{H}_{\text{vac}} = \sum_{i=1}^{N} \frac{\Delta m^2}{4E_i} \vec{B} \cdot \vec{\sigma_i} \ , \tag{1.5}$$

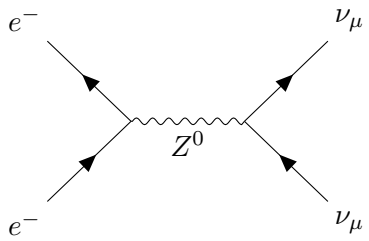

Figure 1.2: Z boson regulating neutrino-electron forward scattering for the neutrino-matter neutral current interaction.

1.2.2 Neutrino-Matter Interaction

The second term to account for in the neutrino Hamiltonian is the neutrino-matter interaction, caused by neutrinos coherently forward-scattering off of matter in the medium that they pass through when not in the vacuum [14, 15, 16]. This is the leading cause of the Mikheyev-Smirnov-Wolfenstein (MSW) effect, which describes how neutrinos' mixing angles are modified as they coherently forward scatter off of dense matter they transit through. Given that neutrinos experience only weak and gravitational forces, the potential matter interactions they can experience are relegated to electron-neutrino, proton-neutrino, and nucleus-neutrino forward-scattering.

Forward-scattering in this context refers to a neutrino interacting with external matter through the exchange of a W boson (for ν_e) or Z boson (all flavors) and continuing at the same initial momentum prior to the interaction, but with its eigenstate subject to nontrivial evolution. Neutrino-matter interactions involving Z bosons are called neutral-current interactions, conserve flavor, and thus do not contribute to flavor oscillations; see Fig.1.2 for a visual. Neutrino-matter interactions involving the W boson are called charged-current interactions, and are the only contribution to flavor oscillations because they predispose ν_e to relatively increased rate of flavor transformations; see Fig.1.1 for a visual.

In the flavor basis, it then makes sense to write the matter coupling constant as $\lambda = \sqrt{2}G_F n_e$ where G_F is Fermi's constant and $n_e = \frac{N_e}{V}$ the electron number density (where N_e is number of electron-type neutrinos and V is volume of a 3-dimensional area in space

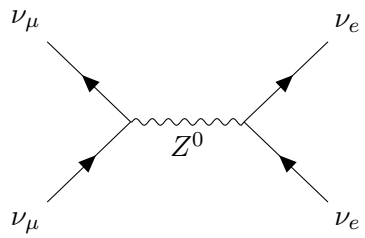

Figure 1.3: Z boson regulating neutrino-neutrino self interaction forward scattering in the S-channel.

in which n_e is calculated for (which we can take to be shaped like a box of length L), and thus neglect the number density of $\nu_x = \nu_{\mu+\tau}$.

The complete second interaction term $\mathcal{H}_{\text{mat}}$ in the two-flavor model of N neutrinos is then:

$$\mathcal{H}_{\text{mat}} = \frac{\lambda}{2} \sum_{i=1}^{N} \sigma_i^z \ , \tag{1.6}$$

1.2.3 Neutrino-Neutrino Interaction

The third interaction is the two-body neutrino-neutrino self-interaction term resulting from neutrinos forward scattering off of each other [17, 18, 19, 20], where each neutrino-neutrino forward scattering event consists of Z boson exchanges between one another, while initial momenta of each particle remains the same before and after the interaction; see Fig.1.3 for a diagram. The measurable quantity undergoing evolution in this interaction is the neutrino flavor phase $|\nu_{\alpha'}(t)\rangle = e^{-iE_\alpha t} |\nu_\alpha(0)\rangle$. All neutrinos within a neutrino gas are generally assumed to weakly entangled with one another yielding an all-to-all coupling structure (though collectively they can also be assumed to start out as a simple product state), with an interaction energy of $\mu = \sqrt{2} G_F (n_\nu = n_{\nu_e} + n_{\nu_{\tau,\mu}})$ where $n_{\nu_e}, n_{\nu_{\tau,\mu}}$ are the neutrino number densities for both flavors in our two-flavor model, and G_F is Fermi's constant.

Each i^{th} neutrino has an associated momentum of $\hat{p}_i = \frac{\vec{p}_i}{|\vec{p}_i|}$; the angle between two flavor momentum modes $\hat{p_i}, \hat{p_j}$, with flavor momenta $\vec{p_i} \neq \vec{p_j}$, is θ_{ij}. The forward-scattering i^{th}

and j^{th} neutrinos outgoing from the CCSN core is determined by θ_{ij}, which determines the geometry of the N neutrino system. For a more detailed explanation of this term and the systems geometery, see Section A.2. The effective two flavor neutrino-neutrino self-interaction Hamiltonian, in the forward scattering limit only, is then:

$$\mathcal{H}_{\nu\nu} = \frac{\mu}{2N}\sum_{i<j}^{N}(1-\cos(\theta_{ij}))\vec{\sigma_i}\cdot\vec{\sigma_j}\ , \tag{1.7}$$

Subtraction of $\cos(\theta_{ij})$ from 1 ensures no contributions from two neutrinos with parallel trajectories to the two body neutrino-neutrino interaction term, as no forward-scattering would occur. The full Hamiltonian[11, 10, 21] then reads as:

$$\begin{aligned}\mathcal{H} &= \mathcal{H}_{\text{vac}} + \mathcal{H}_{\text{mat}} + \mathcal{H}_{\nu\nu} \\ \mathcal{H} &= \sum_{i=1}^{N}\frac{\Delta_m^2}{4E_i}\vec{B}\cdot\vec{\sigma_i} + \frac{\lambda}{2}\sum_{i=1}^{N}\sigma_i^z + \frac{\mu}{2N}\sum_{i<j}^{N}(1-\cos(\theta_{ij}))\vec{\sigma_i}\cdot\vec{\sigma_j}\ ,\end{aligned} \tag{1.8}$$

1.2.4 Neutrino Systems within Core-Collapse Supernova

For the work covered in this document we are interested in systems located in the hot neutrino-dense region of a CCSN, see Fig. A.2 in Section A.2 for a schematic, where we can ignore the neutrino-matter term since at higher neutrino densities, similar to what would be found if located close to the CCSN core, the quantum correlations arising from neutrino-neutrino forward-scattering provides a significantly greater contribution in comparison to the neutrino-matter term.

Moving close to the neutrino sphere (on the order of 50km, see Fig. A.2) the weakly entangled neutrino gas becomes a hot, dense neutrino gas and enables a second simplification via taking the high-neutrino density limit $\mu \gg \frac{m_\Delta^2}{2E_k}$. This allows the one-body vacuum oscillation term to be neglected as vacuum interactions contribute comparatively little in this regime. The further simplified and final Hamiltonian we now work with is:

$$H = \frac{\mu}{2N}\sum_{i<j}^{N}(1-cos(\theta_{ij}))\vec{\sigma_i}\cdot\vec{\sigma_j} \tag{1.9}$$

The Hamiltonian described by Eq.(1.9) shares many structural similarities with the random long-range entangled Heisenberg spin chain, a model commonly used in condensed

matter physics, and quantum many-body studies. Both models possesses global SU(2) symmetry since the neutrino Hamiltonian's flavor isospin also obeys SU(2) symmetry (as justified in Section 1.2.1).

In CCSN settings close to the core, the neutrino-neutrino interaction results in exceptionally unique nonlinear dynamics that can occur only in settings where the density of neutrinos is high enough such that the flavor evolution of one particle is highly interdependent on the surrounding particles. Each neutrino's primary interaction now solely involves coupling to a bath of its sibling particles. This aggregate coupling between multiple unique neutrino modes motivated the development of collective flavor oscillations (CFOs) studies [22, 23, 24].

1.3 Collective Flavor Oscillations

While neutrinos are well known to be weakly interacting particles, in the right environment, such as extreme astrophysical settings, they can become heavily compacted against one another. In dense concentrations their weak interactions accumulate rapidly and give rise to large-scale nonlinear collective dynamics, which can significantly impact the outcomes of large-scale processes such as CCSN shockwave revivals, flavor transport in binary star post-merger fragments, and nucleosynthesis.

CFOs consists of multiple (usually many) neutrinos at various energies and momentas oscillating coherently in flavor space with one another. Each neutrino at a unique energy or momenta can be taken as its own individual mode. In the mid to early nineties the field of CFOs–also known as collective flavor conversions (CFCs)–began to form and grow, initiated first by efforts to explain large scale phenomena in neutrino dense settings. Such phenomena include: CCSN dynamics, energy and entropy transport in CCSNe, all stages of neutron star evolution, and the leptonic asymmetry present in the early universe.

Theoretical-only studies of collective flavor oscillation of high density systems–such as those found in CCSN environments, binary star mergers and big-bang nucleosynthesis–has seen great progress over the last four decades. [25, 26, 17, 27, 28, 18, 19, 29, 30, 31, 32, 33, 34, 35, 36, 37]. The work covered in this dissertation will focus on MBνS located close to the CCSN core.

These environments consist of large numbers of neutrinos rapidly fluctuating between their flavor eigenstates in coherent unison. Phenomena such as spectral swaps, splits, bipolar oscillations [37, 38, 39], These collective modes, known as CFO modes, are somewhat analogous to the collective modes that define quasiparticles often studied in condensed matter systems. This collective behavior of neutrino flavor eigenstate fluctuations motivates studying neutrinos from a many-body system perspective.

1.4 Many Body Neutrino Studies

The paradigmatic development of CFOs[12, 40, 41] underpins the many-body system perspective of neutrino studies, a relatively novel framework in itself with which to study neutrinos. Many-body system studies have largely been the practice of condensed matter investigations, which tend to focus on studying collective dynamics and interactions within strongly correlated systems–the interacting particles generally being electrons, cooper-pairs, majorana fermions and other quasiparticles.

In MBνS, as each neutrino interacts with not just its neighboring particles but all of the particles in the system, the system's entanglement grows, and quantum observables such as entropy, persistence and polarization play significant roles in the system's collective dynamics. Additionally, CFOs can be treated as quasiparticles themselves, as the behavior of flavor modes can be seen as analogous to other quasiparticles such as phonons. These physical features arise when taking the high-density neutrino limit in MBνS, and motivate rigorous many-body treatments, in order to better understand how various initial state conditions can lead to very different evolution outcomes.

1.5 Tensor Networks for Many-Body Neutrino Systems: Obvious Limitations and Indirect Advantages

This section outlines conceptual connections between tensor network (TN) [42, 43, 44] methods and renormalization group techniques developed in quantum field theory (QFT), with particular focus on their shared ability to describe quantum systems across varying scales. Tensor networks were originally developed for simulating low-dimensional strongly correlated systems in condensed matter physics. However, their underlying structure is

shared by the coarse-graining techniques of the renormalization group. Matrix Product States (MPS) [45, 46, 47, 48] and Projected Entangled Pair States (PEPS) [49, 50] in particular have demonstrated considerable success in simulating one-dimensional (1D) and two-dimensional (2D) quantum systems where traditional methods, such as exact diagonalization (ED), fail due to exponential scaling (2^L, with L being system length, or particle number) of the system's Hilbert space. TN methods however are able to circumvent this computational bottleneck by exploiting the area-law entanglement structure of ground states and the low-lying excitations of low-dimensional systems.

We begin by introducing the challenge of ultraviolet divergences in quantum field theories and the development of renormalization group methods as a means of controlling scale-dependent behavior. We then turn to the Density Matrix Renormalization Group (DMRG) [51] and its connection to MPS, followed by a comparison of Time-Evolving Block Decimation (TEBD) [52, 53] and the Time-Dependent Variational Principle (TDVP) [54, 55] as methods for simulating time evolution. We conclude with a brief survey of recent applications of tensor networks in theoretical high-energy physics.

Parallels between the Renormalization Group of Quantum Field Theory and the Density Matrix Renormalization Group

QFT is one of the greatest intellectual feats driven by collective scientific efforts. When it was first developed in the 20th century, for low-order computations QFT needed no more modification. However, at higher orders, a grave problem emerged in theoretical calculations: ultraviolet (UV) divergences, a situation where infinite sums accumulate via ultraviolet divergent Feynman diagrams when calculating short-distance contributions.

The solution to this problem was the conceptual development of renormalizability. Renormalizability is the general ability of a field theory's physical quantities, such as mass or charge, to undergo some rescaling such that the problematic ultraviolet-diverging infinite quantities from earlier are dissolved by the newly regulated physical quantities, leaving the previously problematically infinite field theory now finitely calculable. Such a field theory is called "renormalizable" [56, 57].

Renormalizability was tackled on different fronts asynchronously. In Quantum Electrodynamics (QED), via the insertion of counter terms, the extra diagram vertices were chosen hierarchically to cancel out infinities and was first posed as a solution to the infinite summation problem [57, 58]. This was then proven to be insufficient with the realization that not all QED field theory's UV divergences could be resolved by such a technique on its own, as gauge invariance was violated in certain instances. This lead to the development of the Ward–Takahashi identities [59, 60] in the 1950's. These identities were consistency conditions from gauge invariance which established current conservation and thus prevented spurious gauge symmetry-violating divergences (which manifest as poles in the complex momentum plane).

In the 1970's Quantum Chromodynamics (QCD)[61] was developed. Cutoff-based regularization methods like Pauli-Villars type regularization[62] were developed, but would be limited in their utility [63]. While lattice regularization is the only known regulator of non-Abelian theories, QCD benefited greatly from dimensional regularization[64], which regulated diverging infinities by evaluating them in d spacetime dimensions, where d is not necessarily an integer, to resolve the divergences while protecting gauge symmetry. In contrast to cutoff-based regularization schemes, dimensional regularization [64] preserves gauge invariance and Lorentz symmetry, making it well-suited to non-Abelian gauge theories like QCD.

The development of techniques such as dimensional regularization and the renormalization group validated that local physical observables in quantum field theories are scale-dependent quantities, meaning that the values of their measured physical observables depend on how a system's energy or size increases or decreases. This scale-dependent behavior was encapsulated by the Renormalization Group (RG), whose development was lead by Kenneth Wilson [65], and built upon the progress made in resolving divergences in perturbation theory [66, 67, 68, 69]. RG is a set of differential equations predicting the distance-dependence of physical quantities by integrating out high-energy modes, high-momentum degrees of freedom, and rescaling parameters–not just in QFTs on the continuum, but also for lattice models (as commonly studied by condensed matter physicists), such that physics for a given theory remains scale invariant.

Extending the measurement from such single-point correlation functions to non-local observables such as multi-point correlations, the expectation values of multi-point correlation functions power-law decay as spatial and temporal separation between each probe point of the multi-point correlation functions increases–this behavior is a consequence of RG-flow. It is the variance of expectation values of both local and non-local observables (i.e.: couplings, masses) as one moves from Ultraviolet (UV) to Infrared (IR) theory that is RG-flow.

The very same Wilson then introduced the numerical renormalization group (NRG) [65] to tackle the Kondo problem[70]. First, the Kondo effect is the phenomenon in which electrons scatter within a nonmagnetic metal due to a magnetic impurity–usually just one particle (ion or atom) is all that is needed to dope the metal with to produce such an effect. When previously conductive electrons scatter within a metal, conductivity decreases, and the metal's resistivity of course then increases.

An old phenomenon from the 1960s, the Kondo effect's current-day value [71, 72, 73] resides in the fact that the effect takes place in a strongly coupled system, and that it is a very difficult many-body problem to analytically describe whereas numerical it is much more feasible. The Kondo problem arises when attempting to apply perturbation theory to describe the electron's scattering through the metal. Though it correctly described the resulting electrical resistance at low temperatures, at very low temperatures the resistance diverged, and again the similar nonphysical infinities as seen in the QFTs concerning high energy physicist has emerged but this time in the context of strongly correlated systems at low temperatures.

Wilson's NRG however, correctly resolved the infinities by splitting up the conduction band energy spectrum, via a logarithmically-spaced mesh that allows discretization of energy shells of decreasing width, with discretization parameter $\Lambda > 1$ [65, 74, 75]. The low energies are then given precedence, mapped to a linear chain where from the first site to the last, the ordering of coupling strengths between the impurity and each conduction band state in the model is in decreasing order [75]. Now that the system has been ordered and mapped to a linear chain, the system is then repeatedly diagonalized, and states furthest from the impurity (high energy states, closest to the Fermi energy) are discarded, and after sufficient iterations of the procedure, a more accurate computation of the resistivity at low energies

can be obtained.

While the objective of the NRG was to tackle continuum models at low energies, the Density Matrix Renormalization Group (DMRG)[51, 76, 77], a separate technique, was developed to tackle lattice problems, a situation where NRG performed poorly on. As the name implies, the Density Matrix Renormalization Group (DMRG) instead operates on the density matrices of the system. DMRG is a numerical technique for studying (primarily 1D) quantum many body systems at low energy and was developed in 1992, and was the first demonstrated on Heisenberg spin chains.

The overarching theme emerging from tracing the progression of RG, to NRG [78] is the reigning paradigm of seeking resolution for nonphysical divergences via different analytical, then numerical techniques. Then in the context of NRG and DMRG, while the problem of discarding irrelevant higher-energy contributions and preserving only relevant low-energy contributions are the main objectives, the systems of study are continuum models for NRG and lattice models for DMRG, each requiring a different tactic to resolve computational errors.

While DMRG may not be the direct result of QFT's development of RG, it is certainly a product of the paradigms which motivated RG in the first place, that is understanding the behavior of physical observables and short distances and low energies, as we move from the continuum to, for DMRG's target systems, the lattice. Interestingly, when looking closely at the SVD operations utilized in DMRG's implementation [79, 80], we can take note of how each SVD yields a Schmidt spectrum, while also encoding the information needed to construct the reduced density matrices ρ of each bi-partition of the system.

It is worth taking a granular-level look at the numerical scheme [78] not simply for pedagogical reasons, but to build intuition. From each ρ the von Neumann entanglement entropy can be computed; in order for DMRG to work efficiently this quantity must grow no more than an area-law scaling. Each sweep operation works by discarding the portions of ρ which encode the low entanglement portions of the system. As DMRG sweeps from block to block, back and forth through the system, a partition k moves across the system partitioning each subsequent new two blocks (often called right block and left block in the algorithm) [81].

During the sweep, the entanglement that is discarded from the previous block (say the left block in a sweep from left to right), is then reincorporated into the neighboring right block; a consequence of the series of Schmidt decompositions occurring during each step of DMRG. During these steps, the Hilbert space of each new block is regrouped as k slides across the sites (L), ρ is recomputed, and thus each new von Neumann entropy that can be computed from each new redefined ρ (moving with k) reflects the redistributed entanglement entropy throughout each sweep step. This redistribution of von Neumann entropy during DMRG sweeps provides an early glimpse into the entanglement flow across the system, site by site, block by block, as a consequence of the numerical scheme [82, 83, 84, 85]

1.5.1 Time Evolution Methods for Matrix Product States

Matrix Product States (MPSs) are quantum states of N particles, represented as N tensors linked together via bonds to one another. This numerical framework allows for computationally efficient simulations[86, 53, 87] of many-body quantum states as the given system's particle number N scales up, only if: the system's size N remains reasonably small, the states of interest are not highly energetic, and the Hamiltonian of interest is gapped and 1D. For Hamiltonians that are gapless and higher than 1D, MPS can not suffice, whereas structures such as the multiscale entanglement renormalization ansatz (MERA) states support reproduction of properties in gapless states such as logarithmic scaling of maximum entropy. [88, 44], and projected entangled pair states (PEPS) can support 2D system geometries.

First, a quick introduction to the diagrammatic notation of TNs. Contained in Figure 1.4 are example TN diagram representations of a scalar, a vector, a matrix, a 3-dimensional matrix or an order-3 tensor, and an order-k tensor. Each leg in a tensor is called an *index*, and each index corresponds to a vector with a Hilbert space $\mathcal{H}$ having dimension d the same length as the vector. We note the last diagram in Fig. 1.4 is an order k tensor. To convert this k-dimensional object to a MPS representation, one applies the tensor train singular value decomposition (TT-SVD) algorithm to decompose a high-dimensional tensor into a MPS of k independent tensors, each tensor representing an individual site in the system.

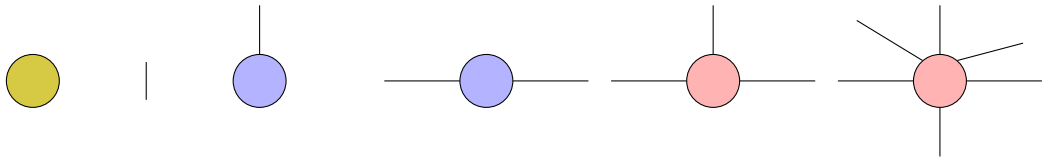

Figure 1.4: Using tensor network graphical notation, moving from left to right, the first diagram (yellow) is that for a scalar, the second (line) is that of the identity, the third (blue) for a vector, the fourth (blue) for a matrix, the fifth (red) for an order-3 tensor or 3-dimensional matrix, and the sixth (red) for an order-l tensor.

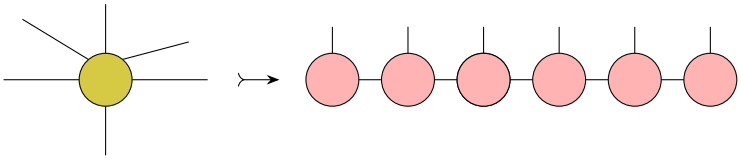

Figure 1.5: Conversion of a 6-dimensional tensor (left) to its corresponding Matrix Product State (MPS) representation (right) for later operation, after applying the tensor train singular value decomposition (TT-SVD) algorithm six times to decompose the higher-dimensional tensor on the left into the six-site MPS on the right.

See Fig. 1.5 for a visualization.

1.5.2 Time Evolving Block Decimation

The Time Evolving Block Decimation (TEBD) method [89, 77] is the process of breaking up and approximating the time evolution operator as a collection of multi-site gates. The Trotter formula (also known as the Lie-Trotter Product formula) [90] is used to split the time evolution operator, with an error of $\mathcal{O}(t^2)$: $S_1(t) = e^{\frac{(A+B)}{t}} = \lim_{n\to\infty}[e^{\frac{At}{n}}e^{\frac{Bt}{n}}]^n$. The Trotter-Suzuki decomposition [91] extends the original Trotter formula through recursive application of a second order symmetric split, with an error of $\mathcal{O}(t^3)$: $S_2(t) = e^{\frac{At}{2}}e^{Bt}e^{\frac{At}{2}}$.

Depending on the operator's construction TEBD breaks up the evolution operator via the Trotter-Suzuki decomposition, applies the components to an MPS, and reduces it's di-

mensionality through an tensor train Singular Value Decomposition (SVD). The MPS TEBD method has does have its limitations: as the system volume grows, so does the approximation error at each time step τ, making it difficult to rely on for long range interactions and systems of dimensionality larger than 2D, though there has been recent developments in making 1D and 2D systems easier to simulate via Krylov expansions of MPSs [92].

Yet, in some cases, such as in the all-to-all connected, two-flavor system neutrino system of concern in this document, MPS's failures can be leveraged to an advantage. Due to the all-to-all connectivity of this system, the the bond dimension increases rapidly as N grows, stressing the computational resources we had available to carry each state approximation. Because a system's bond dimension is intimately connected to the amount of entanglement present within it, insight into the rate at which entropy scales in the system can be indirectly acquired. Further exploration of entanglement growth via entropy measures and bond dimensions in $H_{\nu\nu}$ is underway, as follow-up work related to content contained in the next Chapter.

It can be beneficial to briefly walk through the basic elements of the MPS TEBD procedure with a simple model (more detailed references can be found elsewhere). Say that the Hamiltonian $\mathcal{H}$ of interest to us is just the Heisenberg chain:

$$H = \sum_{i}^{N} \vec{\sigma}_{i,i+1} \tag{1.10}$$

The exact time evolution operator for the time evolution of this system, with no truncations or approximations, is defined as:

$$\hat{U}(t) = e^{-iHt} \tag{1.11}$$

For first-order Trotter time evolution, we split up the exact time evolution operator into two terms, one consisting of even sites and the other consisting of odd sites in Eq. (1.10), as follows:

$$\hat{U}(t) \approx e^{-iH_{even}t} e^{-iH_{odd}t}, \tag{1.12}$$

where H_{even} and H_{odd} are:

$$\begin{aligned} \mathcal{H}_{even} &= \sum_{i \ even}^{N} \vec{\sigma}_{i,i+1} \\ \mathcal{H}_{odd} &= \sum_{i \ odd}^{N} \vec{\sigma}_{i,i+1} \end{aligned} \tag{1.13}$$

and with second-order Trotter time evolution looking like:

$$\hat{U}(t) \approx e^{-iH_{even}\frac{t}{2}} e^{-iH_{odd}t} e^{-iH_{even}\frac{t}{2}} \quad . \tag{1.14}$$

MPS TEBD then proceeds by applying a sequential series of two-site time evolution entanglement gates to each pair of sites in the system. For first order Trotter, one sweep of time evolution gates occur. For second-order Trotter, a sweep forward and then a sweep backward (two time evolution sweeps) occurs. After the application of unitary time evolution gates, a sweep of SVD occurs across each merged two-site pair, (after SVD'ing each merged two site pair, the pair is reshaped back to into two individual neighboring sites).

A SWAP network is necessary for an all-to-all system such as Eq. (1.7), because TEBD involves applying gates only to neighboring sites. Repeated applications of the two-site gates are required to account for the increased number of two-site interactions between sites physically separated from one another by one site or more. Implementation of MPS-TEBD for the Hamiltonians of type Eq. (1.7) decomposes to significantly more gates than Eq. (1.10) due to the SWAP network necessitation, in order to enforce the all-to-all connectivity of the system. See Figure 1.6 for a visualization of a many-body two flavor neutrino system consisting of five particles.

Fig. 1.6 contains a five neutrino example of Eq. 1.7. Let's break this down: the two-site interaction gates must be applied between qubits that are not neighbors in the 1D layout. A SWAP network thus must be constructed for sites: (1,2), (2,3), (3,4), (4,5), (1,3), (2,4), (3,5), (1,4), (2,5), and finally (1,5) for a total of 10 (or $\binom{N=5}{2}$ more succinctly) two-site SWAP gates.

However, after each SWAP gate brings relevant qubits adjacent, and the time evolution operator is applied to them, a final SWAP must be applied to restore the chain back to its original ordering. Implementing this requires alternating layers of SWAP gates to reorder

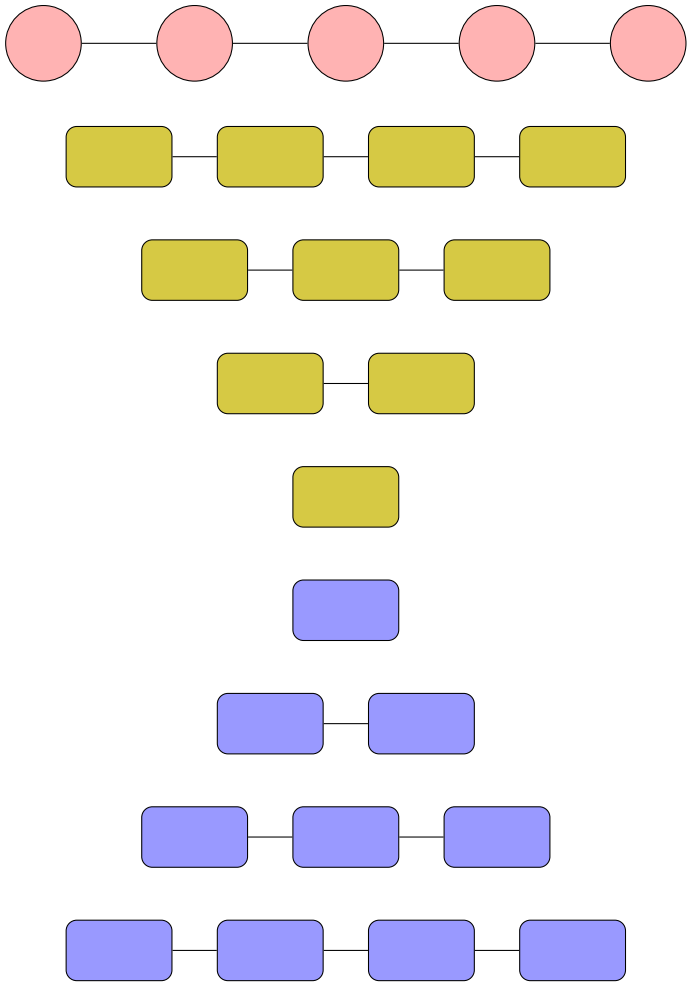

Figure 1.6: Since the SWAP network logically exchanges quantum states amongst the sites along the linear chain of qubits (red shaded circles at top), locality is preserved, as the physical qubits remain in their original locations. For the above five-site linear chain, a conceptual SWAP schematic is presented. A SWAP network, half of which consists of 10 two-site (two-qubit) gates (yellow), is required to enforce *all-to-all* interactions for the five neutrino system, with each neutrino represented as a single qubit. A total of 20 SWAP operations (rectangular blocks) occur across the circuit, in order to reverse the initial SWAP actions and restore the system to its original order (blue).
For brevity the actual positioning of the SWAP gates on each qubit channel in the necessary time-ordered sequencing is not explicitly rendered in this document, but can be easily drawn out with the method's description provided in this document.

qubits, a two-site gate layer to apply the interaction, and a final layer of SWAP gates to undo the initial rearrangement. All of this occurs in a serialized manner, which is why a five neutrino system needs a total of $\binom{N=5}{2} \times 2 = 20$ SWAP gates.

Circuit depth and the entanglement support requirement of the MPS increases with each layer to maintain accuracy. The bond dimension D required to capture the entanglement of such a system thus grows rapidly, an obvious disadvantage of this numerical approximation scheme for all-to-all systems which follow volume-law entanglement scaling.

1.5.3 Comparison of TEBD to the Time Dependent Variational Principle

This section contains a very brief summary of the Time Dependent Variational Principle (TDVP)[93, 55], though the reader is advised to reference more detailed sources online and elsewhere for in-depth explanations on the TDVP method (as well as other time evolution methods, such as Matrix Product Operator (MPO)-based methods[94]).

MPS-TDVP is structurally very different from MPS-TEBD in that MPS-TDVP relies on projecting the time evolution Schrodinger equation of the Hamiltonian onto some MPS with fixed bond dimensions' tangent space. In this perspective, the MPS manifold for a certain bond dimension is a subset within the Hilbert space. TDVP essentially iterates around on some plane which is tangent to this MPS of fixed bond dimension, iterating from the point where the tangent plane touches the MPS. This is where the variational scheme begins from as its starting point, in TDVP.

The primary takeaway when comparing TDVP and TEBD against one another is that TDVP is a variational time evolution scheme while TEBD is a projective one. This structural difference guides much of the computational tradeoffs between TDVP and TEBD. Below are a few interesting and important aspects to consider when choosing which method to use.

1.5.4 Small Bond Dimensions

Both TEBD and TVDP fail when D between system sites approach values lower than the required value for accurate representation of entanglement between sites, but for very

different reasons. As stated earlier, TDVP is a variational approximation scheme, and approximates a manifold of MPS states with a particular D–time evolution is constrained within this low-D manifold. While time evolution is still unitary while operating within this manifold, the manifold itself may drift away from the original many-body wavefunction and instead become tangent to another wavefunction, and the variational scheme would then unintentionally iterate the manifold away from the desired target state.

TDVP can be thought of as artificially moving through potential Hilbert spaces of the system, and because of this variational nature TDVP can loose its way. Thus, TDVP runs the risk of silently suppressing entanglement, as it does not allow for dynamically growing entanglement to be accurately captured. The method presents no obvious signature in its performance that a system's approximated evolutionary dynamics have transgressed into nonphysical dynamics.

Situations where entanglement is misleadingly depicted as stagnant can easily arise in the small D limit. One can easily imagine a TDVP simulation hallucinating exotic phenomena, such as many-body localization, that is not physically accurate for the system's time evolution. This can be exacerbated when entanglement is expected to grow rapidly from small D values.

TEBD's issues with small bond dimensions are more straightforward, as the time evolution is projective, using SVD to truncate each two-site gate application. Under a too small D TEBD will bluntly truncate prematurely if the entanglement grows too fast for the implementation to accommodate. The information (stored as low-weight Schmidt coefficients) is simply lost if the required D to represent entanglement exceeds the cutoff D and is not updated in time.

This can be more clearly seen with a more explicit demonstration. Assume that every two MPS tensors correspond to neighboring sites (or sites which are SWAP gated to become next to one another):

$$\begin{aligned} &A^{[i]}_{\alpha,m,\beta} \quad for\ site\ i \\ &A^{[i+1]}_{\beta,m,\lambda} \quad for\ site\ i+1. \end{aligned} \tag{1.15}$$

Then we contract the two sites and then apply the two site gate:

$$M_{(\alpha,m),(n,\lambda)} = \sum_{m',n'} U_{mn,m'n'} \quad \cdot \quad \sum_{\beta} A^{[i]}_{\alpha,m,\beta} \cdot A^{[i+1]}_{\beta,m,\lambda} \tag{1.16}$$

after which we group the indices, perform SVD and truncate S:

$$M_{m,n} = U \cdot S \cdot V^{\dagger}. \tag{1.17}$$

As the singular values of M are stored in S, truncating S effectively modulates D between the two sites, as the SVD operation split the entanglement between sites i and $i+1$. Thus, a D set too low by TEBD (the truncation operation acts on S) will discard potentially nontrivial information.

As with TDVP, a similar issue of nonphysical dynamics arises with TEBD. False thermalization can emerge unless TEBD has adaptive bond dimension implemented–the hard ceiling on D causes this. However, because D's cap is known in TEBD, it is conceptually easier to track and rectify implementation-wise. TEBD is also relatively more straightforward to prevent such premature suffocation of D, one can ensure the truncation error is small enough (generally anything around 10^{-9} is considered safe). Additionally this truncation error is accessible and trackable since it is the discarded Schmidt weight (unlike in TDVP). To maintain fidelity, adaptive D schemes can prevent artificially suppressed entanglement artifacts, as well as other simple tricks including comparing observable results at varying D values.

1.5.5 Large Bond Dimensions

TEBD does poorly with fixed bond dimensions implemented for large growing D between sites in the system, for obvious reasons: we have an upper limit on what will be encoded between each site's D with one another, so of course, things will be truncated and lost. This prematurely truncating phenomena is a similar situation as what occurs with small D, though for a more straightforward reason. In general TEBD's solution to growing D is simple: simply increase the threshold if one does not want an adaptive D protocol coded into the implementation.

However, TEBD with adaptive bond dimensions mitigates the issue, but incurs a computational cost. TDVP however comes in two variants, where the fixed bond dimension implementation presents an obvious flaw for growing large D, whereas TDVP with adaptive D enabled is more successful at capturing states' growing entanglement.

1.5.6 Time Evolution

TDVP is significantly better for long time intervals compared to TEBD due to the stability its implementation offers, however TDVP is more expensive computationally. The growing Trotter errors and truncation errors of TEBD restrict its use for long time evolution. TDVP requires storing information about the tangent space, and storing information after each time step in temporary variables consume additional memory requirements as the method runs throughout the time evolution, but the trade-off is accuracy in evaluation, which TEBD does not offer due to truncation and Trotter errors that accumulate at long times.

1.5.7 Long-Range Entanglement

TDVP by construction, does not have the same position constraint in its implementation scheme as does TEBD. Two site entangling operators can reach only so many sites in the linear chain with TEBD, so a SWAP network introduction is necessary, and then followed by an unwieldily number of entangling gates that need to be applied to cover all the necessary interactions for implementing an all-to-all connected network.

TDVP operates in the tangent space of the MPS, time evolving the entire system itself regardless of the entanglement structure. There is no need to even be aware of where entangling gates need to be accounted for. As such, the time evolution at long times does incur the cumulative Trotter error one needs to mind with TEBD. But one pays a cost in some way, always: if the MPO one utilizes with TDVP is memory consuming (we operate in the tangent space so more information at each time step must be stored, even if temporary), can not be compressed in an efficient manner, then computational roadblocks in the form of speed emerge. Memory costs provide an immediate stop. And worse, TDVP is a sequential process so parallelization must be handled with care as the sequential sweeps across the

linear chain of sites can not be easily broken up without destroying the order that sweeps must be conducted in.

1.5.8 Large N

With respect to 1+1D systems, both TEBD's and TDVP 's computational runtime scales linearly with system size. TEBD is amenable to parallelization due to its block structure which accommodates simultaneous non-overlapping two-site gates. This is convenient for implementation on multi-core platforms. TDVP requires a sequential sweep across the MPS chain, making parallelization difficult.

Unlike TEBD, TDVP does not suffer from Trotter error, which becomes significant at large N. TEBD also tends to benefit from a dynamically updated bond dimension D, as entanglement gets truncated when updating each two-site gate. Meanwhile, two-site TDVP allows D to grow.

Exact Diagonalization (ED), by contrast, is fundamentally constrained at large N. For systems with very little exploitable symmetry (as is the case in all-to-all connected many-body neutrino systems studied in this dissertation), block-symmetries are nonexistent and cannot be taken advantage of and the full Hilbert space must be stored and operated on. On personal machines or single nodes of a local university HPC cluster, ED typically becomes infeasible around $N = 18$ for spin-$\frac{1}{2}$ chains. Larger ED studies have been performed in the literature—e.g., up to $N = 44$ [95]—but such efforts are not the norm, especially when evolving long-range entangled states lacking symmetries to block diagonalize.

As this dissertation primarily focuses on dynamics, there is moderate motivation to question reliance on ED when TNs can potentially yield *good enough* qualitative results. If ED can be utilized instead as a ground truth reference rather than the simulation's sole engine, then TDVP can approximate observables moderate D. At smaller system sizes, ED can again serve as a baseline to calibrate the error introduced by D truncation in TEBD. Such an approach can enable reliable pursuit larger systems inaccessible to ED alone.

This hinges on whether the Hamiltonian (such as the one in Eq.1.7) can be compressed efficiently as a Matrix Product Operator (MPO) with a manageable bond dimension. If so,

then TEBD and TDVP remain tractable even at large N.

1.5.9 Tensor Networks in High Energy Particle Physics Studies

Given the above laundry lists of issues and advantages of MPS-TEBD, MPS-TDVP and ED, it is worth briefly reviewing how recent high energy theory investigations have been able to utilize TNs [96, 97, 98] for their advantage. With respect to system dimensionalities, for 3+1D systems, there is no known standard TN structure capable of efficiently handling the entanglement growth following a 3D area law. The TN explorations for 3+1D have not yielded a generalized TN structure capable of efficiently handling 3+1D systems, and the current structures studied are very model-dependent, and reliant on many symmetries being present in the system of concern [99, 100, 101]. For 2+1D, Projected Entangled Pair States (PEPS) [102, 103, 104] and the Multiscale Renormalization Ansatz (MERA) [105] are most suitable, while for 1+1D systems, MPS is almost always the most optimal unless the system contains volume-law entanglement.

Several studies have investigated lattice models close to QFT and Lattice Gauge Theories using TNs to study dynamical phenomena [106, 107], scattering in Lattice QED [108], meson melting [96], scattering in the Lattice Schwinger model [109] and with matter [110], Z_2 [111] and Z_3 Lattice Gauge Theory [112], along with many others [113, 114]. Hadronic structure studies leveraging TNs have also seen progress, particularly work on Schwinger model parton distribution functions [115, 116], and parton distribution functions [117].

TNs offer promise as a workaround for the sign-problem often encountered in Monte-Carlo (MC) simulations of Lattice QCD theories and Lattice Gauge Theories, as well as potential to expedite computations of long-time dynamics [118], and thus deserve further study as mainstream computational schemes in theoretical high energy physics. The last decade has witnessed a notable growth in efforts to expand TNs utility to High Energy physics, as TNs offer relief from the sign problem and the entanglement growth bottleneck MC imposes [119, 107, 98, 111, 112, 108, 106, 118, 120].

1.6 Quantum Information Dynamics and Simulations of Many Body Neutrino Systems

Alongside pursuing quantum information science (QIS) applications to further simulations of larger neutrino system sizes, a comprehensive understanding of the quantum interactions underpinning coherent leptonic evolution stands to benefit a great deal from QIS in return. QIS has developed highly specialized tools for analyzing quantum entanglement and dynamics. Applications of QIS techniques to self-interacting neutrino gasses have recently yielded novel insights into the underlying physics of highly entangled neutrino systems, and of spin systems in general. A growing body of work [121, 122, 123] leveraging QIS tools in neutrino oscillation studies has advanced understanding of quantum processes in neutrino systems, results beyond the reach of previous mean-field calculations, but not beyond that of classical simulations. Investigations into entanglement entropy, far-from-equilibrium dynamics [124, 125, 126, 121, 122, 127], and calculations of concurrence, logarithmic negativity, and n-tangles [128, 129, 37] have resulted in valuable insights on entanglement behavior in systems of neutrinos. Recent work on dynamical quantum phase transitions (DQPTs) in two flavored neutrino systems with simple geometries [126, 122, 130] has demonstrated what conditions are necessary to observe a DQPT, and its connection with collective flavor oscillations. A short summary of QIS tools applied to neutrino oscillation investigations is contained in Ref [131].

The dependence of various astrophysical processes – from supernovas to early universe nucleosynthesis – on the initial flavor composition of dense neutrino gas systems is still undetermined. This can play a significant role in thermodynamical sub-processes by influencing leptonic dynamics such as flavor conversion and transport. Understanding how phase transitions occur in out-of-equilibrium neutrino systems can reveal deeper mechanisms at work within such astrophysical phenomena. The second chapter of this dissertation contains a focused study of Loschmidt echo crossing distributions, their connection to dynamical quantum phase transitions (DQPTs) and collective flavor oscillations. Loschmidt Echos are essentially measurements of the wave-function overlaps of a system's state at time t and a chosen initial state from which the system was quenched. This work explores how large

self-coupling angle ranges of geometrically heterogeneous momenta–in flavor space–in the neutrino-neutrino self-interaction term gives rise to two distinct time scales of DQPTs in two-flavor neutrino systems, with further analysis suggesting a DQPT dependence on the initial-state flavor configuration of the system. Additionally, the role of far-from-equilibrium processes in such neutrino-dense mediums is not yet well understood, and the third chapter of this dissertation presents preliminary findings when studying quantum information scrambling in the context of many-body two flavor neutrino systems.

Neutrinos are naturally described as a three-level system given the three flavor states ν_e, ν_τ, ν_μ that they can oscillate between. However, since d-level quantum platforms are currently an emerging technology, it can be quite difficult to obtain quantum computational time on such platforms. In the interim, it is prudent to begin laying the theoretical groundwork for simulating three-level neutrino systems, which naturally embed onto a qutrit, on quantum platforms, beginning with two-level(qubit) platforms. Simulations of d-level systems on qubit platforms can provide benchmarks that can guide the development of d-level devices. The fourth chapter of this dissertation explores novel qubit-based circuits for three-level neutrino systems, the simulation of such circuits on qubit-based platforms including the heavy-hex connectivity superconducting qubit platforms of IBM and trapped ion-based all-to-all connected devices of Quantinuum, and the computation of physical observables including neutrino flavor persistence and entanglement entropy.

While other models have been studied in great depth, this dissertation primarily focuses on monochromatic two flavored systems with larger, more complex, anisotropic distributions of momenta, while the last chapter covers monochromatic three flavored systems. Focusing on the multi-angle case allows for nontrivial entanglement development, and motivates the many-body treatment. Restricting particles to uniform energy primarily serves to reduce computational complexity of the problem. The multi-beam model allows for a simplified scenario in which to study complex quantum phenomena, and serve as a base case against which asses system configurations and parameters of interest when extending the model towards more realistic descriptions of neutrino systems, i.e.: inclusion of non-forward scattering interactions, additional neutrino-interaction Hamiltonian terms such as Eq. 1.5 and Eq. 1.6, inclusion of heterogeneous neutrino energies. The work presented will focus on

quantum dynamics emerging in the two flavored case, as well as the articulation of the three flavored case onto quantum devices.

Chapter 2

TIMESCALES OF DYNAMICAL QUANTUM PHASE TRANSITIONS IN NEUTRINO SYSTEMS

The work presented in this chapter is based on work done in collaboration with Alessandro Rogerro and Martin Savage [132].

2.1 Introduction

Neutrinos play a fundamental role in extreme astrophysical environments, such as CCSN and neutron star binary mergers, where they, in part, determine the dynamical evolution of the explosion and set the ambient conditions for the ensuing nucleosynthesis, e.g., Refs. [133, 134, 30, 31, 32, 135, 136]. Important neutrino-matter processes active in these scenarios proceed through weak charged-current reactions, and can therefore be strongly affected by inhomogeneities in the flavor composition of the neutrino flux. It is well known that neutrinos can experience flavor oscillations in vacuum (for a recent review, see Ref. [137]) but, for neutrinos with MeV energies, these occur over length scales that are typically large compared to the size of the supernova core. In these environments, flavor oscillations are modified by charged-current scattering with charged leptons, leading to the MSW effect [15, 16], and neutral-current neutrino-neutrino scattering which can lead to collective flavor oscillations [138, 17, 18, 19, 34, 139, 35, 140, 141] (see also Refs. [12, 142, 143] for reviews) which can dramatically reduce the oscillation length scales and thus possibly have important impact during the explosion [144, 145]. The physics of collective flavor oscillations is typically discussed in terms of mean-field Boltzmann kinetic equations [27, 146, 147] which assume that neutrinos de-correlate between successive collisions among themselves. A better understanding of correlation effects beyond mean-field descriptions has been a topic of interest since the beginning of this research area [123, 148, 149, 150], and has recently seen a resurgence of efforts [151, 124, 125, 121, 126, 152, 122, 153, 37, 154, 38, 155, 156] (see Ref. [130] for a recent review, and also Refs. [157, 158] for recent discussions concerning

the many-body approaches) aided in part by the use of available NISQ-era [159] quantum computers and by quantum information tools more generally [127, 128, 160, 129, 161] (see also Refs. [162, 131, 163] for recent reviews). A direct connection between the presence of unstable collective modes, whose amplitude grows exponentially at early times, with the presence of Dynamical Phase Transitions (DPT) [126, 122] has recently been shown. This led to a proposal [122] of a unified description of unstable modes generated by asymmetries in the vacuum term, the so called "slow-modes" in the neutrino literature, with unstable modes generated by asymmetries in the flavor dependent angular distribution of neutrino velocities, the so called "fast-modes" This identification was later shown to hold rigorously at the mean-field level [164]. In this work, we extend the previous analysis of Ref. [122], that considered simple angular geometries, to the full multi-angle regime.

Neglecting the non-forward scattering processes between neutrinos and the external matter and neutrinos among each other, the Hamiltonian describing flavor evolution of neutrinos in dense environments contains three main contributions (see Ref. [12] for a review): a one-body term responsible for neutrino flavor mixing in vacuum, a one-body term describing forward scattering between neutrinos and a static matter background (which gives rise to the MSW effect) and, finally, a two-body interaction term describing weak neutral-current forward scattering among neutrinos. In the two-flavor approximation, neutrinos can be described in terms of a $SU(2)$ flavor isospin, with the convention $|\nu_e\rangle = |\uparrow\rangle$ for the electron flavor and $|\nu_x\rangle = |\downarrow\rangle$ for the heavy flavor. In terms of flavor isospin, the Hamiltonian for N neutrinos can then be written in the flavor basis as [10, 11],

$$\mathcal{H} = \sum_{i=1}^{N} \frac{\Delta_m^2}{4E_i} \vec{B} \cdot \vec{\sigma_i} + \frac{\lambda}{2} \sum_{i=1}^{N} \sigma_i^z + \frac{\mu}{2N} \sum_{i<j}^{N} (1 - \cos(\theta_{ij})) \vec{\sigma_i} \cdot \vec{\sigma_j} \ , \tag{2.1}$$

where $\vec{\sigma_i} = (\sigma_i^x, \sigma_i^y, \sigma_i^z)$ is a vector of Pauli operators acting on the i^{th} neutrino and E_i is the energy of the i^{th} neutrino. Neutrino masses are included by the squared-mass difference $\Delta_m^2 = m_2^2 - m_1^2$ and the mixing angle θ_{mix} in the normalized vector $\vec{B} = (\sin(2\theta_{mix}), 0, -\cos(2\theta_{mix}))$, reflecting the mass basis. Assuming a negligible density of heavy charged leptons, the coupling constant of the matter term is $\lambda = \sqrt{2} G_F n_e$ with G_F Fermi's constant and n_e the electron-number density. The interaction term has a coupling constant $\mu = \sqrt{2} G_F n_\nu$, with n_ν the total neutrino-number density, while θ_{ij} is the relative

angle between the momenta of the i^{th} and j^{th} neutrinos, and encodes the geometry of the problem.

In this work, we are interested in the region close to the neutrino-sphere where the neutrino-neutrino coupling μ is much greater than the typical vacuum-oscillation frequency so that the first term in Eq. (2.1) can be neglected. In this regime, since the matter term commutes with the interaction term, for initial flavor states we can also neglect the presence of matter since it will not contribute to the ensuing flavor oscillation. Finally, we consider a geometry with axial symmetry with respect to some direction $\hat{z}$, which we take to be normal to a spherically symmetric neutrino-sphere, and average over the azimuthal angle ϕ. The Hamiltonian then becomes,

$$\mathcal{H}_{\nu\nu} = \frac{\mu}{2N}\sum_{i<j}^{N}(1-\cos(\theta_i)\cos(\theta_j))\vec{\sigma_i}\cdot\vec{\sigma_j} \;=\; \frac{\mu}{2N}\sum_{i<j}^{N}\mathcal{J}_{ij}\vec{\sigma_i}\cdot\vec{\sigma_j}\;, \tag{2.2}$$

with θ_i the polar angle of the i^{th} neutrino momentum, and where we introduce, for later convenience, the neutrino-neutrino coupling matrix $\mathcal{J}_{ij}$. In our numerical simulations, we use a forward-peaked uniform angular distribution with $\theta_i \in [-0.5, 0.5]$. We have verified that the conclusions reached with this choice of distribution remain unchanged qualitatively when adopting a different angular range or other smooth non-uniform distributions (such as triangular or Gaussian). As pointed out in previous works [38, 156], the use of uniform grids of angles can lead to undesirable artificial degeneracies in the Hamiltonian's energy level. To prevent such (lattice) artifacts, the angles θ_i are randomly distributed uniformly on the interval $[0, 0.5]$, and ensemble calculations with different realizations are performed. As shown in Ref. [164], the Hamiltonian in Eq. (2.2) is integrable, in the sense that it allows for an extensive number of conserved charges, and is therefore not able to thermalize the reduced one-body density matrices to a Boltzmann distribution [156]. Nevertheless, it is a model commonly employed in studies of fast-flavor conversion [165, 164, **?**], and provides a useful and interesting test case to analyze the time-scales associated to flavor oscillations in the many-body setting.

For the calculations described in this work, an initial tensor-product state of N neutrinos given by

$$|\Psi_0\rangle = \otimes_{i=1}^{N/2}|\nu_x\rangle_i \otimes_{j=N/2+1}^{N}|\nu_e\rangle_j = |\nu_x\ldots\nu_x\nu_e\ldots\nu_e\rangle\;, \tag{2.3}$$

composed by $N/2$ electron neutrinos and $N/2$ heavy flavor neutrinos, is employed. This is a common initial state used in many previous works on many-body flavor evolution [126, 121, 154, 37], and has the advantage of enabling a focus on effects beyond mean-field as the state $|\Psi_0\rangle$ is invariant under mean-field evolution, and at the same time simplifies the analysis of DPT(s) in the model (see e.g., Ref. [126]). This is because a DPT is signalled by non-analiticities in the Loschmidt echo [166, 167, 168], the probability of observing a time evolved state $|\Psi(t)\rangle = e^{-iHt}\,|\Psi_0\rangle$ in its initial condition $|\Psi_0\rangle$, presents itself as a crossing of two separate Loschmidt echoes associated with $|\Psi_0\rangle$ and its time-reversal counterpart [169]. This makes the numerical analysis easier to carry out than in the case where the Loscmidt echo shows a zero instead (as in Ref. [122]).

In this work, Sec. 2.2 presents a linear stability analysis of the collective modes supported by the axially symmetric Hamiltonian in Eq. (2.2) with the initial flavor state $|\Psi_0\rangle$ from Eq. (2.3). In Sec. **??**, a more detailed characterization of Dynamical Phase Transitions in terms of the Loschmidt echo is presented, specializing the discussion to the model considered in this work. In Sec. 2.4, the results obtained for the Loschmidt echoes crossing time for an ensemble of neutrinos systems with sizes ranging from $N = 4$ to $N = 14$ are presented, along with a statistical analysis of the observed time scales. We summarize our findings in Sec. 3.3, and comment on potential directions of future research.

2.2 Linear Stability Analysis

In order to shed light on the expected collective modes present in the system, we use the standard tool of linear stability analysis [170, 171, 172] (see also Ref. [122]). This starts with the evolution equations for the expectation values $\langle\vec{\sigma}_i\rangle$ within the mean-field approximation. For our model Hamiltonian Eq. (2.2), these are

$$\frac{d}{dt}\langle\vec{\sigma}_i(t)\rangle = \frac{\mu}{N}\sum_{j\neq i}\left(1-\cos(\theta_i)\cos(\theta_j)\right)\langle\vec{\sigma}_j(t)\rangle \wedge \langle\vec{\sigma}_i(t)\rangle\ . \tag{2.4}$$

For initial states aligned along the z direction and up to linear order in deviations from the initial condition, the third components $\langle\sigma_i^z\rangle$ remain static, while the transverse components

evolve via

$$i\frac{d}{dt}\langle\sigma_i^{\pm}(t)\rangle = \frac{\mu}{N}\sum_{j\neq i}(1-\cos(\theta_i)\cos(\theta_j))\left[\langle\sigma_j^z\rangle\langle\sigma_i^{\pm}(t)\rangle - \langle\sigma_i^z\rangle\langle\sigma_j^{\pm}(t)\rangle\right] = \sum_{j=1}^{N}\mathcal{M}_{ij}\langle\sigma_j^{\pm}(t)\rangle \ , \tag{2.5}$$

where $\sigma_i^{\pm} = (\sigma_i^x \pm i\sigma_i^y)/2$, decoupling the remaining two equations. The matrix $\mathcal{M}$ appearing in the right hand side is

$$\mathcal{M}_{ij} = \delta_{ij}\left[\frac{\mu}{N}\sum_{k\neq i}(1-\cos(\theta_i)\cos(\theta_k))\,\langle\sigma_k^z\rangle\right] - (1-\delta_{ij})\frac{\mu}{N}(1-\cos(\theta_i)\cos(\theta_j))\,\langle\sigma_i^z\rangle \ , \tag{2.6}$$

which is manifestly not symmetric. Since the equations are linear, the solutions can be expressed as linear combinations of the N fundamental solutions,

$$s_i^{(n)}(t) = \psi_i^{(n)}e^{-i\omega_n t} \ , \tag{2.7}$$

where $\psi(n)_i$ is the component of the n-th eigenvector of $\mathcal{M}$ of the i-th neutrino and ω_n the corresponding eigenvalue. The eigenvalues can be either real or complex conjugate pairs, the latter case indicating the presence of unstable collective modes whose amplitude can grow exponentially in time. We will use the notation $\omega = \Omega + i\Gamma$, with real Ω and Γ, to denote the real and imaginary part of the eigenvalues.

In order to perform the linear stability analysis associated with the collective oscillation spectrum in this model, calculations of the eigenvalues for systems of even size from $N = 4$ to $N = 16$ were performed, using angles θ_i sampled uniformly in $[0, 0.5]$. For each system size, we performed 10^6 calculations corresponding to different random samples of the angles, starting in the initial state from Eq. (2.3). The results of these calculations are displayed in Fig. 2.1. There are several points to note from these results. First, as shown in the inset on the left panel of Fig. 2.1, the fraction of stable eigenvalues (with imaginary component $\Gamma = 0$) decreases exponential with the system size. This means that for large systems of neutrinos, the model described by Eq. (2.2) and with initial state $|\Psi_0\rangle$ from Eq. (2.3) will contain unstable collective modes with high probability. This is in contrast to more geometrically symmetric systems such as the case of bipolar oscillations [121, 37, 154] or of fast oscillations in systems with three neutrino beams [122]. A somewhat unexpected result is the presence of two distinct types of unstable modes, as shown by the left main plot in the

left panel of Fig. 2.1, which shows the observed frequency of occurrence (i.e., a histogram normalized so that the sum over the bin values times the bin width is unity) of unstable modes of different magnitudes of the imaginary part Γ for $N = 14$. The same behavior is observed for all values of N examined. These two classes of modes are characterized by typical growth rates of either $\Gamma \approx 10^{-4} - 10^{-5}\mu$ or $\Gamma \approx 10^{-9} - 10^{-10}\mu$. In order to shed light on the structure of these two classes of modes, we present in the right panel of Fig. 2.1 a heat map, for the same ensemble of systems used in the main plot of the left panel, showing the observed correlation between the magnitude of the real part Ω and imaginary part Γ of the unstable modes. Unstable modes with large growth rates Γ are associated with large real frequencies Ω and, conversely, modes with a small growth rate also have typically very small real frequencies. The observed values of the eigenvalues with small imaginary part are found to be strongly affected by floating-point errors, and should be regarded as eigenvalues with $\omega = 0$.

The importance of considering both the real and imaginary part of unstable modes in the context of collective neutrino oscillations was recently pointed out in Ref. [165], where it was shown that, for a class of angular and flavor distributions, the oscillation depth quantifying the magnitude of flavor conversion was directly linked to the ratio $|\Gamma/\Omega|$: small values lead to a small oscillation depth, while, conversely, large value can lead to complete flavor inversion. In the present work, we use similar techniques (see also Ref. [164]) to provide a more concrete characterization of the observed two classes of modes in this model. We start by rewriting the linearized equations of motion Eq. (2.5) as,

$$\begin{aligned} i\frac{d}{dt}\langle\sigma_i^{\pm}(t)\rangle &= \frac{\mu}{N}\sum_{j=1}^{N}(1-\cos(\theta_i)\cos(\theta_j))\left[\langle\sigma_j^z\rangle\langle\sigma_i^{\pm}(t)\rangle - \langle\sigma_i^z\rangle\langle\sigma_j^{\pm}(t)\rangle\right] \\ &= \mu\left[S_0^z\langle\sigma_i^{\pm}(t)\rangle - \langle\sigma_i^z\rangle S_0^{\pm}(t) - \cos(\theta_i)S_1^z\langle\sigma_j^{\pm}(t)\rangle + \cos(\theta_i)\langle\sigma_i^z\rangle S_1^{\pm}(t)\right] \quad , \end{aligned} \tag{2.8}$$

where the moments (equivalent to the vectors $\mathbf{D}_n$ in Refs. [165, 164])

$$\vec{S}_n(t) = \frac{1}{N}\sum_{j=1}^{N}\cos(\theta_j)^n\langle\vec{\sigma}_j(t)\rangle \ , \tag{2.9}$$

have been introduced. We note that $\vec{S}_0$ is a conserved quantity owing to the global $SU(2)$ symmetry of the Hamiltonian $\mathcal{H}_{\nu\nu}$ in Eq. (2.2) (a property maintained at the mean-field

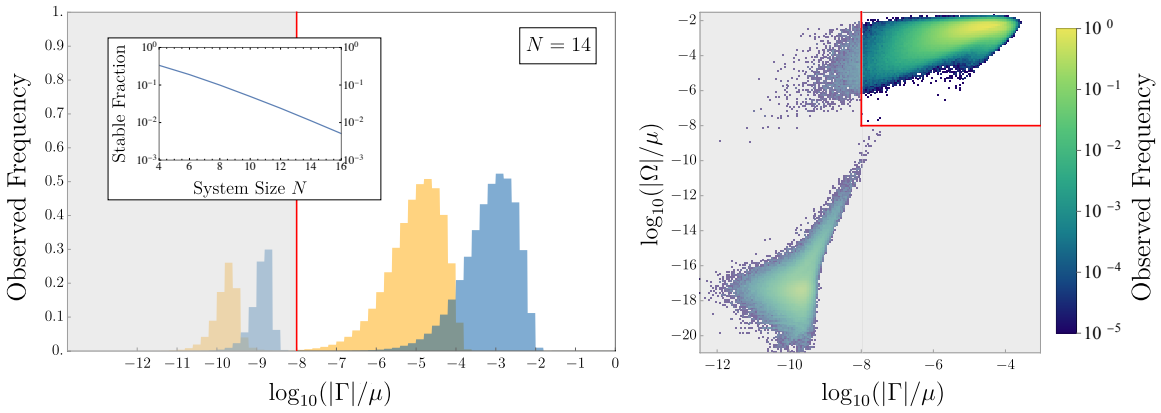

Figure 2.1: The left panel shows a histogram of the observed frequency of eigenvalues with a given imaginary component Γ (in units of μ) for a system with $N = 14$, and using 10^6 independent realizations of the angles θ_j. The inset in the left panel shows the fraction of stable eigenvalues, with imaginary component $\Gamma = 0$, as a function of system size. The right panel shows the observed frequency of unstable eigenvalues with a given magnitude of the real part Ω and imaginary part Γ for the same system. In both panels the presence of modes with small values of $|\Gamma|$ and $|\Omega|$ is a numerical artefact, with the correct mode at zero frequency. We indicate the boundary of the region where numerical errors become important with red lines in both plots and on the right panel we show it also as a grey area.

level), and S_n^z are also conserved in the linear regime, as the third component of the flavor isospins is not dynamical. Furthermore, for our initial condition $|\Psi_0\rangle$ in Eq. (2.3), $S_0^{\pm} = 0$ since the initial state has only components along z and also $S_0^z = 0$. Using these constraints, we finally have

$$\left[i\frac{d}{dt} + \mu\cos(\theta_i)S_1^z\right]\langle\sigma_i^{\pm}(t)\rangle = \mu\cos(\theta_i)\langle\sigma_i^z\rangle S_1^{\pm}(t) \quad . \tag{2.10}$$

By noting that the right hand side is proportional to $\cos(\theta_i)\langle\sigma_i^z\rangle$, the solutions take the general form [165, 164],

$$\langle\sigma_i^{\pm}(t)\rangle = \frac{A_\omega\cos(\theta_i)\langle\sigma_i^z\rangle}{\omega + \mu\cos(\theta_i)S_1^z}e^{-i\omega t} \ , \tag{2.11}$$

with coefficient A_ω independent of i, and ω corresponds to the eigenvalues of the matrix $\mathcal{M}$ from Eq. (2.5). Inserting these solution into Eq. (2.10), together with the condition $S_0^{\pm} = 0$,

the eigenvalues satisfy,

$$1 = \frac{\mu}{N}\sum_{j=1}^{N}\frac{\cos(\theta_j)^2\langle\sigma_j^z\rangle}{\omega+\mu\cos(\theta_j)S_1^z} \qquad \text{and} \qquad 0 = \frac{\mu}{N}\sum_{j=1}^{N}\frac{\cos(\theta_j)\langle\sigma_j^z\rangle}{\omega+\mu\cos(\theta_j)S_1^z}\ . \tag{2.12}$$

Two types of solutions can be identified: a uniform solution corresponding to $\omega = 0$ with amplitudes essentially independent of the propagation direction θ_i, and coherent solutions corresponding to higher frequencies and for which the eigenfunctions in Eq. (2.11) have amplitudes that are correlated with the propagation direction. The presence of a collective mode with $\omega = 0$ has already been pointed out [164], but it's structure was connected to the presence of amplitudes with $\cos(\theta_j) = 0$ which we do not have. For our initial conditions however, this mode is still physical thanks to the fact that S_0^z vanishes.

2.3 Dynamical Quantum Phase Transitions Introduction

Quantum phase transitions are typically a result of non-analyticities of free energy in equilibrium systems, where some physical observable of the system serves as a tuning parameter driving the system over a transition threshold [173]. Smooth phase transitions, such as crossovers, have long been of interest to the nuclear community since the Bardeen-Cooper-Schrieffer- Bose-Einstein condensation transition realization, due its theoretical potential of manifesting in neutron stars; see Ref. [174] for a review. What these phase transitions have in common however, is their emergence via the tuning of some time-independent physical parameter—be it magnetization, interaction strength or temperature—causing the system to move through critical points in its phase diagram.

Analogous to modulating static observables to achieve phase transitions in systems at equilibrium, in systems far from equilibrium, phase transitions that can be identified by observables behaving non-analytically in time are termed Dynamical Quantum Phase Transitions (DQPT) [166]. This is the defining feature of DQPTs: the out of equilibrium states—such as those occurring within CCSN processes—transpires via time evolution of the system. They are distinguished by zero-crossings of the time-derivative of some measurable quantity: for this work we use Loschmidt Echo-defined DQPTs. Studies of systems in which DQPTs arise have seen advancement on a many fronts, from classifying coupling regimes

and universality classes[175], to experimental realizations[176]. For an introduction to and review of theoretical progress on DQPTs see Ref.[167].

When studying real-time dynamics of an initial state $|\Psi(t=0)\rangle$ generated by a Hamiltonian H,

$$|\Psi(t)\rangle = e^{-itH}\,|\Psi(0)\rangle\,, \tag{2.13}$$

it is convenient to describe the evolution as a two step process: for time $t<0$, the system is prepared in the ground-state of some initial Hamiltonian $H_{\mathcal{I}}$ and allowed to evolve trivially under the action of $e^{-itH_{\mathcal{I}}}$; at time $t=0$, the Hamiltonian is instantaneously changed to H, and the system is evolved forward in time. This process of instantaneously changing the Hamiltonian $H_{\mathcal{I}} \to H$ at some $t=0$ is commonly called a "quantum quench". "Quenching" a system can include anything from suddenly turning on a $\vec{B}$ field, to altering some aspect of the system's geometry. For a review of quenches and recent theoretical advances, see Refs. [177, 178].

As initially proposed in Ref. [166], the Loschmidt Echo $\mathcal{L}(t)$ [179] can measure the wavefunction overlap across a quench. It is defined as

$$\mathcal{L}(t) = |\langle\Psi(t)|\Psi(0)\rangle|^2 = \left|\langle\Psi(0)|e^{-itH}|\Psi(0)\rangle\right|^2 = e^{-N\lambda(t)}\,, \tag{2.14}$$

and can be interpreted as probing the likelihood that the system returns to the initial state $|\Psi(0)\rangle$ after the quantum quench. In this setting, a DPT can be detected by the formation of a zero in $\mathcal{L}(t)$, which corresponds to a divergence in the rate $\lambda(t)$, as the system reaches the thermodynamic limit [166, 167].

The discussion of DPTs becomes more involved when the initial ground-state is degenerate, as in our model. Here we present the required generalization proposed in Ref. [169], and used already in the collective neutrino oscillation setting in Ref. [126]. Assume that $H_{\mathcal{I}}$ has two degenerate ground states: $|\Psi_\alpha\rangle$ and $|\Psi_\beta\rangle$, and we initialize our system $H_{\mathcal{I}}$ at $t \to -\infty$ to $|\Psi_\beta\rangle$. Then, at $t=0$, we apply a quench to the system, where we instantaneously change $H_{\mathcal{I}} \to H$, and then time evolve $|\Psi_\beta\rangle$ under the quenched H. Two separate Loschmidt echoes can be defined,

$$\mathcal{L}_{\beta,\beta}(t) = \left|\langle\Psi_\beta|\,e^{-itH}\,|\Psi_\beta\rangle\right|^2 \qquad \mathcal{L}_{\alpha,\beta}(t) = \left|\langle\Psi_\alpha|\,e^{-itH}\,|\Psi_\beta\rangle\right|^2\,, \tag{2.15}$$

where the first, $\mathcal{L}_{\beta,\beta}(t)$, is analogous to the previous definition of the Loschmidt echo from Eq. (2.14), while the second, $\mathcal{L}_{\alpha,\beta}(t)$, corresponds to the probability of transitioning to the orthogonal ground-state $|\Psi_\alpha\rangle$. The full out-of-equilibrium partition function is then defined as the sum of the two Loschmidt echoes [169].

Similar to the discussion of slow-modes in a neutrino system [126], for the work discussed in this chapter, the Loschmidt echo crossing times that we compute are associated with the two ground states $|\Psi_\alpha\rangle$ and $|\Psi_\beta\rangle$,

$$|\Psi_\alpha\rangle = \left(\bigotimes_{n=1}^{N/2} |\uparrow\rangle_n\right) \otimes \left(\bigotimes_{m=N/2+1}^{N} |\downarrow\rangle_m\right) \tag{2.16}$$

$$\tag{2.17}$$

$$|\Psi_\beta\rangle = \left(\bigotimes_{n=1}^{N/2} |\downarrow\rangle_n\right) \otimes \left(\bigotimes_{m=N/2+1}^{N} |\uparrow\rangle_m\right) \ , \tag{2.18}$$

where we took the state $|\Psi_\beta\rangle$ as the initial state for evolution at the quench, which is the same as the initial state $|\Psi_0\rangle$ from Eq. (2.3) that is used in the linear stability analysis of Sec. 2.2. For N even, these are degenerate ground states of an initial Hamiltonian $H_{\mathcal{I}}$,

$$H_{\mathcal{I}} = \sum_{i=1}^{N/2} \sum_{j=N/2+1}^{N} \sigma_i^z \sigma_j^z \ . \tag{2.19}$$

At $t = 0$, the system is quenched to evolve under the Hamiltonian $H_{\nu\nu}$ given in Eq. (2.2). The initial state $|\Psi_\beta\rangle$ is evolved forward, with overlaps onto itself and onto $|\Psi_\alpha\rangle$ computed, and the first crossings of the Loschmidt echos, $\mathcal{L}_{\alpha,\beta}(t)$ and $\mathcal{L}_{\beta,\beta}(t)$, are subsequently determined.

We now introduce the Loschmidt rate function $\lambda(t)$, which is related to $\mathcal{L}(t)$ as:

$$\lambda(t) = -\frac{1}{N} \log[\mathcal{L}(t)], \tag{2.20}$$

for a system with N particles. In such a system, with $\mathcal{L}_{\beta,\beta}(t)$ and $\mathcal{L}_{\alpha,\beta}(t)$, we define a corresponding $\lambda_{\beta,\beta}(t), \lambda_{\alpha,\beta}(t)$.

As initially discussed in [180, 181], $\lambda(t)$ is an intensive quantity which, in the thermodynamic limit of infinitely many particles $N \to \infty$, will be dominated by one of the two rate functions $\lambda_{\beta,\beta}(t), \lambda_{\alpha,\beta}(t)$ [166, 169]. This leads us to the following overall rate function $\lambda_N(t)$ for a system with N neutrinos, as introduced in [169]:

$$\lambda_N(t) = \min(\lambda_{\beta,\beta}(t), \lambda_{\alpha,\beta}(t)) \tag{2.21}$$

Nonanalyticities in the rate function $\lambda_N(t)$ occur when a previously dominant rate function (say, $\lambda_{\beta,\beta}(t)$) is overtaken by the other rate function (say $\lambda_{\alpha,\beta}(t)$), which causes a kink in $\lambda_N(t)$ [166, 169, 167], see the left panel of Fig. 2.2. Following directly from Eq.(2.20), the critical time at which a DQPT can occur, therefor, is when one Loschmidt echo $\mathcal{L}_{\alpha,\beta}(t)$ overtakes the other $\mathcal{L}_{\beta,\beta}(t)$ [169, 168], which manifests as an intersection of the two Loschmidt echo spectra identified by a crossing time $t_{\mathcal{L}_\times}$ [169]:

$$\mathcal{L}_{\alpha,\beta}(t_{\mathcal{L}_\times}) = \mathcal{L}_{\beta,\beta}(t_{\mathcal{L}_\times}), \tag{2.22}$$

The overall rate function's Eq.(2.21) inflection points manifest whenever the system suddenly alternates in probability of reaching $|\Psi_\alpha\rangle$ or $|\Psi_\beta\rangle$. Hence choosing the proper $H_{\mathcal{I}}$ which has two degenerate ground states is essential when characterizing DQPTs via $\mathcal{L}(t)$, as first acknowledged in [166, 169]. Now what we are actually interested in is the natural logarithm value of the time at which Eq. (2.22) occurs, which we represent as:

$$w_\times = \ln t_{\mathcal{L}_\times}. \tag{2.23}$$

With this definition, a non-analytic behavior, and thus a DPT, can present itself as a "kink" in the free energy when the dominant rate function switches between $\lambda_{\beta,\beta}(t)$ and $\lambda_{\alpha,\beta}(t)$ at some crossing time $t_{\mathcal{L}_\times}$. We display this behavior for a system of neutrinos with $N = 12$ neutrinos evolving under the Hamiltonian in Eq. (2.2) in Fig. 2.2. The left panel shows the two rate functions $\lambda_{\beta,\beta}(t)$ and $\lambda_{\alpha,\beta}(t)$ as a function of time, with the inset focusing on the kink in $\lambda_N(t)$ formed by their crossing. The same behavior is of course paralleled by the crossing of the Loschmidt echoes, as shown in the right panel of Fig. 2.2.

2.4 Analysis of Loschmidt Echo Crossing Times

Ensembles of independent $\mathcal{J}_{ij}$ configurations with $N = 4, 6, 8, 10, 12$ and 14 neutrinos were generated using Monte Carlo uniform sampling in θ_i for $0 \leq \theta_i \leq 0.5$. These provided ensembles of $H_{\nu\nu}$ defined in Eq. (2.2). The initial state in Eq. (2.18) was evolved forward in time for each member in an ensemble, and the times of the first crossing of the Loschmidt echos $\mathcal{L}_{\alpha,\beta}(t)$ and $\mathcal{L}_{\beta,\beta}(t)$, given in Eq. (2.15), were determined. For the systems with $N \leq 10$, the systems could be evolved in time and the Loschmidt echos determined exactly using

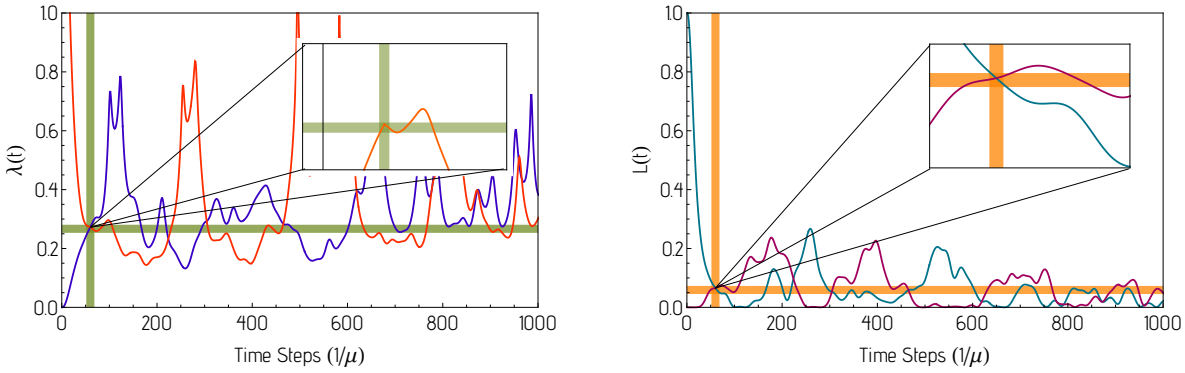

Figure 2.2: The left panel shows $\lambda_{\beta,\beta}(t)$ (red curve) and $\lambda_{\alpha,\beta}(t)$ (blue curve) as a function of time in units of μ^{-1}. The thick green lines mark the time when the rate functions first cross. The inset zooms in on the lowest-λ's first (non-analytic) cusp. The right panel shows $\mathcal{L}_{\beta,\beta}(t)$ (teal curve) and $\mathcal{L}_{\alpha,\beta}(t)$ (purple curve). Orange lines mark the first crossing time, $t_{\mathcal{L}_\times}$, in units of μ^{-1}, with the inset focusing on the evolution around $t_{\mathcal{L}_\times}$.

`Mathematica`, without the need for time decimation. For larger systems (and the smaller systems for verification purposes), matrix product states (MPS) were used to simulate dynamics via `iTensor`'s `Julia` package [182] using Trotterization of the evolution operator, implemented via the Time Evolving Block Decimation (TEBD) method [183, 52, 184], with a tolerance of 10^{-9}. For the simulations in this work, an MPS truncation error cut off of 10^{-9} was used, which meant that for each SVD the lowest m singular values λ_n were thrown out, such that: [182]

$$\frac{\sum_{n=1}^{m} Min(\lambda_n^2)}{\sum_{n=1}^{N}(\lambda_n^2)} < 10^{-9} \tag{2.24}$$

and occurred $\binom{N}{2}$ times in each time step. A step size of $\tau = 0.05\mu^{-1}$ for a total time evolution time of $t_{max} = 50.0\mu^{-1}$ (or 10^3 τs) was used for each system with unique $\mathcal{J}_{ij}$ for the analysis in the main text, while step sizes of $\tau = [0.02\mu^{-1}, 0.07\mu^{-1}, 0.1\mu^{-1}]$ were also profiled. A maximum evolution time interval of $50\,(2N/\mu)$ was selected, with a Trotter step size of $\Delta t = 0.05\,(2N/\mu)$ [1]. This was guided by previous numerical results [148, 149] which demonstrated collective flavor oscillations taking place on time scales typically ranging from

[1] Step sizes of $\Delta t = [0.02, 0.07, 0.1]\,(2N/\mu)$ were also profiled, and furnished consistent results.

$t_{slow} = \mu^{-1}\sqrt{N}$ to $t_{fast} = \mu^{-1}\log(N)$. To account for the increased complexity in the system introduced by our random selection of neutrino momenta, the maximum simulation time was increased by 10×, as similarly estimated in Ref. [122].

The observed heavy tails of the obtained distributions, reminiscent of those found in lattice QCD calculations of baryon correlation functions (see, e.g., Ref. [185]), prompts us to change variables from $t_{\mathcal{L}_\times}$ to $w_\times$, where

$$w_\times \;=\; \log t_{\mathcal{L}_\times} \quad . \tag{2.25}$$

Figure 2.3 displays the associated histograms as functions of $w_\times$ (with uniform bins width) for each N. As the systems are evolved forward in time up to a maximum time, $T_{\max}$, there are a small number of elements in the ensembles that do not experience a Loschmidt Echo crossing (during that time interval). Qualitatively, for the sizes of ensembles we have generated, the $N = 4$ system exhibits a single skewed distribution, with a heavy tail for increasing $w_\times$. The $N > 4$ systems show the emergence of a second peak on the shoulder of the first.

For small system sizes, the discreteness of the systems furnish "sectors" of Loschmidt echo crossing times, as suggested in Fig. B.1. As a result, the distributions are not expected to be smooth functions for small N. However, they are expected to become smooth with increasing N. Therefore, fitting to smooth functions should describe results for large N, but become increasingly poor descriptions at small N. In order to quantify these distributions, the sum of two stable distributions are fit to each histogram, in particular, type-1 stable distributions,

$$h(w) \;=\; a_1\mathcal{S}_1(\alpha_1,\beta_1,\mu_1,\sigma_1,w) \;+\; a_2\mathcal{S}_1(\alpha_2,\beta_2,\mu_2,\sigma_2,w) \;, \tag{2.26}$$

where a_i denote their amplitudes and are real numbers. As defined in `Mathematica`, the type-1 stable distribution is,

$$\begin{aligned}\mathcal{S}_1(\alpha,\beta,\mu,\sigma,x) \;&=\; e^{i\mu t-|t\sigma|^\alpha\left(1-i\beta\tan\left(\frac{\pi\alpha}{2}\right)\,\mathrm{sgn(t)}\right)} \;:\; \alpha\neq 1 \\ &=\; e^{i\mu t-t\sigma\left(1+2i\frac{\beta}{\pi}\log|t|\,\mathrm{sgn(t)}\right)} \;:\; \alpha = 1 \quad ,\end{aligned} \tag{2.27}$$

where $\mathrm{sgn}(x)$ is the sign of x. α is the stability parameter, β is the skewness parameter, μ is the mean of the distribution, and σ is twice the variance. The results of fitting $h(w)$

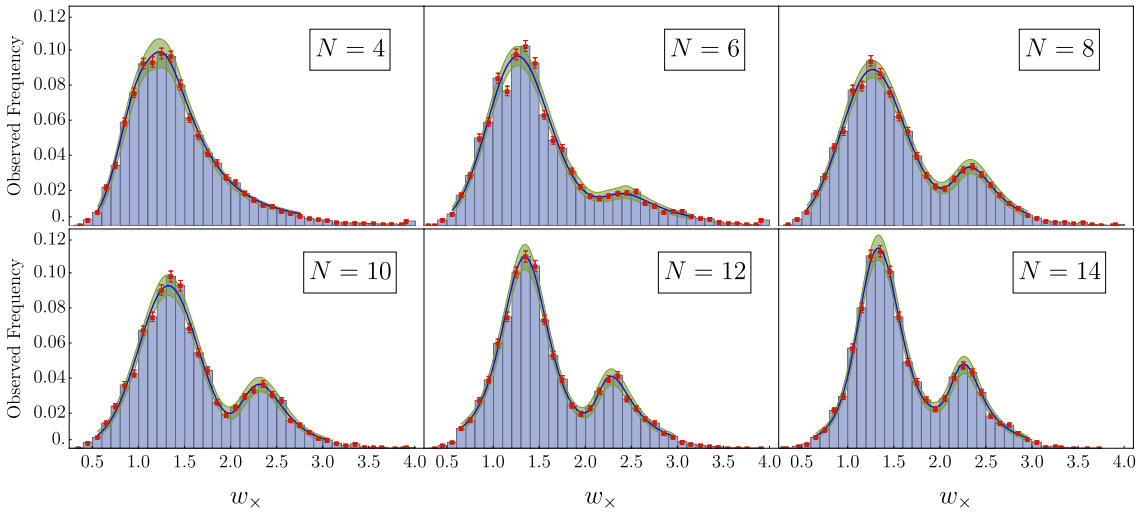

Figure 2.3: Histograms of the Loschmidt-echo crossing times for system sizes of $N = 4, 6, 8, 10, 12$ and 14 neutrinos evolving under the dynamics described in the text. They show the number of events in a given bin normalized to the total number of events, as a function of $w_\times$, defined in Eq. (2.25). A bin width of $\delta w_\times = 0.100$ is employed in each histogram. All distributions were formed from 10.5k independent samples of $\mathcal{J}_{ij}$. The red points with error bars correspond to the height of each bin and uncertainty estimated by bootstrap re-sampling over the 10.5k independent samples. The dark-blue curves show the best fit of the sum of two stable distributions (given in Eq. (2.26)) to the histograms, with fit parameters and uncertainties given in Table 2.1. The 68% confidence intervals associated with the fits are shown by the green-shaded regions.

in Eq. (2.26), with a total of 10 fit parameters, are shown in Table 2.1, including the uncorrelated weighted χ^2/dof to indicate the goodness of fit. Monte Carlo sampling was used to perform the fitting and in determining the 68% CIs. For each histogram, the global minimum of the uncorrelated weighted χ^2/dof [2] was found by a search in the 10-dimensional parameter space, first using a coarse lattice of points then followed by a stochastic gradient descent. The 68% CI was determined by sampling parameter space to identify the surface for which $\chi^2_{\rm min} \to \chi^2_{\rm min} + 11.55$, appropriate for a 10 parameter fit. In some instances, a second minimum lay within this upper value of χ^2, giving outliers in the sampling. Their impact

[2]The weights corresponded to the inverse variance of each histogram bin, determined by bootstrap re-sampling.

N	a_1	α_1	β_1	μ_1	σ_1	a_2
4	0.0849(54)	1.34(10)	0.976(76)	1.64(16)	0.275(23)	0.0231(29)
6	0.0840(35)	1.842(86)	0.914(61)	1.333(35)	0.2474(93)	0.0184(11)
8	0.0793(29)	1.866(81)	0.918(41)	1.326(37)	0.2531(96)	0.0231(11)
10	0.0785(27)	1.854(86)	0.0785(41)	1.330(23)	0.2397(91)	0.0230(10)
12	0.0843(36)	1.349(83)	0.00277(15)	1.346(21)	0.2268(9)	0.0237(12)
14	0.0771(31)	1.447(72)	0.213(12)	1.389(25)	0.1966(76)	0.0283(15)
N	α_2	β_2	μ_2	σ_2	χ^2/dof	
4	0.892(43)	0.621(76)	0.35(31)	0.313(34)	2.03	
6	1.049(20)	0.389(28)	4.32(66)	0.358(22)	6.54	
8	1.175(62)	0.468(22)	2.76(16)	0.226(11)	1.69	
10	1.366(78)	0.898(59)	2.630(90)	0.1893(88)	3.56	
12	1.121(57)	0.613(35)	2.97(27)	0.1952(99)	2.01	
14	1.079(48)	0.313(16)	2.80(27)	0.1987(83)	2.31	

Table 2.1: Best-fit parameters obtained from fitting two stable distributions, given in Eq. (2.26), to the histogram distributions of Loschmidt echo crossing times for systems with $N = 4, 6, 8, 10, 12, 14$ neutrinos, as displayed in Fig. 2.3. The histogram bin size is $\delta w_\times = 0.100$. All distributions were formed from 10.5k independent samples of $\mathcal{J}_{ij}$.

was mitigated by using the median average deviation (MAD) of the parameter sample, with an appropriate re-scaling factor (computed to be 4.855(9)). While the presented results use bin widths of $\delta w_\times = 0.100$, a range of bin widths were examined $\delta w_\times = 0.060, 0.065, ...0.140$, over which the resulting fit parameters were found to be consistent.

There are some interesting points to note from our results. First is that the locations of the two peaks, $\mu_{1,2}$, become approximately independent of the number of neutrinos, and the variances also appear to be approximately stable. Further, the relative strength of the two distributions appears somewhat stable to increasing neutrino number. The goodness-of-fit to two stable distributions depends on the number of neutrinos, as can be seen in the last

column of Table 2.1. For the systems with $N \geq 8$, there are two peaks in the histograms that are reasonably well reproduced by the sum of two stable distributions. However, as the $\chi^2/\text{dof} > 1$ for each, this does not constitute a perfect description of the systems, as expected. It is found to be a superior hypothesis to that of a single stable distribution for $N \geq 8$, which have $\chi^2/\text{dof} > 10$.

It is enlightening to compare the results for the Loschmidt echo crossings with the results of the stability analysis that we presented above, in particular the distributions of imaginary parts of the frequencies. In both instances, there are two peaks in the distributions associated with the sampled $\mathcal{J}_{ij}$ matrices. The slower and faster modes correspond to the long-time scale and short-time scale Loschmidt echo crossings, respectively. Interestingly, while the distributions associated with faster-modes and the shorter Loschmidt echo crossing times occur at the same $w_\times$, those associated with the slower modes (consistent with zero frequency) are at a desparately larger value of $w_\times$ than the corresponding longer Loschmidt echo crossing times. The well-separated slower- and faster-mode distributions differ from the overlapping distributions in the Loschmidt echo crossing times. So while the linear instability analysis describes well the fast modes, it is only qualitatively reflective of the longer Loschmidt echo crossing times.

2.5 Summary

Neutrinos play a key role in CCSN; after creation in the core, neutrino flavor evolves in complex ways through interactions with matter, with other neutrinos, and because the mass eigenstates are combinations of the weak eigenstates. Our work builds upon current research into the quantum evolution of model neutrino systems in the full many-body treatment. Starting with a tensor-product state of equal numbers of electron-type and heavy-type neutrinos, small- and modest-sized systems are evolved forward by the Hamiltonian describing neutrino-neutrino forward scattering, neglecting vacuum mixing. In this setting, the forward-scattering interactions with matter only contribute a global phase factor and are therefore neglected. Attention is paid to the time-scales for flavor conversion under this evolution, both through a linear stability analysis and also using the crossing of Loschmidt echos. We consider Loschmidt echo crossings because of their relation to dynamical phase

transitions in non-equlibrium systems.

Through Monte Carlo sampling over a uniform distribution in neutrino angles, we generate ensembles of neutrino coupling matrices in the context of an axially-symmetric light-bulb model. In our linear stability analysis, both zero-frequency and non-zero frequencies instabilities are found, while two modes are observed in the crossings of the Loschmidt echoes, both with finite time-scales. The locations of the peaks in the Loschmidt echo crossings appear independent of the number of neutrinos for $N \leq 14$. While the distributions for the $N = 4, 6$ systems reflect the underlying discreteness of the systems, we found that they become increasingly well described by smooth distributions, in particular the sum of two stable distributions. As a mean-field analysis identifies only one fast mode of flavor conversion for such systems, our fully quantum mechanical analysis has revealed the presence of a second mode. Further work is required to better understand the impact of this second mode, and its connection to the linear stability analysis. In future work, it would be interesting to understand the role played by the integrability of the axially-symmetric Hamiltonian, and whether a rich multi-peaked spectrum could be expected also in the chaotic multi-angle regime studied in Ref. [156]. In this context, the zero mode may potentially show it's presence in thermalizing systems as a quantum many-body scar, creating unusually long thermalization times.

2.6 Conclusions

Previous studies focusing on the neutrino-neutrino interaction term Eq. (1.9) in two-flavored systems have established the existence of multiple time scales of DQPTs in a given system with homogenous flavor momentum coupling angles $\mathcal{J}_{ij}$, and have utilized DQPTs to analyze systems similar to Eq.(A.16) [126, 121]. In earlier, formative work by Sawyer [150], differences in initial momentum and flavor distributions of a neutrino system produced two markedly different evolutionary behaviors, in both the amount of flavor converted and the timescales on which those conversions occurred. Systems similar to Eq.(1.9) have also produced dual phases and modes of behavior–from entanglement growth to collective flavor dynamics–in the two-flavor regime[129, 126, 121, 164].

We focused our attention on Eq.(A.16), where large angle ranges of heterogenous mo-

menta were taken for $\mathcal{J}_{ij}$. The θ_i composing $\mathcal{J}_{ij}$ were constrained to lie between $\theta_\Delta = [0.0, 0.5]$ radians, to ensure physically-relevant kinematics in the simplified bulb-model we followed. The downfall of constraining angle ranges to be smaller than θ_Δ risked exclusion of potentially non-trivial structures in the $\log t_{\mathcal{L}_\times}$ histograms.

For random uniform angular distributions populating $\mathcal{J}_{ij}$, simulations of $H_{\nu\nu}$ resulted in a statistically verified bimodal distribution of log-scaled Loschmidt echo crossing times $\log t_{\mathcal{L}_\times}$ to the order of the first crossing. The findings in Fig. 2.3 depict the presence of two distinct DQPT time scales in Eq.(A.16), persistent as N increased. What we find novel, however, is the asymptotic behavior of the separation between the two modes, as suggested by Fig. 2.3: as neutrino number N grew, each centroid's amplitude $\mathrm{a}_1, \mathrm{a}_2$ steadily increased, the variance at each mode mean decreased, and the mean estimates themselves remained relatively stable, demonstrating not only the distribution's persistence but also suggesting asymptotic behavior when system size is taken to the thermodynamic limit $N \to \infty$. Simulations indicated that the number of neutrino angle cones–which scaled with N–had no bearing on the number of distinct DQPT time scales, of which there were consistently two. Similar qualitative behavior in $\log t_{\mathcal{L}_\times}$ distributions were found when using other angular distributions to populate $\mathcal{J}_{ij}$ in this work.

When exploring lepton-number dispersion measures as a potential initial state discriminator, we saw a gradual formation of two independent modes in density plots of the CFC frequency's discriminant ϑ Eq.(D.6). Recent work by Roggero [126] was the first to observe DQPTs' precipitative effect on CFCs in neutrino models similar to Eq.(A.16). When Eq.(A.16) is simulated over large angular ranges of heterogenous $\mathcal{J}_{ij}$ flavor momenta, a bimodal distribution of $\vartheta(\log t_{\mathcal{L}_\times})$ materializes and partitions in the same temporal region as histograms of $\log t_{\mathcal{L}_\times}$, with the partition location remaining stable as N increased. Particularly close attention was given to ϑ Eq.(D.6) due to its deterministic role in whether Ω Eq.(D.4) is complex or real valued, which can affect instability growth. The similar bimodal structures of distributions in Fig.2.3 and Fig.D.1 suggest an initial-state dependent observable potentially predictive of $t_{\mathcal{L}_\times}$ occurrences if ϑ is very negative. For the N we surveyed, below -0.0250 appears to be correlated with $t_{\mathcal{L}_\times}$s in the first mode of the bimodal histograms of $\log t_{\mathcal{L}_\times}$, regardless of N. This soft cutoff is somewhat arbitrary, whether it

is related to system size or other factors is currently undetermined in this work, and is left for future work. Understanding why low negative values of ϑ are more correlated with $t_{\mathcal{L}_\times}$s in the first centroid of Fig.2.3 could be accomplished by studying systems $N > 14$, or by analyzing ϑ with respect to $t_{\mathcal{L}_\times}$s occurring beyond the first. Comprehensive understanding of the relationship between DQPTs and CFCs is necessary and should be explored in more physically realistic models, and can potentially contribute to recent investigations into the role of CFCs modulating astrophysical phenomena such as nucleosynthesis.

Previous work has indicated primordial neutrino flavor conversion's potential to affect the relative abundances of protons and neutrons in the early universe [17, 186], which can consequently inhibit or amplify big bang nucleosynthesis (BBN). Within the context of CCSN nucleosynthesis (CCSNN), flavor evolution within neutrino-driven winds can affect CCSNN in CCSN ejecta, where the evolution of flavor concentrations can play a non-trivial role in stymieing or encouraging rapid neutron capture processes (r-processes) as described in previous work by [187, 188, 189]. Analyzing the potential impact of CFCs on nucleosynthesis[190, 191, 192, 193] however is a recent development, made possible by Sawyer's first works on the subject [150]. Additional out-of-equilibrium analyses of late-time collective neutrino flavor dynamics is therefor necessary for understanding initial state conditions conducive for BBN and CCSNN. The initial flavor composition necessary for DQPTs to occur and in turn how DQPTs affect late-time collective flavor evolution necessitates further exploration–given r-process's dependence on the concentrations of ν_e in neutrino-driven winds–and will be the subject of future work.

Far-from equilibrium analyses in neutrino systems and studies on how they affect the late-time behavior of flavor evolution is a relatively contemporary integration into neutrino studies [121, 121, 122], particularly given the recent identification of DQPTs[167, 121, 121, 122]. Computational tools long familiar in the condensed matter community and analysis techniques fundamental to QIS holds significant potential for gaining insight into the quantum correlations and many-body dynamics underpinning late-time collective flavor evolution in neutrino systems, emphasized more so by collective CFCs comparatively recent theorization [23, 194]. A more holistic understanding of how system attributes that give rise to DQPTs can also affect collective CFCs can be achieved via exploration of more

realistic models. This can take shape via consideration of a variety of features that had been neglected for simplicity in this work: from inclusion of neutrino–matter interactions and extending the study to three-flavored neutrino systems, or the accounting of neutrinos trajectories $\frac{\vec{p}_{k_z}}{|\vec{p}_k|}$ not restricted to be axisymmetric about a $\hat{z}$ orthogonal to the neutrino emission surface.

Investigating the entanglement structure and growth around $t_{\mathcal{L}_\times}$ in $H_{\nu\nu}$ Eq.(A.16)–along with flavor persistence–in order to fully understand the two distinct DQPT timescales and CFC modes' presences will be necessary. This entanglement investigation, along with another study probing the manifestation of scramblers in this two-flavored neutrino system, are the subject of forthcoming work.

Chapter 3

SCRAMBLING IN NEUTRINO SYSTEMS

3.1 Introduction

Current experimental advances in engineering quantum simulation platforms such as trapped ion or ultra-cold atomic-based systems have enabled great progress in realizing a wide range of far-from-equilibrium phenomena[195, 196, 197], particularly those ranging from strong to weak violations and demonstrations of the eigenstate thermalization hypothesis (ETH).

The Out-of-time ordered correlator (OTOC) has arisen as a powerful diagnostic tool for emergent far-from-equilibrium and chaotic phenomena arising in such realizable spin systems. The OTOC is a four-point correlation term, the expectation value of the squared commutator of two operators $V, W(t)$ where $W_t = e^{iHt}We^{-iHt}$ and $W_t^\dagger = e^{iHt}W^\dagger e^{-iHt}$ are Heisenberg operators. Conventionally, they contain three separate time-reversal operations and probe the information spread within a system, but they can contain more, and probe other observables like stabilizer Renyi Entropy[198]. The OTOC is defined as[199]:

$$F(t) = \langle\psi_i| W_t^\dagger V^\dagger W_t V |\psi_i\rangle = \langle\psi_i| e^{i\hat{\mathcal{H}}t}We^{-i\hat{\mathcal{H}}t}Ve^{i\hat{\mathcal{H}}t}We^{-i\hat{\mathcal{H}}t}V |\psi_i\rangle$$

where V, W can or can not commute, are unitary, and do not need to be Hermitian.

Previous investigations have probed the OTOC's potential as a witness for quantum phase transitions in models ubiquitous in condensed matter such as the Transverse Field Ising (TFI) Model, the transverse axial next nearest neighbor Ising (TANNNI), the Lipkin-Meshkov-Glick (LMG) model rendered as a fully connected transverse Ising chain [200, 201, 202, 203, 204], as well as a witness for topological phase transitions [205] which were also studied in primarily Su-Schreiffer-Heeger (SSH), Creutz and other lattice models. OTOCs have also been used a probe for many-body localization [206, 207], measuring magic[208], scars[209, 210], and operator purity[211]. Investigations probing the connection between OTOCs and phase transitions have been conducted in a wide variety of systems ranging

from nearest-neighbor, and next-nearest-neighbor, to all-to-all connectivity, though largely confined to Ising spin models. There has been limited work on systems containing continuous spin rotations and long-range connectivity (cite).

Given the wide range of physical observables and far-from-equilibrium phenomena[212, 213, 214, 215, 216] for which the OTOC has been used as a diagnostic tool and the wide range of spin models previously investigated, we are interested in the potential of the OTOC as a dynamical quantum phase transition (DQPT)[166, 167, 168] diagnostic in long-range entangled Heisenberg spin chains whose couplings are subject to constraints originating from the many-body neutrino model. Previous work has shown non-trivial DQPT occurrence timescales in families of such Hamiltonians[132], where distinct structures emerge after high-statistics analysis.

In this work, we are interested in studying a specific family of random-coupled long-range entangled Heisenberg models, following the form of Eq. 1.7, where the angles constituting the coupling matrix $\mathcal{J}_{ij}$ are sampled from random uniform distributions as described in Table G.1. Constraints on the coupling terms in this model are motivated by neutrino many-body systems close to the supernova core, in this case narrowing the study's scope to relatively tight angular ranges mimics. By focusing on forward-peaked uniform angular distribution of θ_i which are randomly sampled uniformly on the interval $[0, 0.5]$, false degeneracies[38, 156] in Eq. (1.7) can be prevented.

Quantum information scrambling dynamics have not been studied in many-body neutrino systems–or for neutrino systems in general–in the current literature to date, and is thus a uniquely novel observable to consider, particularly in the context of neutrino systems close to the CCSN core where 99% [217] of the energy is emitted through neutrino emission from the proto-neutrino core. This released energy affects a wide variety of macroscopic processes including heating, and shock revival. Neutrino flavor transformation (oscillation) directly affects these macroscopic observables.

In the computations of DQPTs and OTOCs in this work, the initial states are constructed as tensor-products of N neutrinos, made up of $N/2$ electron and $N/2$ heavy flavor neutrinos, and are each defined as Eq. 2.3. These are a commonly used state in many-body flavor dynamics studies [132, 126, 121, 154, 37] to focus on dynamics beyond the mean-field

regime as the states $|\Psi_\alpha\rangle, |\Psi_\beta\rangle$ are invariant under mean-field evolution. We define DQPTs similarly as we do in the previous chapter, via the Loschmidt Echo crossing times (2.23), for the same initial states as in (2.18), as done in [132].

We note the deep connection between DQPTs and Fisher zero crossings. The DQPT itself is often regarded as a partition function in time, while Fisher zeros are when the partition function equals 0 in the complex temperature plane. For DQPTs, when extending the Loschmidt echo out into the complex time domain, as Fisher zeros accumulate on the x-axis, their location (on the real time axis) indicates when the system experiences a DQPT. We refer the reader to available reviews for more details on the backgroud of Fisher zero crossing's connection to DQPTs (see Ref. [167] for a review).

In Sec. 3.2, the results obtained for the Loschmidt echoes crossing time for an ensemble of neutrinos systems with sizes ranging from $N = 4$ to $N = 10$ are presented. A statistical analysis of the observed time scales is forthcoming, along with a more detailed analytical assessment of the observed phenomena, and scaled-up numerical simulations which cover a wider variety of system and operator parameters surveyed. In Sec. 3.3 we discuss future analytical directions to help guide a more formal understanding of the phenomena witnessed in Sec. 3.2.

3.2 Preliminary Numerical Results

In this section, we studied the relationship between when a particular system achieved its first full scrambling. The time at which a system becomes fully scrambled is defined by that system's OTOC spectrum crossing the x-axis (or reaching the value of 0), and when that system experienced its first DQPT (as defined by Loschmidt echos).

There were several parameters to vary in the numerical exploration of a system's first occurrence of a DQPT and when the OTOC fully scrambled. First was system size N–we present numerical results for $N = 4 - 18$ in this document. The next relevant parameter was the site locations at which operators V and W acted on. The third was the operator that was used for V and W.

For Figures 3.1, 3.2, we held the locations of V, W fixed, as well as the V, W's actual operators, which were both spin-Z, and varied only size. We note that high stats were

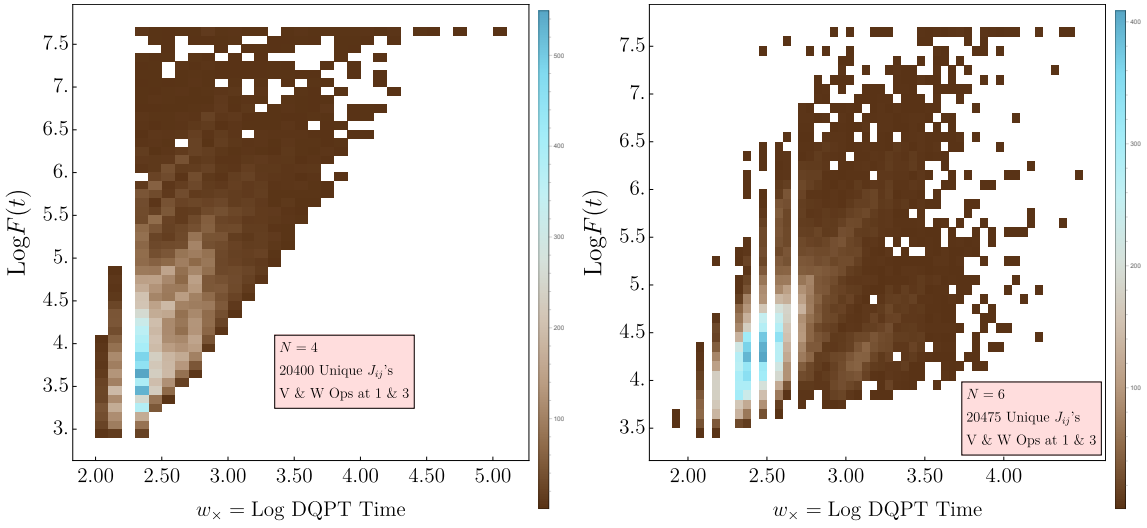

Figure 3.1: Density histogram with bin number 42, for 20k $N = 4, 6$ neutrino systems with unique J_{ij} couplings for the Out-of-Time-Ordered-Correlator (OTOC) as denoted by $\log(F(t) = 0)$ as a function of the first Loschmidt Echo Crossing time $w_\times$. Operators were on sites 1 & 3.

necessary for meaningful plots, and emphasize that only after time evolving over 10k unique systems for $N = 4$ (Fig. 3.1), were we able to see nontrivial structures appear. We increased system size while we held everything else constant (V, W locations and V, W definitions). Figures 3.1, 3.2 all contain the maximum number of samples.

For each density histogram shown in Figures 3.3, 3.4, systems were evolved for 2000 time steps with step size $dt = 0.05$. For each system, Eq. (3.1) was calculated for each dt. The resulting spectra of Eq. 3.1 for each system was then searched for the time at which the system fully scrambled, which the current literature defines as when Eq. 3.1 $= 0$. The natural log of this time, t_{scramble} was then plotted as a function of Eq. (2.23), and then the subsequent scatter plot was converted to a density histogram.

For reference, we have included another set of figures with lower statistics (only 8k samples each in Figures 3.3, 3.4 to further underscore the importance of studying increasingly larger families of Eq. (1.7) as the system size N increases. This is necessary to clearly understand if the nontrivial behavior seen in Fig. 3.1 is due to finite size effects, or if it is a genuine novel feature that emerges only after taking a broad sample set family of Eq. (1.7),

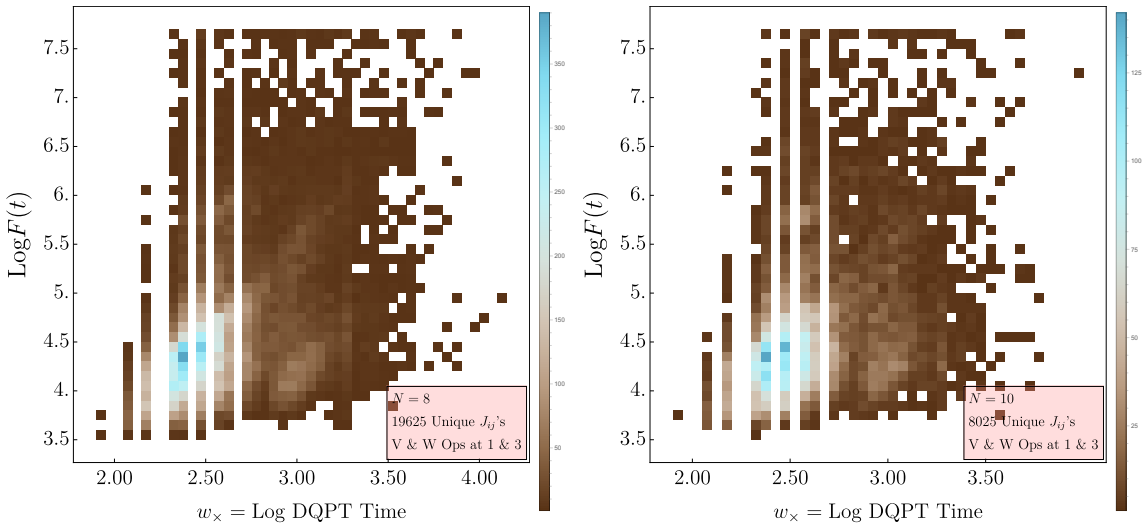

Figure 3.2: Density histogram with bin number 42, for 19k $N = 8$ neutrino systems and 8k $N = 10$ neutrino systems with unique J_{ij} couplings, for $\log(F(t) = 0)$ as a function of the first Loschmidt Echo Crossing time $w_\times$. Operators were on sites 1 & 3.

for a given system size. We also made sure to only probe with operators acting at the first and second sites on the spin chain. Now we can focus on the structures that we see within Fig.3.3.

The resulting Figures 3.1, 3.2 demonstrate an emerging power-law scaling relationship between t_{scramble} and Eq. (2.23), as well as contain what appears to be multiple modes emerging, all oriented along the diagonal. All figures have the bright blue concentrated mode at roughly $2.5 = w_\times$ and $4.5 = \ln(F(t) = 0)$. We note that this does not appear to shift in any direction as system size increases either, though we are not sure yet if this something that would change if more systems are incorporated in studies for $6 \leq N$.

3.3 Towards An Analytical Description

Developing an analytical connection between OTOCs and DQPTs in all-to-all connected random Heisenberg two-level spin chains would result in a robust understanding of how DQTPs occurrence times and scrambling as defined with OTOCs are related to one another, as well as lend a deeper explanation behind the power-law scaling witnessed in Figures 3.1

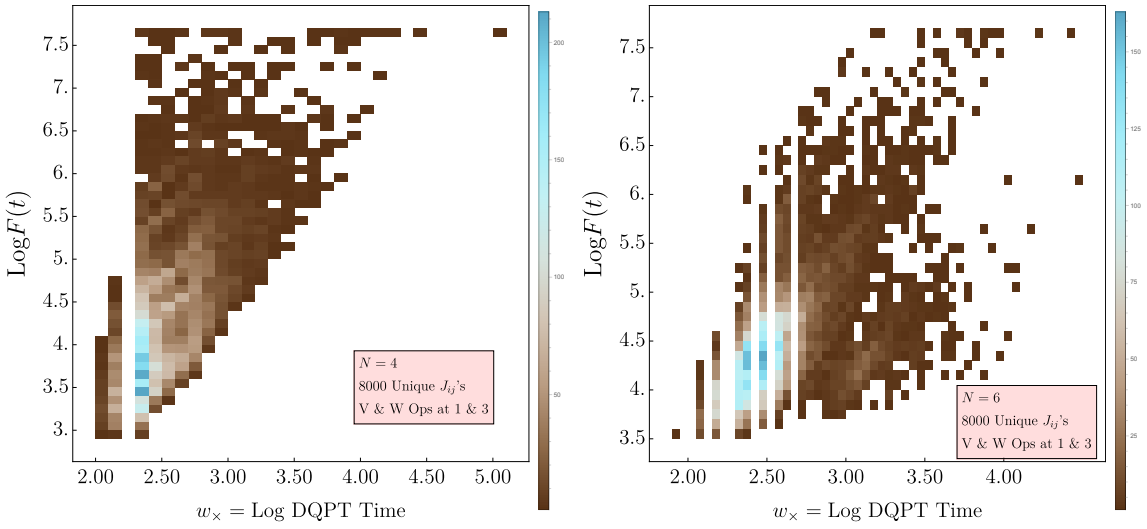

Figure 3.3: Density histogram with bin number 42, for 8k $N = 4$ neutrino systems with unique J_{ij} couplings for the Out-of-Time-Ordered-Correlator (OTOC) as denoted by $\log(F(t) = 0)$ as a function of the first Loschmidt Echo Crossing time $w_\times$. Operators were on sites 1 & 3.

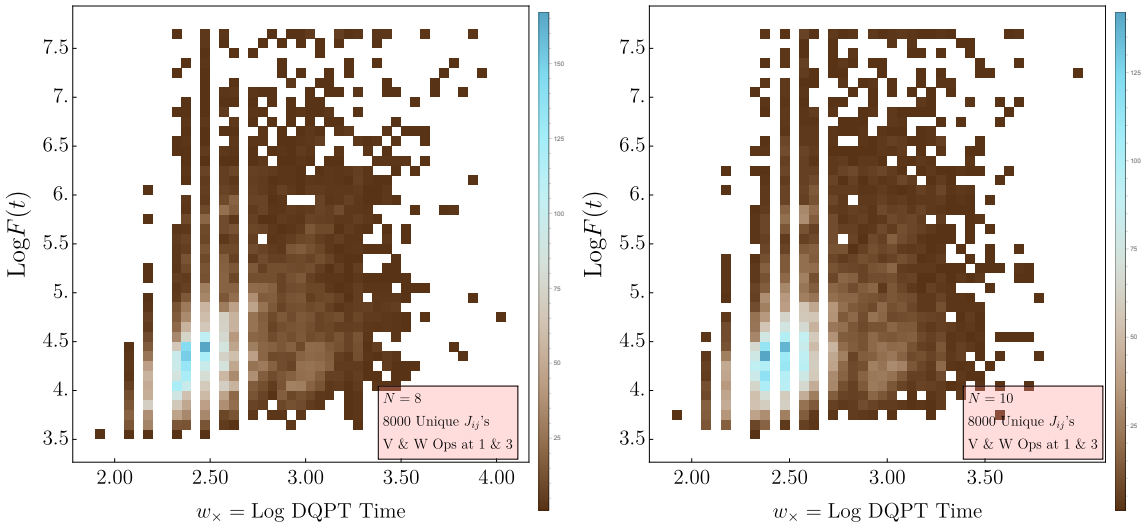

Figure 3.4: Density histogram with bin number 42, for 8k $N = 8$ neutrino systems with unique J_{ij} couplings, for $\log(F(t) = 0)$ as a function of the first Loschmidt Echo Crossing time $w_\times$. Operators were on sites 1 & 3.

and 3.2. A brief conceptual outline is provided in this section, with which to guide future analytical explorations that seek to tie when a system experiences its first DQPT and when the same system fully scrambles.

Based on persistence patterns in numerical results, we are motivated to investigate deeper connections between the Kirkwood-Dirac Quasiprobability (KDQ) which underlies the OTOC, as first demonstrated in Ref. [218, 219, 220, 221], and the Fisher-zero crossings which characterize a DQPT. Further analysis on the KDQ behavior will likely need to be undertaken as well as studies focusing on the collective behavior of the Fisher zero crossings for the families of Eq. (1.7) that were time evolved.

Since Eq. 1.7 is a spin system, it has a finite eigenbasis for $N < \infty$ which will be an important source of convenience later on. Within the OTOC, $F(t) = \langle\psi_i| W_t^\dagger V^\dagger W_t V |\psi_i\rangle = \langle\psi_i| e^{i\hat{\mathcal{H}}_S t} W e^{-i\hat{\mathcal{H}}_S t} V e^{i\hat{\mathcal{H}}t} W e^{-i\hat{\mathcal{H}}_S t} V |\psi_i\rangle$, we define our time evolution operator to be:

$$U = e^{i\mathcal{H}_S t} \,, \tag{3.1}$$

and our local operators of interest, V and W, are both the single-site spin-Z operator.

Both are always acting on different sites within the spin chain. Also, we take $\hbar = 1$. The eigendecomposition of V and W can be written as $V = \sum_{v_\ell, \alpha_{v_\ell}} v_\ell |v_\ell, \alpha_{v_\ell}\rangle\langle w_\ell, \alpha_{v_\ell}|$ and $W = \sum_{w_\ell, \beta_{w_\ell}} w_\ell |w_\ell, \beta_{w_\ell}\rangle\langle w_\ell, \beta_{w_\ell}|$. Eigenvalues are w_ℓ and v_ℓ and eigenvectors β_{w_ℓ} and α_{v_ℓ}.

Note that a Kirkwood-Dirac quasiprobability (KDQ) amplitude ($\tilde{A}_\rho$) based argument was first defined in Ref. [220] for a state $\rho = \sum_j p_j |j\rangle \langle j|$, where p_j is the probability of occurrence for a particular state $|j\rangle$. A_ρ results from some protocol $\mathbb{M}_{\mathcal{P}_{1,2}}$ devised to measure observables $j, (v_1, \alpha_{v_1}), (w_1, \beta_{w_1})$for an all-to-all connected two-level Heisenberg spin-chain. The measurement protocol $\mathbb{M}_{\mathcal{P}_{1,2}}$, and $\mathbb{M}_{\mathcal{P}_{3,2}}$ is run, and results in $\tilde{A}_\rho$ to generate observables w_2, w_3, v_1, and v_2.

Tuples of $(v_\ell, \alpha_{v_\ell})$ and (w_ℓ, β_{w_ℓ}) can then be obtained, and Ref. [220] has shown that complex conjugating them and multiplying them by $\tilde{A}_\rho$ can recover $F(t)$. What one would want to do is to derive a relation between these values, $(v_\ell, \alpha_{v_\ell})$ and (w_ℓ, β_{w_ℓ}), and the real axis crossings in the complex plane of complex partition functions[167, 169, 166], also called fisher zero crossings.

Generally complex parameters are not particularly physically relevant, but complex-

conjugating partition functions is an old tool in history of probing phase transitions [222]. The work conducted in this section pursues establishing a connection between the operators chosen for the OTOC, as well as the initial states chosen to measure the DQPT from. The initial state chosen impact the rate function $\lambda_s(z) = 2Re[gs(z)]$, where $g_s(z) = -\frac{1}{N}\sum_j \log\left[z_j - z\right]$ and the z_j are the fisher zero crossings.

In an attempt to highlight a potential link between $(v_\ell, \alpha_{v_\ell})$ and (w_ℓ, β_{w_ℓ}) to z_j, complex conjugation of the Loschmidt echo is considered next. DQPTs are defined as non-analytic kinks in the rate function:

$$\lambda(t) = \min(\frac{1}{N}\log\mathcal{L}_{\Psi_1}(t), \frac{1}{N}\log\mathcal{L}_{\Psi_2}(t)) \tag{3.2}$$

.

Note that $\mathcal{L}_{\Psi_1}(t) = |\langle\Psi_1(0)|U|\Psi_1(0)\rangle|^2$ and $\mathcal{L}_{\Psi_2}(t) = |\langle\Psi_1(0)|U|\Psi_2(0)\rangle|^2$. Ψ_1, Ψ_2 are defined as Eq. 2.3.

It is possible to complex conjugate the Loschmidt amplitude by extending the time variable into the complex plane:

$$t \to z = t + it_\tau$$

where t_τ is the imaginary time. The complex plane echo is now:

$$\mathcal{G} = \langle\Psi_1(0)|e^{i\mathcal{H}_s z}|\Psi_1(0)\rangle \ . \tag{3.3}$$

Because the eigenbasis for the $\mathcal{H}_S$ is finite, Eq. 3.3 can be written as a finite sum:

$$\mathcal{G}(z) = e^{\mu(z)}\Pi_j[z_j - z] \ . \tag{3.4}$$

where $\mu(z)$ is can be taken as some analytic function (which we can define later if needed) and z_j are zeros of Eq. 3.4 in $\mathbb{C}$. All information critical to the definition of Loschmidt echo-defined DQPTs are contained within these zeros of the complex plane.

Each complex contribution to the complex Loschmidt amplitude is:

$$g(z) = \frac{1}{N}\sum_j \log[z_j - z] \ . \tag{3.5}$$

At the time of this writing, two methods to fully bridge $(v_\ell, \alpha_{v_\ell})$ and (w_ℓ, β_{w_ℓ}) with Eq. (2.23) appear to be promising routes to pursue. The first involves directly linking z_j to the complex eigenvalues in $v_1 w_2 v_2^* w_3^*$ and appears to not have been probed in current literature. Numerical investigations verifying the viability of this path would lend credence to a potential link. Another potential approach to bridge a connection between the two distinct values is to extend the OTOC definition into the complex plane by extending the time evolution operators that define the Loschmidt echos constituting the OTOC. Afterwards, one could try to recreate a close variant of $(v_\ell, \alpha_{v_\ell})$ and (w_ℓ, β_{w_ℓ}) in complex space.

The complex plane time evolution operator can be defined as:

$$U_{\mathbb{C}} = e^{i\mathcal{H}_S z} = e^{i\mathcal{H}_S(t+i\tau_t)} \,, \tag{3.6}$$

which should be noted, is no longer unitary after transforming to the $\mathbb{C}$ plane.

The second approach involves rewriting the OTOC in terms of these non-unitary complex time evolution operators:

$$F_{\mathbb{C}}(t) \to \langle \psi_i | \, e^{i\mathcal{H}_S(t+i\tau_t)} W e^{i\mathcal{H}_S(t+i\tau_t)} V e^{i\mathcal{H}_S(t+i\tau_t)} W e^{i\mathcal{H}_S(t+i\tau_t)} V \, | \psi_i \rangle \tag{3.7}$$

Again, numerically searching for singularities in the complex plane for Eq. (3.7) would be the natural first step, and from Eq. (3.7), constructing an inequality bound on Eq. (3.1), rather than attempting to recover Eq. (3.1) entirely, could be a reasonable subsequent step, preceding Eq. (3.1)'s recovery.

Chapter 4

QUANTUM SIMULATIONS OF THREE-FLAVORED NEUTRINO SYSTEMS

The work presented in this chapter is based on work done in collaboration with Francesco Turro, Ivan Chernyshev and Marc Illa [223].

4.1 Introduction

The use of qudits [224] for simulating nuclear and high-energy physics systems has generated significant interest [225, 226, 227, 228, 229, 230, 231, 232, 233, 234, 235, 236, 237, 238, 239], as a result of recent advancements in experimental realizations of qudit-based platforms, including trapped-ion systems [240, 241, 242, 243, 244], superconducting circuits [245, 246, 247, 248], superconducting radio-frequency cavities [249], and photonic systems [250]. Multilevel quantum devices can efficiently map to high-dimensional systems, which is advantageous for the quantum simulation of such systems, as well as quantum algorithm performance [251, 252, 253, 254, 255] (see Ref. [256] for a review). Three-level quantum systems (qutrits) [245, 257, 258, 259, 241, 260, 261, 262, 244] are particularly attractive for simulating three-flavor neutrino systems.

In extreme astrophysical environments, neutrinos can reach high enough densities such that their flavor evolution can affect large scale dynamics. Examples include: CCSNe processes [263, 264, 265, 266, 267], flavor transport in remnants of binary star mergers [268, 269, 270, 271, 272, 273, 274, 275], and nucleosynthesis [276, 277, 278, 279, 280] (see Refs. [281, 282, 41, 283, 284, 285, 286, 287, 288] for reviews on these topics).

At distance $\lesssim$ 100 km away from the CCSNe center, self-interacting neutrino-neutrino currents [289, 290, 291, 292, 293] predominate the region's dynamics, while at distance $\gtrsim$ 100 km, neutrino-vacuum oscillations and the Mikeheyev-Smirnov-Wolfenstein (MSW) effect [294, 295, 296, 297] become the primary mechanisms driving neutrino flavor evolution. The Hamiltonian describing the flavor dynamics of neutrinos propagating through a CCSN

environment therefore contains three terms: the one-body vacuum oscillation term, the one-body background matter interaction term modeled by the MSW effect, and the two-body neutrino-neutrino self-interaction term describing the coherent forward scattering [298, 299, 300, 263, 264, 301, 302, 303, 304, 305, 306, 307] that gives rise to the quantum phenomenon of coherent collective flavor oscillations.

While mean-field studies have evidenced collective flavor dynamics [265, 308, 309, 310, 311, 312, 313, 314], there is growing interest in collective dynamics beyond the mean-field approximation, such as when nontrivial neutrino-neutrino two-body correlations are taken into account [315, 316, 317, 132, 318]. The all-to-all connectivity of the two-body operator requires exponentially-growing classical resources when attempting to simulate neutrino dynamics from the exact many-body Hamiltonian at physically relevant scales, mainly due to the rapid entanglement growth in such systems.[1]

Recent progress in quantum simulations of two flavor neutrino systems [319, 320, 321, 322, 323, 324] has demonstrated quantum devices' potential [325] to efficiently capture the non-trivial entanglement structure present in many-body neutrino systems. Classical and quantum simulations of relatively small-sized two-flavor neutrino systems have uncovered a variety of uniquely quantum phenomena [326, 327, 328, 315, 316, 323, 132, 39, 329], further motivating quantum simulations of three-flavor self-interacting neutrino systems [330, 331].

In this work, we introduce qubit and qutrit-based quantum circuits for simulating the time evolution of the three-flavor neutrino system. Simulation of the system dynamics for $N = 2, 4$ and 8 neutrinos is demonstrated on the IBM `ibm_torino` [332] and Quantinuum `H1-1` qubit platforms [3] and time evolved observables, such as single-neutrino flavor probabilities and entanglement entropy, are studied.

4.2 Hamiltonian

Within 100 km from the CCSN core, contributions from background matter (MSW effect) can be assumed negligible as similarly approximated in Refs. [333, 327, 328, 315, 334]), and antineutrinos are not considered in this work. The Hamiltonian governing the evolution of

[1] See Refs. [157, 158] for discussions regarding the apparent differences between the mean-field and many-body approaches.

the neutrino system studied is then

$$H = H_\nu + H_{\nu\nu} \ , \tag{4.1}$$

where H_ν describes the one-body neutrino Hamiltonian given by the vacuum oscillation and $H_{\nu\nu}$ the neutrino-neutrino interactions resulting from coherent forward scattering.

The vacuum oscillations can be described in the mass basis as [304]

$$H_\nu = \sum_i^N H_\nu^{(i)} = \sum_i^N -\frac{\omega}{2}\lambda_3^{(i)} + \frac{\omega - 2\Omega}{2\sqrt{3}}\lambda_8^{(i)} \ , \tag{4.2}$$

where the index i sums over N neutrinos in the system, $\lambda_n^{(i)}$ is the n^{th} Gell-Mann matrix acting on the i^{th} neutrino (the Gell-Mann matrices are detailed in App. H), and ω and Ω are the oscillation frequencies, defined as

$$\omega = \frac{1}{2E}\Delta m_{21}^2 \ , \quad \Omega = \frac{1}{2E}\Delta m_{31}^2 = \omega\frac{\Delta m_{31}^2}{\Delta m_{21}^2} \ , \tag{4.3}$$

with $\Delta m_{ij}^2 = m_i^2 - m_j^2$, and m_i^2 being the squared mass of the i^{th} mass-eigenstate neutrino, with the neutrinos taken to have the same energy. The i^{th} one-body Hamiltonian can also be written as

$$H_\nu^{(i)} = \begin{pmatrix} 0 & 0 & 0 \\ 0 & \omega & 0 \\ 0 & 0 & \Omega \end{pmatrix} \ . \tag{4.4}$$

Here, identity contributions that correspond to global phases in the real-time evolution operator have been neglected.

To operate in the flavor basis, the Pontecorvo-Maki-Nakagawa-Sakata (PMNS) matrix is used to transform between mass and flavor basis,

$$\begin{pmatrix} \nu_e \\ \nu_\mu \\ \nu_\tau \end{pmatrix} = U_{\text{PMNS}} \begin{pmatrix} \nu_1 \\ \nu_2 \\ \nu_3 \end{pmatrix} , \tag{4.5}$$

$$U_{\text{PMNS}} = \begin{pmatrix} 1 & 0 & 0 \\ 0 & c_{23} & s_{23} \\ 0 & -s_{23} & c_{23} \end{pmatrix} \begin{pmatrix} c_{13} & 0 & s_{13}e^{-i\delta_{\text{CP}}} \\ 0 & 1 & 0 \\ -s_{13} & 0 & c_{13} \end{pmatrix} \begin{pmatrix} c_{12} & s_{12} & 0 \\ -s_{12} & c_{12} & 0 \\ 0 & 0 & 1 \end{pmatrix} , \tag{4.6}$$

PMNS parameters (deg.)	
θ_{12}	$33.67^{+0.74}_{-0.71}$
θ_{23}	$42.3^{+1.1}_{-0.9}$
θ_{13}	$8.58^{+0.11}_{-0.11}$
δ_{CP}	232^{+39}_{-25}
Mass parameters MeV^2	
Δm^2_{21} $(\times 10^{17})$	$7.41^{+0.21}_{-0.20}$
Δm^2_{31} $(\times 10^{15})$	$2.505^{+0.024}_{-0.026}$

Table 4.1: PNMS mixing parameters and mass differences taken from Refs. [1, 2], assuming normal ordering.

where $c_{ij} \equiv \cos(\theta_{ij})$ and $s_{ij} \equiv \sin(\theta_{ij})$, and the mixing angles θ_{ij} and phase δ_{CP} are taken from NuFIT v5.3 [1, 2] (with other groups recovering consistent results [335, 336]), and are tabulated in Table 4.1.

The three-flavor coherent neutrino-neutrino interaction can be described by the following Hamiltonian [304],

$$H_{\nu\nu} = \sum_{i<j} J_{ij} \boldsymbol{\lambda}^{(i)} \cdot \boldsymbol{\lambda}^{(j)} \ , \tag{4.7}$$

with $\boldsymbol{\lambda}^{(i)} = (\lambda_1^{(i)}, \lambda_2^{(i)}, \ldots, \lambda_8^{(i)})$, and the coupling coefficient J_{ij} is defined as

$$J_{ij} = \frac{G_F \rho_\nu}{\sqrt{2}N}(1 - \cos\theta_{ij}) \ , \tag{4.8}$$

with G_F being Fermi's constant and ρ_ν the number-density of neutrinos. The angle θ_{ij} is the angle between the momentum of the i^{th} and j^{th} neutrino, and for demonstration purposes, we use the simple model introduced in Ref. [319], where it is sampled from a cone-shaped

distribution, $\theta_{ij} = \frac{|i-j|}{N-1}\arccos(0.9)$, as done in Refs. [319, 321, 322, 323, 331]. The neutrino density coupling constant μ is defined such that the one-body and two-body terms have the same magnitude,

$$\mu = \frac{G_F \rho_\nu}{\sqrt{2}} = \frac{\Delta m^2_{31} N}{2E}\,, \tag{4.9}$$

and it is assumed time independent. However, since the density of neutrinos decreases as a function of time, a realistic simulation should consider a time-dependent strength of the two-body term (see, e.g., Refs. [334, 330, 324]).

The final Hamiltonian in the mass basis as a function of μ is then given by

$$\begin{aligned} H = \frac{\mu}{N}\sum_i \left[-\frac{\omega}{2\Omega}\lambda_3^{(i)} + \frac{\omega - 2\Omega}{2\sqrt{3}\Omega}\lambda_8^{(i)}\right] \\ + \frac{\mu}{N}\sum_{i<j}[1-\cos(\theta_{ij})]\boldsymbol{\lambda}^{(i)}\cdot\boldsymbol{\lambda}^{(j)}\,. \end{aligned} \tag{4.10}$$

While the two-body term is basis-independent, to transform the one-body term into flavor space the PNMS matrix is applied to the one-body term (Eq. (4.2)) as follows

$$H_\nu^{(i)}|_{\text{flavor}} = U_{\text{PNMS}} \cdot H_\nu^{(i)} \cdot U_{\text{PNMS}}^\dagger\,. \tag{4.11}$$

4.3 Qutrit mapping

Motivated by neutrinos' natural three-level structure, we present qutrit-based quantum circuits that can be used for simulating the time evolution of a many-body three-flavored neutrino system. The proposed qutrit circuit follows the native qutrit gate set and the notation of the transmon qudits in Ref. [261] (see App. I for more details).

The one-body term H_v, first implemented in Ref. [337] on an IBM quantum computer, only involves single-qutrit gates. Equation (4.4) can be implemented with a single phase gate,

$$e^{-itH_\nu^{(i)}} = \text{Ph}(0, -\omega\,t, -\Omega\,t) = \text{diag}(1, e^{-i\omega\,t}, e^{-\Omega\,t})\,, \tag{4.12}$$

and the PNMS matrix can be decomposed as

$$\begin{aligned} U_{\text{PNMS}} \;&= R_y^{12}(\theta_{23}) R_Z^{02}\left(\frac{-\pi+\delta_{CP}}{2}\right) R_y^{02}(\theta_{13}) \\ &\times R_Z^{02}\left(-\frac{-\pi+\delta_{CP}}{2}\right) R_y^{01}(\theta_{12})\,, \end{aligned} \tag{4.13}$$

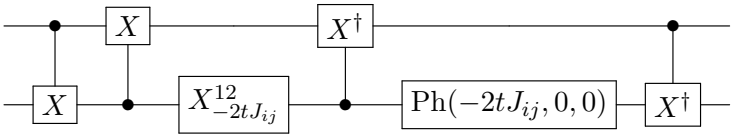

Figure 4.1: Quantum circuit implementing the term $e^{-itJ_{ij}\boldsymbol{\lambda}^{(i)}\cdot\boldsymbol{\lambda}^{(j)}}$ from the two-neutrino part $H_{\nu\nu}$. Definitions of the gates can be found in App. I.

where App. I shows our gate definitions.

For the two-body term, while a numerical compilation requires at most 6 CX (or $CX^\dagger$) gates [261], two controlled-shift gates CX and two $CX^\dagger$ were found to be sufficient to apply the specific SU(9) rotation described in Eq. (4.7), as shown in Fig. 4.1. The qutrit CX gate is defined as $CX\,|x,y\rangle = |x, \mathrm{mod}(\mathrm{x}+\mathrm{y},3)\rangle$, and the $X^{12}_{2tJ_{ij}}$ gate is given by

$$X^{12}_{-2tJ_{ij}} = \begin{pmatrix} 1 & 0 & 0 \\ 0 & \cos(J_{ij}\,t) & -i\sin(J_{ij}\,t) \\ 0 & -i\sin(J_{ij}\,t) & \cos(J_{ij}\,t) \end{pmatrix} . \tag{4.14}$$

4.3.1 Swap network

Since strategic ordering of application of Eq. (4.7) is required to minmize circuit depth, we implement the swap network, $\mathbb{SW}$, which was first proposed in Ref. [319] and is similar to the fermionic swap from Refs. [338, 339]. This network limits the depth to N layers of Eq. (4.7) for a system with N neutrinos (assuming the qubits are in a linear network and gates can be applied in parallel). In the original $\mathbb{SW}$, SWAP gates are needed between each layer to achieve the all-to-all connectivity. However, for this particular implementation, they can be absorbed into the two-body term,

$$\begin{aligned} \mathrm{SWAP}_{ij}\cdot e^{-itJ_{ij}\boldsymbol{\lambda}^{(i)}\cdot\boldsymbol{\lambda}^{(j)}} &= e^{-i\frac{\pi}{4}\boldsymbol{\lambda}^{(i)}\cdot\boldsymbol{\lambda}^{(j)}}\cdot e^{-itJ_{ij}\boldsymbol{\lambda}^{(i)}\cdot\boldsymbol{\lambda}^{(j)}} \\ &= e^{-i(tJ_{ij}+\frac{\pi}{4})\boldsymbol{\lambda}^{(i)}\cdot\boldsymbol{\lambda}^{(j)}} , \end{aligned} \tag{4.15}$$

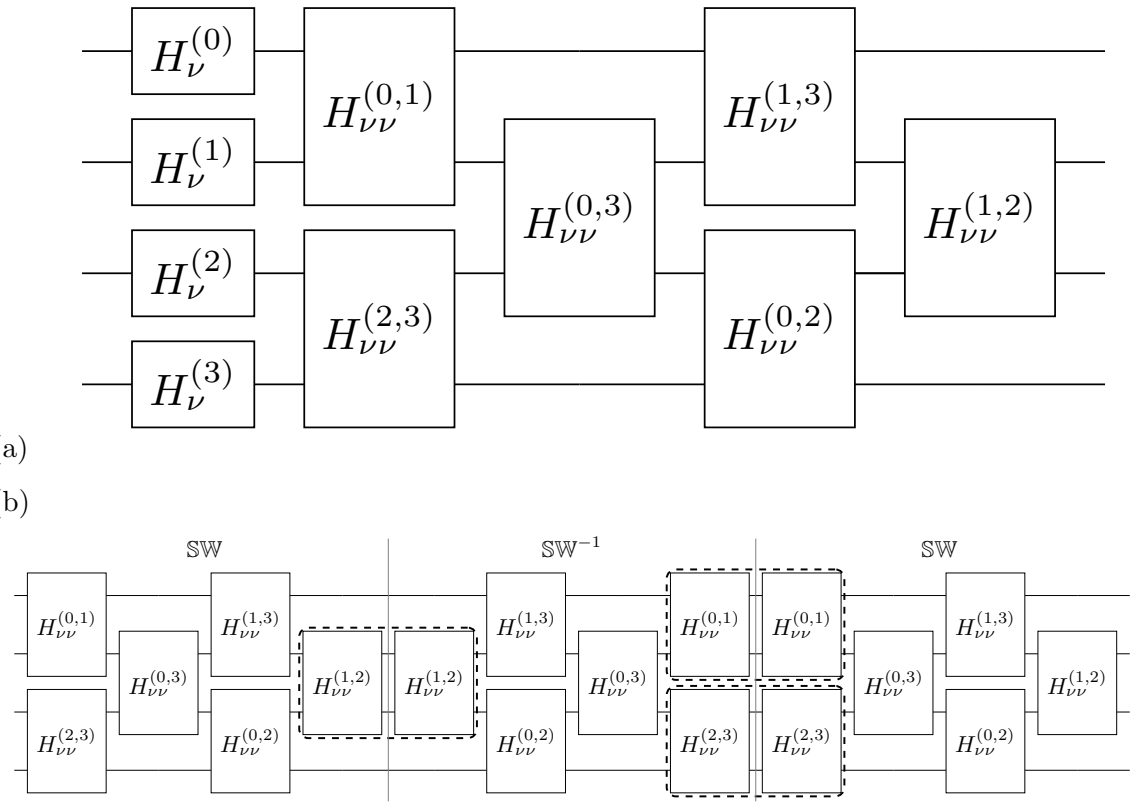

Figure 4.2: (a) Quantum circuit implementing a single LO Trotterized time evolution step via the swap network for four neutrinos. (b) Simplification when using three steps of the NLO* Trotterized time evolution operator for four neutrinos, where the highlighted operations can be simplified by a single two-qubit box with twice the time step.

substantially reducing the number of entangling gates, particularly in hardware with limited connectivity such as superconducting systems.[2] The schematic of such a network can be seen in Fig. 4.2a for four neutrinos. While SWAP gates might not be required in devices with all-to-all connectivity (such as trapped ions), this new strategy

can also improve the circuit fidelity in devices where qubits have to be physically moved around, such as in the Quantinuum devices.

[2]The same simplification can be applied on the two-flavor case, where the SWAP gate can be written as $e^{-i\frac{\pi}{4}\boldsymbol{\sigma}^{(i)}\cdot\boldsymbol{\sigma}^{(j)}}$.

The one- and two-body terms in Eqs. (4.2) and (4.7) commute, $[H_\nu, H_{\nu\nu}] = 0$, so they can be Trotterized independently. The leading-order (LO) Trotterized time evolution operator is therefore

$$U(t)_{\mathrm{LO}} = e^{-itH_\nu} \prod_{i,j \in \mathbb{SW}} e^{-itJ_{ij}\boldsymbol{\lambda}^{(i)}\cdot\boldsymbol{\lambda}^{(j)}} \ . \tag{4.16}$$

When applying multiple Trotter steps, it is more efficient to use the second order (NLO) Suzuki-Trotter formula [340, 341], as used in Ref. [322],

$$\begin{aligned} U(t)_{\mathrm{NLO}} \ &= e^{-itH_\nu} \prod_{i,j \in \mathbb{SW}} e^{-i\frac{t}{2}J_{ij}\boldsymbol{\lambda}^{(i)}\cdot\boldsymbol{\lambda}^{(j)}} \\ &\times \prod_{i,j \in \mathbb{SW}^{-1}} e^{-i\frac{t}{2}J_{ij}\boldsymbol{\lambda}^{(i)}\cdot\boldsymbol{\lambda}^{(j)}} \ , \end{aligned} \tag{4.17}$$

with $\mathbb{SW}^{-1}$ applying the gates in reverse order. With this method, additional simplifications are possible. In particular, the last and first layer in $\mathbb{SW}$ and $\mathbb{SW}^{-1}$, respectively, can be merged into a single operation with twice the time step, as depicted in Fig. 4.2b.

This can be generalized to multiple Trotter steps by interleaving layers ordered in the $\mathbb{SW}$ and $\mathbb{SW}^{-1}$ network sequences, allowing for cancellations between these layers (referred as NLO*).[3] Then, the total number of CX gates for k number of Trotter steps (with $k \geq 2$) is

$$\left[U(\tfrac{t}{k})_{\mathrm{LO}}\right]^k \ : \ N_{CX} k \frac{N(N-1)}{2} \ , \tag{4.18}$$

$$\begin{aligned} U(t)_{\mathrm{NLO}^*_k} \ : \ & N_{CX} k \frac{N(N-1)}{2} - N_{CX} \left\lfloor \frac{k}{2} \right\rfloor \left(\left\lceil \frac{N}{2} \right\rceil - 1 \right) \\ & - N_{CX} \left\lfloor \frac{k-1}{2} \right\rfloor \cdot \left\lfloor \frac{N}{2} \right\rfloor \ , \end{aligned} \tag{4.19}$$

where $\lceil\cdot\rceil$ ($\lfloor\cdot\rfloor$) is the ceiling (floor) function, N is the number of neutrinos, and N_{CX} is the number of CX gates needed to compile a single neutrino-neutrino term (for the case in Fig. 4.1, $N_{CX} = 4$). A reduction in two-qubit gates is seen when using NLO* compared to LO with increasing number of Trotter steps, as well as improved convergence.

[3] This can be extended to higher-order Suzuki-Trotter formulas, although further simplifications are not expected to compensate for the increase in circuit depth.

4.4 Qubit mapping

In the absence of qutrit-based platforms, an alternate approach involves mapping a three-flavor neutrino to two qubits [342] , with each flavor encoded as: $|\nu_e\rangle \rightleftharpoons |00\rangle$, $|\nu_\mu\rangle \rightleftharpoons |01\rangle$, $|\nu_\tau\rangle \rightleftharpoons |10\rangle$, and the unassigned state $|11\rangle$ designated as the unphysical state (assuming no sterile neutrinos). Therefore, no matrix elements in the unitaries that implement the one- and two-neutrino terms are allowed to mix states between the physical and the unphysical sub-spaces. However, there is freedom to allow arbitrary mixing between unphysical states if the resulting quantum circuits are shallower.

For the one-neutrino term H_v, its time evolution operator in the mass basis is diagonal, and can be implemented with single-qubit R_z gates,

$$e^{-itH_v^{(i)}} = R_z(-\omega t)_{2i} \otimes R_z(-\Omega t)_{2i+1} \ . \tag{4.20}$$

In the flavor basis, the 3×3 matrix can be embedded into a 4×4 one, and the resulting SU(4) matrix can be transpiled into the three-CNOT circuits from Refs. [343, 344, 345] (or use the circuits from Refs. [342, 346]).

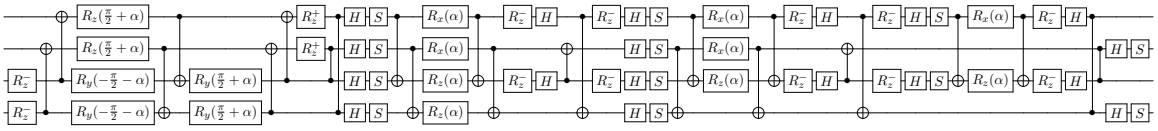

Figure 4.3: Circuit A implementing $e^{-i\alpha \boldsymbol{\lambda}^{(i)} \cdot \boldsymbol{\lambda}^{(j)}}$ in the physical subspace, using 24 CNOTs. The gates $R_z^{\pm}$ represents the short-hand version of $R_z(\pm\frac{\pi}{2})$.

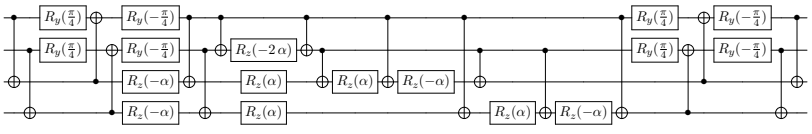

Figure 4.4: Circuit B implementing $e^{-i\alpha \boldsymbol{\lambda}^{(i)} \cdot \boldsymbol{\lambda}^{(j)}}$ in the physical subspace, using 18 CNOTs.

The two-neutrino term $H_{\nu\nu}$ is more delicate in this case, compared to the qutrit implementation. As mentioned, while the physical subspace is fixed, it is possible to implement

any rotation on the unphysical subspace, as long as the two subspaces do not get mixed. Here two circuits are presented, A (shown in Fig. 4.3) and B (shown in Fig. 4.4), both using qiskit conventions [347] for the gate definitions. The difference between these two circuits can be seen by looking at the unitary they implement,

$$e^{-i\alpha\boldsymbol{\lambda}^{(i)}.\boldsymbol{\lambda}^{(j)}}\Big|_A = \quad , \tag{4.21}$$

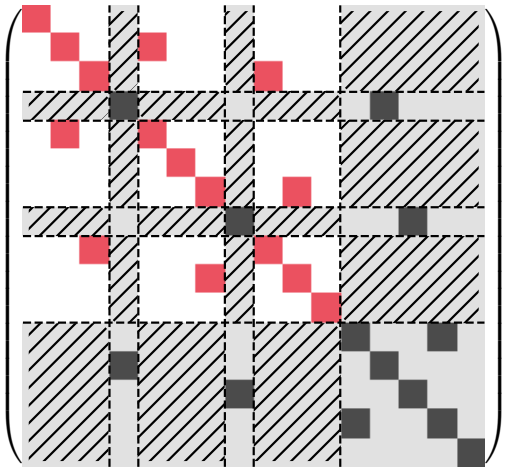

$$e^{-i\alpha\boldsymbol{\lambda}^{(i)}.\boldsymbol{\lambda}^{(j)}}\Big|_B = \quad . \tag{4.22}$$

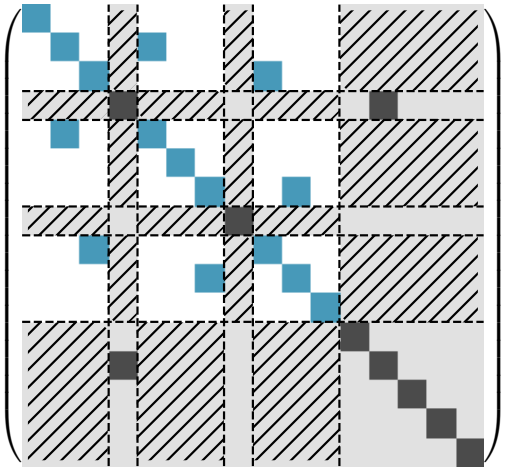

While both circuits have the same effect in the physical subspace, shown with white background in Eqs. (4.21)-(4.22), the rotations in the unphysical subspace, shown with a gray background, are different (with the dashed region being the transition between the two subspaces). For example, circuit A, in the full four-qubit space, implements the more general gate $e^{-i\alpha\tilde{\boldsymbol{\lambda}}^{(i)}.\tilde{\boldsymbol{\lambda}}^{(j)}}$ (with $\tilde{\boldsymbol{\lambda}}^{(i)}$ being the set of SU(4) generators that act on the i^{th} neutrino), which can also be written as $e^{-i\frac{\alpha}{2}\sum_{a,b}(\sigma_a\otimes\sigma_b)^i\otimes(\sigma_a\otimes\sigma_b)^j}$ (with σ_a being all possible elements of the Pauli group and the superscripts denoting neutrino-indices). While circuit A does not perform the most general SU(16) gate, it contains significantly less CNOT gates than what

one would obtain for an SU(16) gate using currently available operator-to-circuit transpilers such as qiskit [347, 348], tket [349], or other decomposition approaches [350, 351, 352, 353], which result in circuits containing on the order of $\mathcal{O}(100)$ CNOTs.

In both circuits A and B, the method discussed in Sec. 4.3.1 can absorb the SWAP operation into the two-body term, modifying $\alpha \to \alpha + \frac{\pi}{4}$. For this case, where each neutrino is composed of two qubits, the action of the SWAP gate is $\text{SWAP}_{ij} \left|ab\right\rangle_i \otimes \left|cd\right\rangle_j = \left|cd\right\rangle_i \otimes \left|ab\right\rangle_j$. Table 4.2 reports the number of required CX or CNOT gates and its corresponding depth for each quantum circuit (both qubit and qutrit) after compilation in both an-all-to-all and linear-chain architecture.

Qudit	Circuit	All-to-all		Linear chain	
		2-q gate count	2-q gate depth	2-q gate count	2-q gate depth
Qutrit	Fig. 4.1	4	4	4	4
Qubit	A (Fig. 4.3)	24	13	42	31
	B (Fig. 4.4)	18	12	30	25

Table 4.2: The two-qudit entangling gate count and depth for the two-neutrino quantum circuits proposed, involving two qutrits or four qubits.

4.5 Results

Dynamics for $N = \{2, 4, 8\}$ neutrinos were simulated with the `H1-1` Quantinuum trapped-ion and `ibm_torino` IBM superconducting quantum computers (device parameters can be found in App. M). The circuits described in Sec. 4.4 are used, in particular circuit B in Fig. 4.4, to implement the two-neutrino interaction. For two and four neutrinos, the time step was fixed (while increasing the number of Trotter steps), while for eight neutrinos number of Trotter steps was fixed (while increasing the time step).

For current noisy intermediate-scale quantum (NISQ) devices [354] error mitigation techniques are critical for reliable results. Well-known techniques, such as zero-noise extrapolation [355, 356, 357] and probabilistic error cancellation [356, 358], require a large overhead in

circuit sampling or an increase in circuit depth. For this study, the more resource-friendly algorithm decoherence renormalization (DR) as chosen, as first introduced in Refs. [359, 360], and later implemented in increasingly larger simulations in Refs. [361, 362, 363, 364, 365], to mitigate decoherent errors. For each time step, two different quantum circuits were ran: the first one (which we call the *physics* quantum circuit) implements the correct dynamics, and the second one (which we call the *identity* quantum circuit) runs a quantum circuit with the same structure as the *physics* circuit, except its action on the initial state is the identity. For first-order Trotter, this can be achieved by setting the time step to zero. For second-order Trotter, the sign in the time step for the second half of the circuit is flipped. Through the following rescaling formula, the experimental noiseless probability $P^{\text{ex}}_{phys}(t)$ can be computed as:

$$P^{\text{ex}}_{phys}(t) - d_n = \frac{P^{\text{ex}}_{id} - d_n}{P^{\text{noisy}}_{id} - d_n} \left(P^{\text{noisy}}_{phys}(t) - d_n \right) , \tag{4.23}$$

where $P^{\text{noisy}}_{phys}(t)$ indicates the obtained probability value from the *physics* quantum circuit and P^{noisy}_{id} indicates the obtained probability from the *identity* quantum circuit. P^{ex}_{id} corresponds to the noiseless result of the *identity* quantum circuit. d_n represents the decoherence value of the quantity computed P, which, for a generic n-neutrino measurement probability, is $d_n = 1/4^n$.

Equation (4.23) assumes all noise from the device is depolarizing. While this seems a reasonable assumption for the Quantinuum device, as observed in other trapped ion devices [366], the IBM quantum computer requires additional steps. To ensure all noise to be depolarizing, Pauli twirling [367, 368] was applied to transform coherent noise into incoherent noise, as well as dynamical decoupling [369, 370, 371] to suppress cross-talk and idling errors. Moreover, the matrix-free measurement mitigation (M3) [372] provided by the `Sampler` function from `qiskit` [347] was used to correct readout errors.

Two observables for each system were computed: the probability of a single neutrino in a particular flavor state P_ν and the persistence probability of the initial state, $|\langle\psi(0)|\psi(t)\rangle|^2$. Since device errors will populate the unphysical Hilbert space, we implement two different strategies for computing the single-neutrino probabilities. The first method uses the full physical Hilbert space (pHS) where all nonphysical states $|11\rangle$ are discarded. The second

method involves summing over the remaining states in the single-neutrino Hilbert space (snHS), mimicking a single measurement of the qubits representing the i^{th} neutrino. While unphysical states for other neutrinos contribute to the probability, after being corrected with DR their contribution can be small.[4]

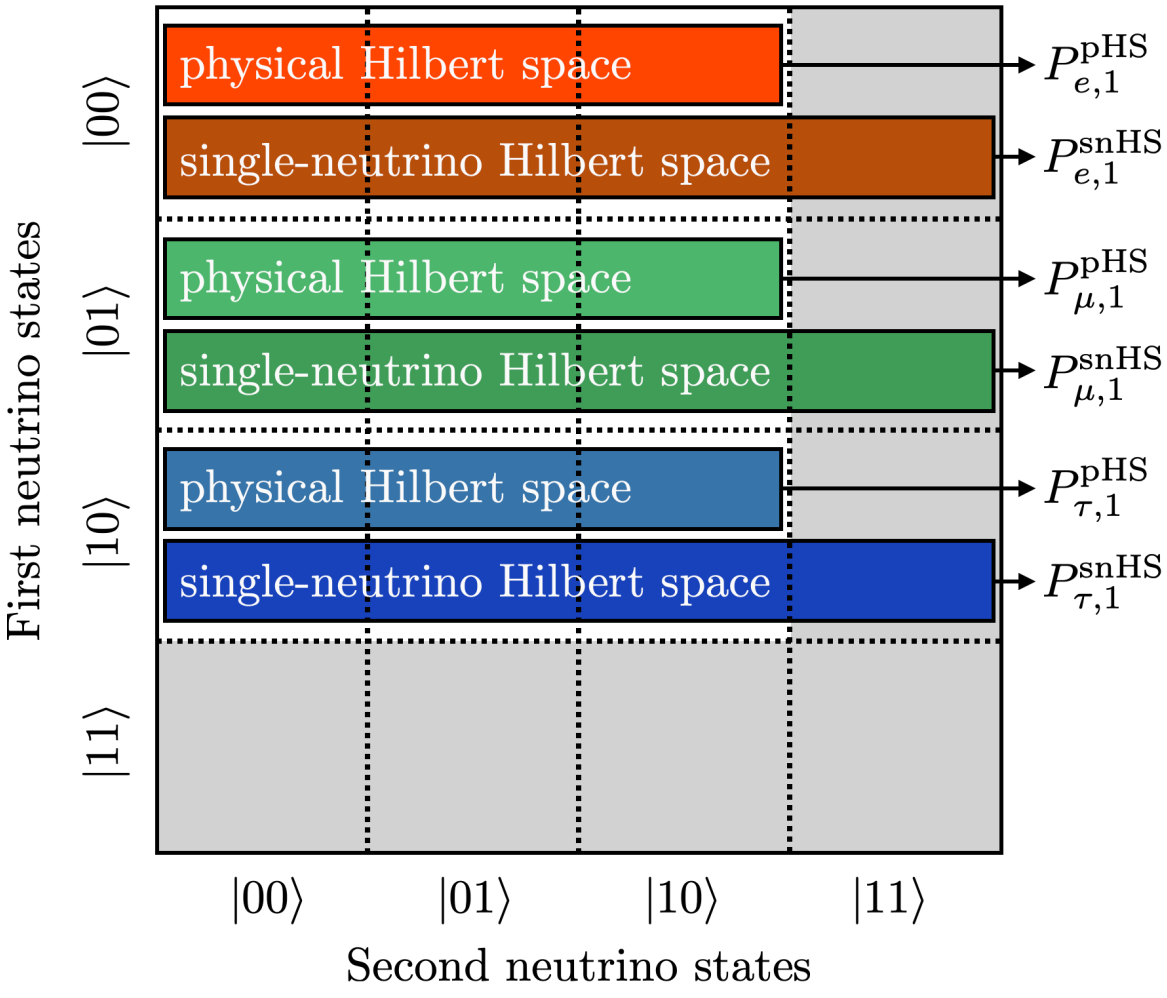

Figure 4.5: Different post-selecting procedures for computing the single-neutrino flavor probability, for a system of two neutrinos. The physical Hilbert space (pHS) approach only accounts for the physical flavor states; the single neutrino Hilbert space (snHS) approach keeps all contributions from the other neutrino states (both physical and unphysical).

[4]One should notice that the two methods have two different decoherence values in Eq. (4.23). When computing P_ν, $d_1^{\text{pHS}} = 3^{N-1}/4^N$ (with N the total number of neutrinos) and $d_1^{\text{snHS}} = 1/4$.

4.5.1 Quantinuum

The two methods are illustrated in Fig. 4.5 for the two neutrino case, where the big squares represent all possible 16 states.

Due to the all-to-all architecture of the Quantinuum device [3], the circuit in Fig. 4.4 for implementing the neutrino-neutrino term can be used without having to rewrite the CNOTs connecting distant qubits. After transpiling the circuit to the native gate-set (single-qubit gates and $\mathrm{ZZ}(\theta) = e^{-i(\theta/2)Z\otimes Z}$), the entangling gate count and depth gets reduced by one unit, compared to the numbers in Table 4.2.[5] A $\pi/4$ phase was added to the neutrino-neutrino terms to incorporate the SWAP gate into the latter. This is because although it is not necessary for this hardware, as mentioned in Sec. 4.3.1, it should reduce the shuffling of trapped ions.

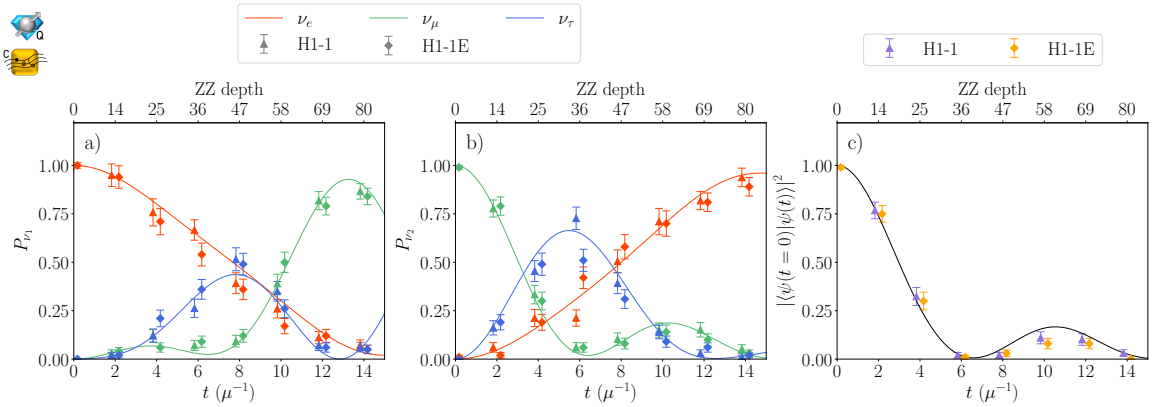

Figure 4.6: Flavor evolution of a two-neutrino system as a function of time. Panels (a) and (b) show the flavor evolution of the first and second neutrinos, respectively. Panel (c) shows the persistence probability of the initial state. Triangles and diamonds indicate results from the device (`H1-1`) and its emulator (`H1-1E`), respectively, slightly shifting the points for ease of readability; solid lines show the exact result. The top axis measures the ZZ depth for each point

First, the evolution of two neutrinos was simulated, using multiple numbers of Trotter time steps to study the propagation at long times and the noise sources for deep quantum

[5]The simplification occurs in the $R_z(-2\alpha)$ rotation and its two neighboring CNOTs in Fig. 4.4, which get transformed into a single $\mathrm{ZZ}(-2\alpha)$ gate.

circuits.[6] Figure 4.6 shows the results when we start from the $|\nu_e\nu_\mu\rangle$ state from the device `H1-1` and the emulator `H1-1E`, and use 100 shots per circuit. In this simulation, no error-mitigation techniques were implemented. Also, a 1-3% contribution from unphysical states was found, supporting the pHS approach to be a good approximation. The results, even for longer times, ($t = 14\mu^{-1}$), are compatible with the exact evolution (represented with solid lines). The icons in the top-left corner that appear in this and subsequent plots, identify if the noisy simulator (yellow icon) or quantum device (blue icon) was used [373].

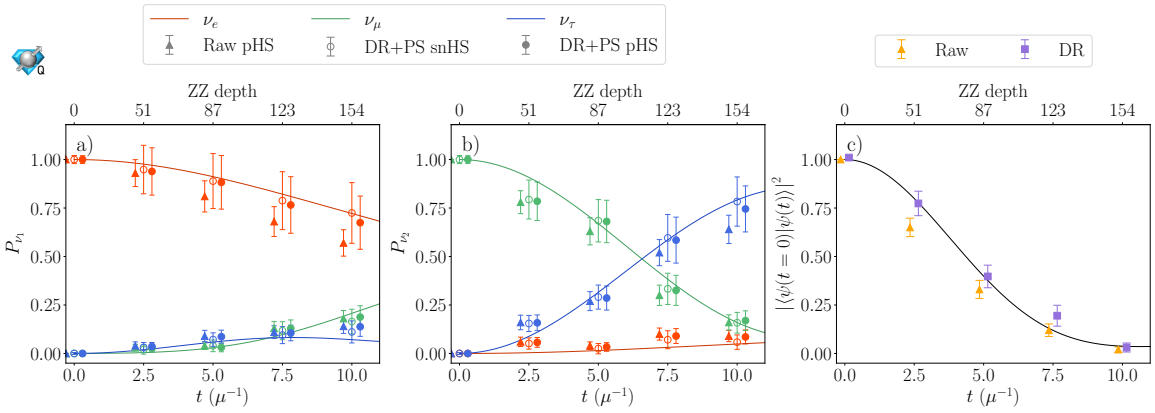

Figure 4.7: Flavor evolution of a four-neutrino system as a function of time, using the `H1-1` device. Panels (a) and (b) show the flavor evolution of the first and second neutrinos, respectively. Triangles indicate the raw pHS results. Empty and solid circles represent the results of applying DR, snHS, and pHS post-selecting procedures, respectively. Panel (c) shows the persistence probability of the initial state. The triangle and square markers represent the results without and with applying DR, respectively. In all panels, the solid lines show the exact evolution, and the points have been slightly shifted to ease the readability. The top axis measures the ZZ depth for each point.

The dynamics of four neutrinos starting from the $|\nu_e\nu_\mu\nu_e\nu_\tau\rangle$ state on the `H1-1` device was then simulated. Figure 4.7 shows the obtained results, using 100 shots per circuit. Like in Fig. 4.6, panels (a) and (b) illustrate the flavor evolution of the first (the neutrino starting as ν_e) and second neutrino (the neutrino starting as ν_μ), respectively. In this case DR was

[6] Notice that for two neutrinos, there are no Trotter errors in the decomposition of the time evolution circuits, therefore the multiple Trotter steps are a way to increase the circuit depth and benchmark the quantum computer.

used for error-mitigation, and after post-selection via snHS and pHS, the probabilities were normalized to sum to 1. Panel (c) shows the persistence probability of the initial state. For this larger system, an improvement after performing error mitigation was observed.

In App. J the emulator `H1-1E` and device `H1-1` results is compared. Generally the emulator and device results are observed to be compatible within reasonable uncertainties. Nevertheless, it was observed that the `H1-1E` emulator gives more pessimistic results than the actual machine.

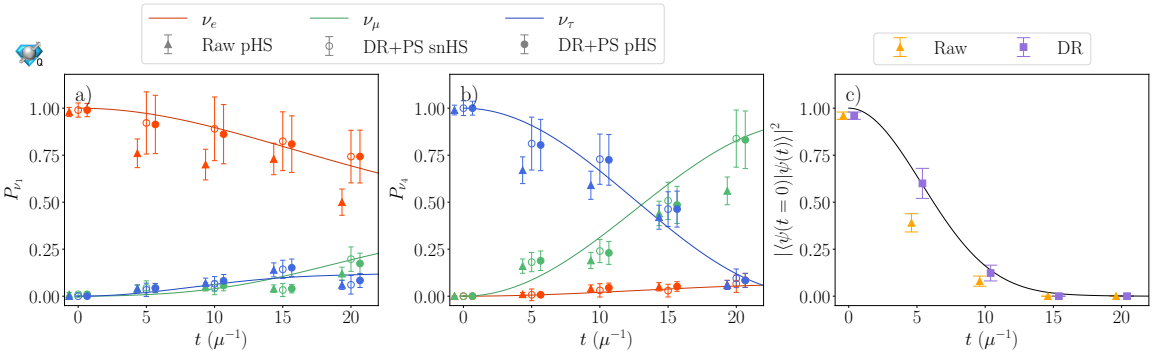

Figure 4.8: Flavor evolution for an eight-neutrino system as a function of time, using the `H1-1` device. Panels (a) and (b) show the flavor evolution of the first and fourth neutrinos, respectively. Panel (c) shows the persistence probability of the initial state. Details are as in Fig. 4.7.

Figure 4.8 shows the results for an eight-neutrino system, starting from $|\nu_e\nu_\mu\nu_e\nu_\tau\nu_e\nu_\mu\nu_e\nu_\tau\rangle$. In this case only a single Trotter time step was performed, increasing the time step. The implemented quantum circuits have a ZZ depth of 91, and 100 shots were used (except for $t = 10\mu^{-1}$, which used 79 shots). All results are compatible within 2σ with the exact evolution, albeit with larger uncertainties than the cases for two and four neutrinos.

4.5.2 IBM

Compared to Quantinuum, the IBM hardware has the constraint of linear connectivity between qubits (a one-dimensional chain was selected from the heavy-hex lattice), necessitating the circuit in Fig. 4.4 to be compiled into a linear chain architecture. All results

were obtained from implementations on `ibm_torino`, where the native entangling gate is the controlled-Z (CZ) gate, leading to the same depth and number of gates as in Table 4.2.

As discussed at the beginning of in Sec. 4.5, $10 \times N$ different Pauli-twirled quantum circuits were ran for each time step in order to average out the coherence noise (with N being the number of neutrinos), using 8000 shots per circuit. After applying DR and the post-selecting procedures it was noted that the resulting single-neutrino probabilities could become unphysical (either negative or greater than 1), an issue not encountered when using the Quantinuum device in Sec. 4.5.1. To fix this, the algorithm of Ref. [374] was applied to find the closest probability distribution. The uncertainties from combining the different twirled circuits were computed via bootstrap resampling.

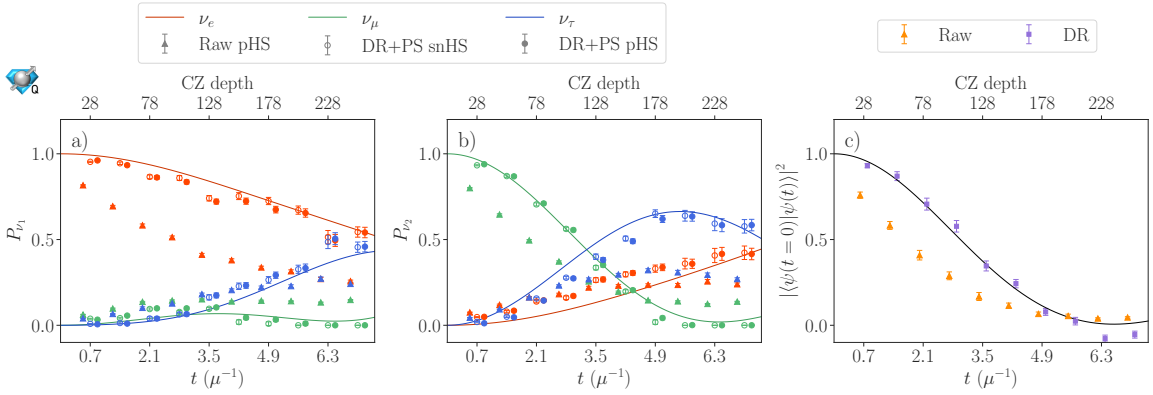

Figure 4.9: Flavor evolution for two neutrinos as a function of time obtained from `ibm_torino` device. Panels (a) and (b) show the flavor evolution of the first and second neutrinos, respectively. Panel (c) shows the persistence probability of the initial state. Details are as in Fig. 4.7. The top axis measures the CZ depth at every other point.

Figure 4.9 depicts the evolution for a two-neutrino system, starting from the $|\nu_e\nu_\mu\rangle$ state. Unlike for Quantinuum (Fig. 4.6), in this case error mitigation is essential for the results to be compatible with the exact evolution. While most points are within 1σ and 3σ, it seems that the initial state persistence is more robust against errors than the single-neutrino probabilities.

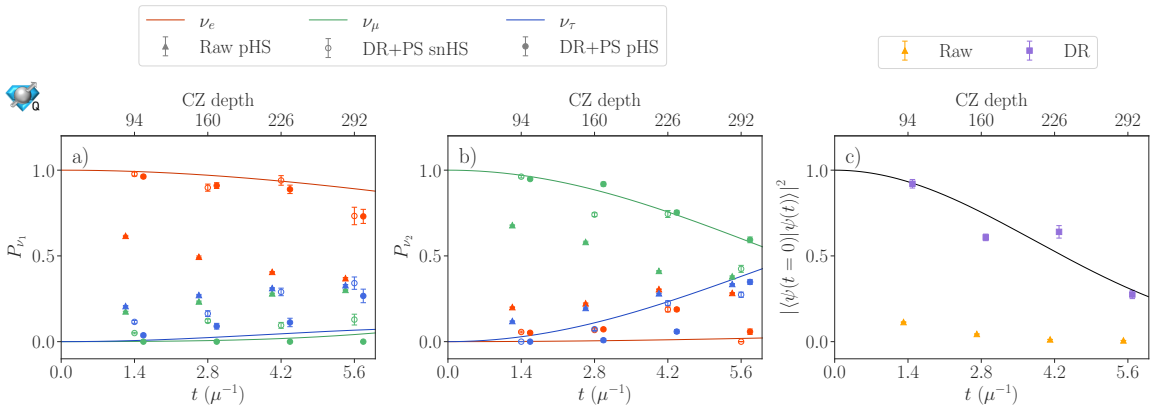

Figure 4.10: Flavor evolution for four neutrinos as a function of time obtained from the `ibm_torino` device. Panels (a) and (b) show the flavor evolution of the first and second neutrinos, respectively. Panel (c) shows the persistence probability of the initial state. Details are as in Fig. 4.7. The top axis measures the CZ depth at each point.

Figure 4.10 shows the evolution for the four-neutrino system, starting from the $|\nu_e\nu_\mu\nu_e\nu_\tau\rangle$ state. Like in the two-neutrino case, the obtained results follow the analytical evolution, although in some cases there is a difference of more than 5σ. This growing tension is investigated further in the eight-neutrino system.

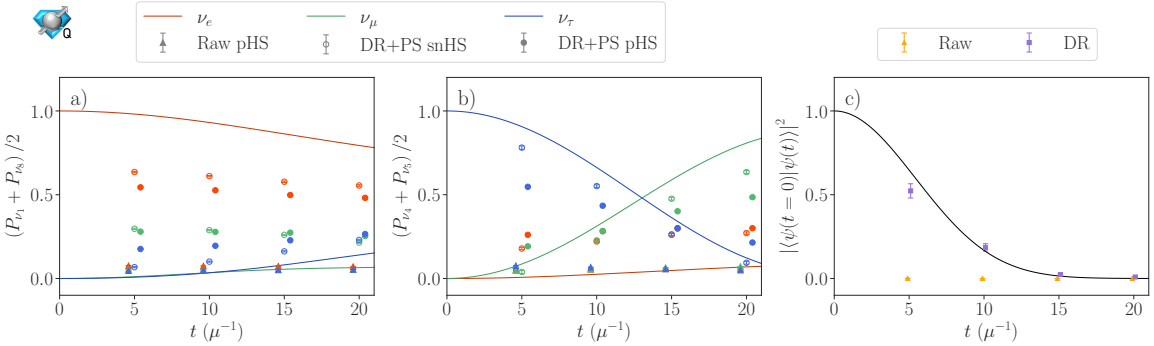

Figure 4.11: Flavor evolution for eight neutrinos as a function of time obtained from the `ibm_torino` device. Panels (a) and (b) show the flavor evolution of the (symmetrized) first and fourth neutrinos, respectively. Panel (c) shows the persistence probability of the initial state. Details are as in Fig. 4.7.

Figure 4.11 shows the evolution for the eight-neutrino system, with quantum circuits that have a CZ depth of 182. In contrast to the previous results, here the initial state was the symmetric state $|\nu_e\nu_\mu\nu_e\nu_\tau\nu_\tau\nu_e\nu_\mu\nu_e\rangle$. This change enables averaging of the single-neutrino probability between the i^{th} and $(N+1-i)^{\text{th}}$ neutrino, improving the quality of the obtained results (as seen by the degradation in the four neutrino system in Fig. 4.10).[7] After performing the symmetrization, the noise contributions can be averaged out and reduced (for the non-symmetric initial state, see App. K). Despite performing error mitigation, the results in Fig. 4.11 for the single-neutrino probabilities have large deviations from the expected values (more noticeable with pHS post-selection than with snHS). As before, the initial state persistence seems to be more effectively recovered after DR.

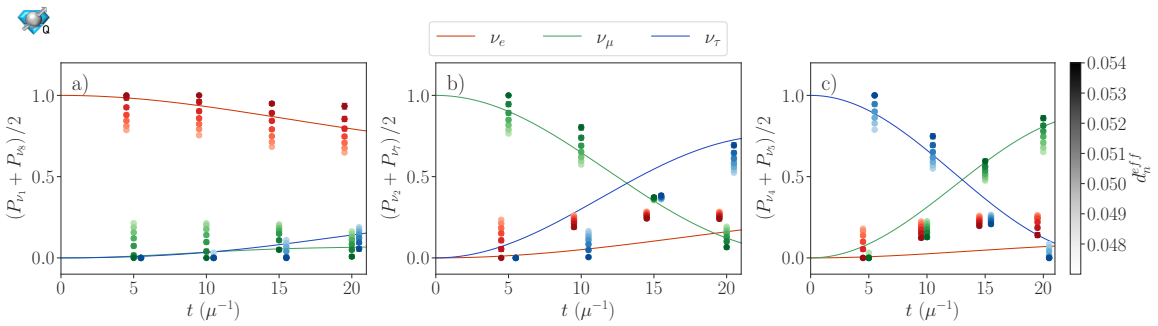

Figure 4.12: Flavor evolution for an eight-neutrino system as a function of time obtained from `ibm_torino` device as in Fig. 4.11, scanning over effective decoherence values $d_n^{(eff)}$ after applying DR and pHS post-selection procedure. Panels (a), (b), and (c) show the flavor evolution of the (symmetrized) first, second and fourth neutrinos, respectively. As shown in the color bar on the far-right, $d_n^{(eff)}$ increases from lighter to darker colors.

[7] A similar exchange symmetry has been observed for the two-flavor case [319, 322, 323], although in the three-flavor case it is only manifested for symmetric initial states.

Neutrino	P_e	P_μ	P_τ	$d_n^{(id)}$
$(P_1 + P_8)/2$	**0.079(4)**	0.054(3)	0.047(3)	0.033
$(P_2 + P_7)/2$	0.055(3)	**0.081(4)**	0.043(2)	0.033
$(P_3 + P_6)/2$	**0.081(4)**	0.052(3)	0.046(2)	0.033
$(P_4 + P_5)/2$	0.051(3)	0.043(2)	**0.085(4)**	0.033

Table 4.3: pHS probabilities obtained from implementing the *identity* quantum circuit on `ibm_torino` averaging the i^{th} and $(N+1-i)^{\text{th}}$ neutrinos. The last column shows the theoretical value for the decoherence line, $d_n^{(id)} = 3^7/4^8$. In the noiseless case, the probabilities in bold should be 1.

The single-flavor probability results obtained from running the *identity* quantum circuits in the DR method, shown in Table 4.3, suggest a shift of the decoherence value d_n in Eq. (4.23). After applying the identity operator, the decoherence line d_n is expected to be the plateau value of the probability that decays due to noise sources, i.e., the initial state probability value goes from 1 to d_n, while the other states' probabilities go from 0 to d_n. Therefore, in the ideal case, the state probability results never cross the decoherence line. Instead, Table 4.3 reports that all the obtained probabilities are greater than the theoretical decoherence value $d_n^{(id)}$ (given by $3^7/4^8$). A possible explanation is the simple depolarizing noise model, assumed when applying DR method, is not enough to describe the noise contributions, and different qubits are subjected to different noise sources. Moreover, a non-negligible contribution from relaxation process is observed, increasing the probability of being in the $|0\rangle$ state.

This implies that the decoherence value d_n in Eq. (4.23) should be empirically changed. Looking at the obtained values, the "effective" experimental decoherence value can be estimated to be in the range $d_n^{(eff)} \in [0.048, 0.054]$. If DR is applied using $d_n^{(eff)}$, the flavor probabilities for the first, second and fourth neutrino are closer to the analytical curves, as shown in Fig. 4.12. Also noted was that running a deeper quantum circuit for two Trotter steps causes the empirical decoherence line to move closer to the theoretical decoherence

line.

Entropy and tomography calculations

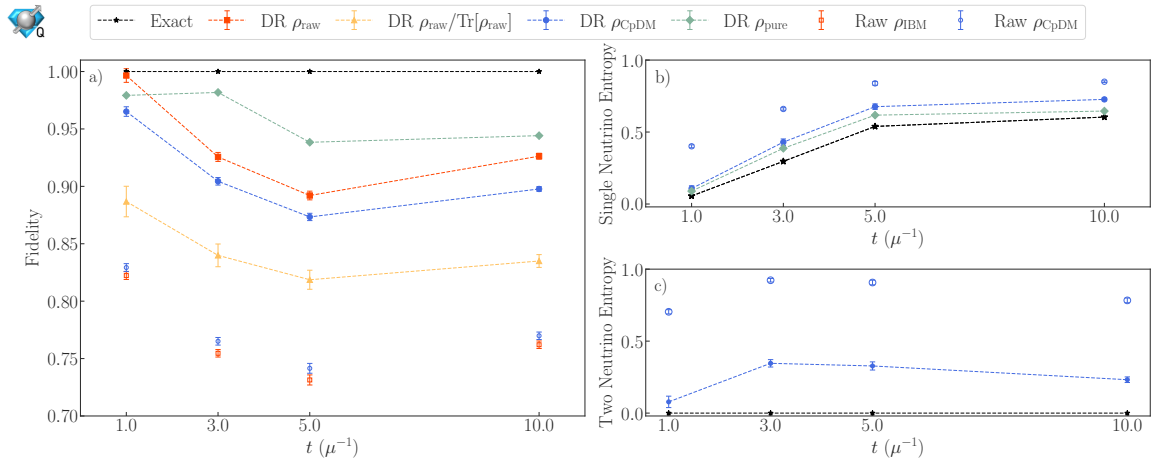

Figure 4.13: (a) Fidelity and (b) single-neutrino entropy for different Δt for the two neutrino system starting from $|e\mu\rangle$ state. The different points correspond to different methods in computing the density matrix (see the main text for details). (c) Two-neutrino entropy computed from $\rho_{\rm CDM}$ density matrix.

To compute the entanglement entropy and other entanglement witnesses, the density matrix of $n \leq N$ neutrinos is evaluated. One approach uses classical shadows [375]. Here, full state tomography is performed, as in Ref. [319]. Since not all 2^{2n} states are physical in the qubit mapping, the number of measurements needed to estimate the physical density matrix can be reduced. For example, for a single neutrino the state-tomography operator pool can be reduced from 15 to 7 (independent) different operators that describe the Gell-Mann decomposition in the qutrit physical space. The reduced density matrix for one neutrino is given by

$$\rho_\nu = \sum_{i=1}^{9} c_i \lambda_i \ , \tag{4.24}$$

where $\lambda_9 = \mathbb{I}$ and $c_i = {\rm Tr}(\lambda_i\, \rho)/\mathcal{A}_i$, with $\mathcal{A}_i = {\rm Tr}\big(\lambda_i^2\big)$. Tables L.1, L.2 in App. L contains the explicit operator pool needed to extract each coefficient c_i, where the last column

formulates the c_i coefficient from the resulting measurement probabilities. For a generic system of N neutrinos, all combinations of the 7 operators should be implemented to obtain the corresponding density matrix. Once these coefficients are fixed, the single-neutrino entanglement von Neumann entropy can be obtained using $S = -\operatorname{Tr}\left[\rho_\nu \log(\rho_\nu)\right]$.

This three-flavor state tomography procedure is implemented on `ibm_torino` for the two-neutrino system using a single Trotter time step. This requires running 49 different quantum circuits (that describe all possible independent combinations of Tables L.1, L.2). Then, after applying the error mitigation methods, the coefficients $c_{ij} = \operatorname{Tr}(\lambda_i \otimes \lambda_j\, \rho)/\mathcal{A}_{ij}$ are evaluated, with $\mathcal{A}_{ij} = \operatorname{Tr}\left(\lambda_i^2 \otimes \lambda_j^2\right)$, via the probabilities listed in Tables L.1, L.2, L.3. The corresponding density matrix, labeled ρ_{IBM}, is obtained in a similar manner to Eq. (4.24),

$$\rho_{\text{IBM}} = \sum_{i,j=1}^{9} c_{ij} \lambda_i \otimes \lambda_j \ . \tag{4.25}$$

Due to hardware noise, ρ_{IBM} is generally not positive semi-definite, therefore it does not represent a physical density matrix. Here, the algorithm from Ref. [376] is applied to find the closest physical density matrix, labeled ρ_{CpDM}, via a rescaling of the eigenvalues (more details in App. L). Moreover, because in this case the density matrix of the whole system is computed, the final state is expected to be a pure quantum state. This can be enforced by using the eigenstate with the largest eigenvalue of ρ_{CpDM}. This state will correspond to the closest pure quantum state (it has the highest contribution in the Schmidt decomposition), and is labeled as ρ_{pure}.

The fidelity between the obtained ρ_{IBM}, ρ_{CpDM}, ρ_{pure} and the exact one, $\zeta = |\Psi(t)\rangle\langle\Psi(t)|$, is:

$$F(\rho, \zeta) = \left(\operatorname{Tr}\sqrt{\sqrt{\zeta}\rho\sqrt{\zeta}}\right)^2 \ . \tag{4.26}$$

Panel (a) of Fig. 4.13 shows the results. It is interesting to note that due to the error mitigation used here (the coefficients c_{ij} are all normalized using the same P_{id} quantity), the raw and DR $\rho_{\text{IBM}}/\operatorname{Tr}(\rho_{\text{IBM}})$ completely overlap, since the DR renormalization factor is cancelled out when enforcing the unity of the trace. Similarly, the ρ_{pure} does not depend on whether error mitigation is applied or not, since in this case the largest eigenvalue is the same.

Single neutrino entanglement entropy is also computed using the ρ_{CpDM} and ρ_{pure} density matrices,[8] shown in panel (b) of Fig. 4.13. Results from ρ_{pure} (dark blue points) are observed to be closer to the exact entropy behavior than the results from ρ_{CpDM} (green triangles). As a further test on the fidelity, the two-neutrino entropy for ρ_{CpDM} is computed to diagnose the effect of noise, since the analytical two-body entropy remains zero. These results are reported in panel (c) of Fig. 4.13, where while the fidelity is seen to be $> 90\%$, the density matrix ρ_{CpDM} still exhibits features of a mixed state.

4.6 Conclusions

In this work, we introduce new quantum circuits for simulating the collective dynamics of three-flavor neutrinos on gate-based quantum computers, and also provide an implementation of the two-neutrino flavor-exchange operator on qutrit-based computers using 4 CX gates. The implementation of the same dynamics on qubit-based platforms is demonstrated, where each neutrino is mapped to two qubits. The corresponding circuits require at least 18 CNOT gates. Additionally, we introduce a simplification that allows the realization of the required all-to-all connectivity in a linear chain without any additional computational costs (same circuit depth).

We have executed the qubit-based quantum circuits with up to eight neutrinos on the Quantinuum `H1-1` and IBM `ibm_torino` devices, and computed the probabilities of finding each neutrino in a specific flavor state, as well as the initial state persistence. These are key observables used to study the thermalization and equilibration of such systems [39]. For the smaller systems, with two and four neutrinos, the circuit depth is small enough that using multiple Trotter steps to perform time evolution is feasible. For eight neutrinos, while only one Trotter step was used, the resulting Trotter errors were smaller than the statistical and systematic uncertainties from the device. Hardware noise was corrected through various error mitigation techniques and post-selection procedures. The quality of the results (after mitigation) are higher in the trapped-ion device than the superconducting one, though the different number of shots used in both hinders a direct comparison.

[8] The matrix ρ_{IBM} cannot be used since it can have negative eigenvalues.

Using the IBM quantum computer, it was also possible to test the proposed partial state tomography, which required implementing 49 operators, allowing us to evaluate the full density matrix of two neutrinos and the entanglement entropy.

The algorithms needed to perform realistic simulations require quantum computers with longer coherence times. That is because one might need to start from a thermal state (and not a pure state) [377, 378, 379, 380], include the time-dependence in the two-neutrino term in the Hamiltonian [381, 324], or include the effect of anti-neutrinos.

Chapter 5

CONCLUSIONS

This thesis contains three distinct explorations of quantum information and simulation analyses of many-body neutrino systems. These investigations rest heavily on recent theoretical progress in both high-energy and condensed matter physics, specifically in many-body neutrino simulations and studies of far-from-equilibrium phenomena. The work contributes to the modern collective effort to characterize out-of-equilibrium dynamics of systems relevant to CCSNs and other astrophysical environments [126, 121, 315, 317, 38, 329, 156, 39]. The nascent numerical and analytical explorations within this document demonstrate how simple models used to describe many-body neutrino systems are still capable of hosting a wide array unexpected exotic quantum phenomena. Enforcing constraints from many-body neutrino models on what is ultimately a randomly coupled, long-range entangled Heisenberg spin system has provided a rich playground within which to explore a wide variety of exotic out-of-equilibrium quantum dynamics, in the context of high energy settings.

In Chapter 2, classical numerical simulations were used to study DQPT occurrences in long-range entangled randomly-coupled two-flavor neutrino many-body systems which were represented as spin chains. This work was grounded in the context of previous explorations of DQPTs in many-body neutrino systems, a recently hybridized research direction. The presence of distinct timescales in certain coupling configurations raises questions about symmetry structures within the original Hamiltonian and warrants further investigation.

The simulations themselves were TN-based computations of the time evolution of a randomly coupled, long-range entangled Heisenberg spin system. To accompany this, this thesis includes a discussion of TN methods and their utility for high energy physics computations. Originally developed for low-dimensional condensed matter models with short-range interactions, TNs have potential to provide useful qualitative insights for systems with more complex coupling structures. While TNs themselves are not naturally suited for systems hosting

volume-law scaling entanglement growth, TNs offer the most promising workaround to the computational bottleneck that inevitably emerges with ED computations. Computation of dynamical phenomena—such as entanglement growth and operator spreading—inevitably hit a limit via ED and other numerical methods in terms of computational resource consumption. TNs hold potential to circumvent this obstacle; this is being actively pursued in ongoing follow-up work related to the timescales study of Chapter 2. Tree Tensor Networks, Tensorial Neural Networks and novel MPO-based architectures [382, 383, 384, 385, 386] all warrant serious consideration for specialized application to the highly entangled systems typical to high-energy settings, such as those found in CCSNs, binary star mergers, and other highly energetic astrophysical environments.

Additionally, the work of chapter 2 invites deeper questions into how other quantum information observables and non-equilibrium phenomena in this many-body neutrino-grounded long-range entangled Heisenberg system scale in the long-time, large-N limit. Entanglement power [387], magic [388, 389, 390, 391], negativity [392, 393], n-tangles [129], thermal phase transitions [106], amongst many others, are under active consideration and pursuit. Extending Chapter 2's work beyond the two-level systems studied to d-level systems is another promising avenue of exploration. Future work will explore these directions further, including ongoing investigations of dynamical phase transitions in d-dimensional Hilbert spaces via both classical and quantum computational methods.

Chapter 3 explores the application of scrambling diagnostics to the same neutrino-motivated long-range entangled Heisenberg spin model, and numerically examining its connection to Loschmidt echo defined DQPTs. This diagnostic for operator growth, the out-of-time-ordered correlator (OTOC), originates in black hole and condensed matter physics. Such information spread and operator growth studies may shed light on statistically driven, ensemble-level behavior like flavor equilibration, and macroscopic phenomena like superfluidity [394, 395], and BCS-BEC crossover-like transitions [396, 397, 398]. The study also invites questions on the occurrence of quantum many-body localization and quantum many-body scarring in the same system, and how quantum complexity measures like magic [198, 389, 390, 399] might scale in such many-body localized, scarred, or scrambling systems. Expanding this study to also account for anisotropic neutrino velocity directions

and other features contributing to a more physically realistic neutrino many-body configuration [400], would be one of many natural extensions.

Chapter 4 covers a demonstrative implementation of three-flavor neutrino oscillations on both superconducting qubit (heavy-hex connectivity) and trapped ion-based (all-to-all connectivity) quantum hardware. This work demonstrated practical use cases for quantum devices in service of many-body neutrino system simulations, as well as computations of physical observables such as entanglement entropy and flavor persistence. These results contribute to ongoing efforts exploring the viability of quantum hardware for the simulation and computational needs of problems of interest within the high-energy physics community [401, 402]. Natural outflows from this investigation include utilization of the three-flavor circuits developed (for both three and two-level quantum platforms) to further explore other dynamical phenomena in three-flavor neutrino systems, and inclusion of anti-neutrinos as well. Studies of such three-level or other higher-level systems naturally lend motivation to explore error mitigation techniques and error correction protocols for such d-level systems [403, 404, 405], in order to tractably simulate longer time-evolution ranges on quantum devices, particularly d-level quantum platforms.

Altogether, the work contained within this thesis reinforce the relevance of quantum information techniques and tools in advancing the understanding of collective flavor dynamics and evolution within neutrino many-body systems. Tools spanning quantum information-motivated classical numerical methods for many-body quantum systems (like TNs) to quantum-based techniques (direct device simulation) contribute to this purpose, and this document's results assist in building a foundation for future investigations at the intersection of high-energy physics and quantum information and computation.

BIBLIOGRAPHY

[1] Ivan Esteban, Maria Conceptión González-García, Michele Maltoni, Thomas Schwetz, and Albert Zhou. The fate of hints: updated global analysis of three-flavor neutrino oscillations. *JHEP*, 09:178, 2020.

[2] Nufit 5.3, www.nu-fit.org, 2024.

[3] Quantinuum, 2024.

[4] M. Goldhaber, L. Grodzins, and A. W. Sunyar. Helicity of neutrinos. *Phys. Rev.*, 109:1015–1017, Feb 1958.

[5] Yoshiyuki Fukuda, T Hayakawa, E Ichihara, K Inoue, K Ishihara, Hirokazu Ishino, Y Itow, T Kajita, J Kameda, S Kasuga, et al. Evidence for oscillation of atmospheric neutrinos. *Physical review letters*, 81(8):1562, 1998.

[6] Y. Fukuda, T. Hayakawa, E. Ichihara, K. Inoue, K. Ishihara, H. Ishino, Y. Itow, T. Kajita, J. Kameda, S. Kasuga, K. Kobayashi, Y. Kobayashi, Y. Koshio, M. Miura, M. Nakahata, S. Nakayama, A. Okada, K. Okumura, N. Sakurai, M. Shiozawa, Y. Suzuki, Y. Takeuchi, Y. Totsuka, S. Yamada, M. Earl, A. Habig, E. Kearns, M. D. Messier, K. Scholberg, J. L. Stone, L. R. Sulak, C. W. Walter, M. Goldhaber, T. Barszczxak, D. Casper, W. Gajewski, P. G. Halverson, J. Hsu, W. R. Kropp, L. R. Price, F. Reines, M. Smy, H. W. Sobel, M. R. Vagins, K. S. Ganezer, W. E. Keig, R. W. Ellsworth, S. Tasaka, J. W. Flanagan, A. Kibayashi, J. G. Learned, S. Matsuno, V. J. Stenger, D. Takemori, T. Ishii, J. Kanzaki, T. Kobayashi, S. Mine, K. Nakamura, K. Nishikawa, Y. Oyama, A. Sakai, M. Sakuda, O. Sasaki, S. Echigo, M. Kohama, A. T. Suzuki, T. J. Haines, E. Blaufuss, B. K. Kim, R. Sanford, R. Svoboda, M. L. Chen, Z. Conner, J. A. Goodman, G. W. Sullivan, J. Hill, C. K. Jung, K. Martens, C. Mauger, C. McGrew, E. Sharkey, B. Viren, C. Yanagisawa, W. Doki, K. Miyano, H. Okazawa, C. Saji, M. Takahata, Y. Nagashima, M. Takita, T. Yamaguchi, M. Yoshida, S. B. Kim, M. Etoh, K. Fujita, A. Hasegawa, T. Hasegawa, S. Hatakeyama, T. Iwamoto, M. Koga, T. Maruyama, H. Ogawa, J. Shirai, A. Suzuki, F. Tsushima, M. Koshiba, M. Nemoto, K. Nishijima, T. Futagami, Y. Hayato, Y. Kanaya, K. Kaneyuki, Y. Watanabe, D. Kielczewska, R. A. Doyle, J. S. George, A. L. Stachyra, L. L. Wai, R. J. Wilkes, and K. K. Young. Evidence for oscillation of atmospheric neutrinos. *Phys. Rev. Lett.*, 81:1562–1567, Aug 1998.

[7] WC Haxton. The solar neutrino problem. *Annual Review of Astronomy and Astrophysics*, 33(1):459–503, 1995.

[8] Wick C Haxton, RG Hamish Robertson, and Aldo M Serenelli. Solar neutrinos: status and prospects. *Annual Review of Astronomy and Astrophysics*, 51:21–61, 2013.

[9] A. Mirizzi, I. Tamborra, H.-Th. Janka, N. Saviano, K. Scholberg, R. Bollig, L. Hüdepohl, and S. Chakraborty. Supernova Neutrinos: Production, Oscillations and Detection. *La Rivista del Nuovo Cimento*, 39(102):1–112, February 2016.

[10] AB Balantekin and Y Pehlivan. Neutrino–neutrino interactions and flavour mixing in dense matter. *Journal of Physics G: Nuclear and Particle Physics*, 34(1):47, 2006.

[11] Y. Pehlivan, A. B. Balantekin, Toshitaka Kajino, and Takashi Yoshida. Invariants of collective neutrino oscillations. *Phys. Rev. D*, 84:065008, Sep 2011.

[12] Huaiyu Duan, George M Fuller, and Yong-Zhong Qian. Collective neutrino oscillations. *Annual Review of Nuclear and Particle Science*, 60:569–594, 2010.

[13] Y. Abe, J. C. dos Anjos, J. C. Barriere, E. Baussan, I. Bekman, M. Bergevin, T. J. C. Bezerra, L. Bezrukov, E. Blucher, C. Buck, J. Busenitz, A. Cabrera, E. Caden, L. Camilleri, R. Carr, M. Cerrada, P.-J. Chang, E. Chauveau, P. Chimenti, A. P. Collin, E. Conover, J. M. Conrad, J. I. Crespo-Anadón, K. Crum, A. S. Cucoanes, E. Damon, J. V. Dawson, J. Dhooghe, D. Dietrich, Z. Djurcic, M. Dracos, M. Elnimr, A. Etenko, M. Fallot, F. von Feilitzsch, J. Felde, S. M. Fernandes, V. Fischer, D. Franco, M. Franke, H. Furuta, I. Gil-Botella, L. Giot, M. Göger-Neff, L. F. G. Gonzalez, L. Goodenough, M. C. Goodman, C. Grant, N. Haag, T. Hara, J. Haser, M. Hofmann, G. A. Horton-Smith, A. Hourlier, M. Ishitsuka, J. Jochum, C. Jollet, F. Kaether, L. N. Kalousis, Y. Kamyshkov, D. M. Kaplan, T. Kawasaki, E. Kemp, H. de Kerret, D. Kryn, M. Kuze, T. Lachenmaier, C. E. Lane, T. Lasserre, A. Letourneau, D. Lhuillier, H. P. Lima, M. Lindner, J. M. López-Castaño, J. M. LoSecco, B. Lubsandorzhiev, S. Lucht, J. Maeda, C. Mariani, J. Maricic, J. Martino, T. Matsubara, G. Mention, A. Meregaglia, T. Miletic, R. Milincic, A. Minotti, Y. Nagasaka, Y. Nikitenko, P. Novella, L. Oberauer, M. Obolensky, A. Onillon, A. Osborn, C. Palomares, I. M. Pepe, S. Perasso, P. Pfahler, A. Porta, G. Pronost, J. Reichenbacher, B. Reinhold, M. Röhling, R. Roncin, S. Roth, B. Rybolt, Y. Sakamoto, R. Santorelli, A. C. Schilithz, S. Schönert, S. Schoppmann, M. H. Shaevitz, R. Sharankova, S. Shimojima, D. Shrestha, V. Sibille, V. Sinev, M. Skorokhvatov, E. Smith, J. Spitz, A. Stahl, I. Stancu, L. F. F. Stokes, M. Strait, A. Stüken, F. Suekane, S. Sukhotin, T. Sumiyoshi, Y. Sun, R. Svoboda, K. Terao, A. Tonazzo, H. H. Trinh Thi, G. Valdiviesso, N. Vassilopoulos, C. Veyssiere, M. Vivier, S. Wagner, N. Walsh, H. Watanabe, C. Wiebusch, L. Winslow, M. Wurm, G. Yang, F. Yermia, and V. Zimmer. Improved measurements of the neutrino mixing angle 13 with the double chooz detector. *Journal of High Energy Physics*, 2014(10), October 2014.

[14] M Concepción González-Garciá and Yosef Nir. Neutrino masses and mixing: evidence and implications. *Reviews of Modern Physics*, 75(2):345, 2003.

[15] SP Mikheev and A Yu Smirnov. Resonance amplification of oscillations in matter and spectroscopy of solar neutrinos. *Yadernaya Fizika*, 42(6):1441–1448, 1985.

[16] L. Wolfenstein. Neutrino oscillations in matter. *Phys. Rev. D*, 17:2369–2374, May 1978.

[17] Martin J Savage, Robert A Malaney, and George M Fuller. Neutrino oscillations and the leptonic charge of the universe. *Astrophysical Journal*, 368(1):1–11, 1991.

[18] James Pantaleone. Neutrino oscillations at high densities. *Physics Letters B*, 287(1):128–132, 1992.

[19] James Pantaleone. Dirac neutrinos in dense matter. *Phys. Rev. D*, 46:510–523, Jul 1992.

[20] Bruce H. J. McKellar and Mark J. Thomson. Oscillating neutrinos in the early universe. *Phys. Rev. D*, 49:2710–2728, Mar 1994.

[21] Y Pehlivan, AB Balantekin, and Toshitaka Kajino. Exact methods for self interacting neutrinos. In *AIP Conference Proceedings*, pages 245–252. American Institute of Physics, 2014.

[22] R. F. Sawyer. 'Classical' instabilities and 'quantum' speed-up in the evolution of neutrino clouds, 8 2004.

[23] R. F. Sawyer. Speed-up of neutrino transformations in a supernova environment. *Phys. Rev. D*, 72:045003, Aug 2005.

[24] Raymond F Sawyer. Multiangle instability in dense neutrino systems. *Physical Review D*, 79(10):105003, 2009.

[25] George M Fuller, Ron W Mayle, James R Wilson, and David N Schramm. Resonant neutrino oscillations and stellar collapse. *Astrophysical Journal*, 322(2):795–803, 1987.

[26] Georg Raffelt and David Seckel. Bounds on exotic-particle interactions from sn1987a. *Physical Review Letters*, 60(18):1793, 1988.

[27] Günther Sigl and G Raffelt. General kinetic description of relativistic mixed neutrinos. *Nuclear Physics B*, 406:423–451, 1993.

[28] CK Jung, T Kajita, T Mann, and C McGrew. Oscillations of atmospheric neutrinos. *Annual Review of Nuclear and Particle Science*, 51(1):451–488, 2001.

[29] Masatoshi Koshiba. Nobel lecture: Birth of neutrino astrophysics. *Reviews of Modern Physics*, 75(3):1011, 2003.

[30] Shinya Wanajo, Yuichiro Sekiguchi, Nobuya Nishimura, Kenta Kiuchi, Koutarou Kyutoku, and Masaru Shibata. Production of all the r-process nuclides in the dynamical ejecta of neutron star mergers. *The Astrophysical Journal Letters*, 789(2):L39, 2014.

[31] RD Hoffman, SE Woosley, and Y-Z Qian. Nucleosynthesis in neutrino-driven winds. ii. implications for heavy element synthesis. *The Astrophysical Journal*, 482(2):951, 1997.

[32] Christian Winteler, Roger Kaeppeli, Albino Perego, Almudena Arcones, Nicolas Vasset, Nobuya Nishimura, Matthias Liebendoerfer, and F-K Thielemann. Magnetorotationally driven supernovae as the origin of early galaxy r-process elements? *The astrophysical journal letters*, 750(1):L22, 2012.

[33] Sergio Pastor, Georg Raffelt, and Dmitry V. Semikoz. Physics of synchronized neutrino oscillations caused by self-interactions. *Phys. Rev. D*, 65:053011, Feb 2002.

[34] Stuart Samuel. Bimodal coherence in dense self-interacting neutrino gases. *Physical Review D*, 53(10):5382, 1996.

[35] Sergio Pastor and Georg Raffelt. Flavor oscillations in the supernova hot bubble region: Nonlinear effects of neutrino background. *Phys. Rev. Lett.*, 89:191101, Oct 2002.

[36] AB Balantekin. Collective neutrino oscillations and nucleosynthesis. In *AIP Conference Proceedings*, page 020012. AIP Publishing LLC, 2018.

[37] Joshua D. Martin, A. Roggero, Huaiyu Duan, J. Carlson, and V. Cirigliano. Classical and quantum evolution in a simple coherent neutrino problem. *Phys. Rev. D*, 105:083020, Apr 2022.

[38] Joshua D. Martin, A. Roggero, Huaiyu Duan, and J. Carlson. Many-body neutrino flavor entanglement in a simple dynamic model, 2023.

[39] Joshua D. Martin, Duff Neill, A. Roggero, Huaiyu Duan, and J. Carlson. Equilibration of quantum many-body fast neutrino flavor oscillations. *Phys. Rev. D*, 108(12):123010, 2023.

[40] Huaiyu Duan, George M. Fuller, and Yong-Zhong Qian. Collective neutrino oscillations. *Annual Review of Nuclear and Particle Science*, 60(1):569–594, November 2010.

[41] Sovan Chakraborty, Rasmus Hansen, Ignacio Izaguirre, and Georg Raffelt. Collective neutrino flavor conversion: Recent developments. *Nucl. Phys. B*, 908:366–381, 2016.

[42] I. V. Oseledets. Tensor-train decomposition. *SIAM Journal on Scientific Computing*, 33(5):2295–2317, 2011.

[43] Roman Orus. A Practical Introduction to Tensor Networks: Matrix Product States and Projected Entangled Pair States. *Annals Phys.*, 349:117–158, 2014.

[44] Jacob C Bridgeman and Christopher T Chubb. Hand-waving and interpretive dance: an introductory course on tensor networks. *Journal of physics A: Mathematical and theoretical*, 50(22):223001, 2017.

[45] M. Fannes, B. Nachtergaele, and R. F. Werner. FINITELY CORRELATED STATES ON QUANTUM SPIN CHAINS. *Commun. Math. Phys.*, 144:443–490, 1992.

[46] A. Klümper, A. Schadschneider, and J. Zittartz. Groundstate properties of a generalized VBS-model. *Zeitschrift fur Physik B Condensed Matter*, 87(3):281–287, October 1992.

[47] Stellan Östlund and Stefan Rommer. Thermodynamic limit of density matrix renormalization. *Phys. Rev. Lett.*, 75:3537–3540, Nov 1995.

[48] Guifré Vidal. Efficient classical simulation of slightly entangled quantum computations. *Phys. Rev. Lett.*, 91:147902, Oct 2003.

[49] F. Verstraete and J. I. Cirac. Renormalization algorithms for quantum-many body systems in two and higher dimensions. 7 2004.

[50] F. Verstraete and J. I. Cirac. Valence-bond states for quantum computation. *Phys. Rev. A*, 70:060302, Dec 2004.

[51] Steven R. White. Density matrix formulation for quantum renormalization groups. *Phys. Rev. Lett.*, 69:2863–2866, Nov 1992.

[52] Guifré Vidal. Efficient simulation of one-dimensional quantum many-body systems. *Phys. Rev. Lett.*, 93:040502, Jul 2004.

[53] F. Verstraete, J. J. García-Ripoll, and J. I. Cirac. Matrix product density operators: Simulation of finite-temperature and dissipative systems. *Phys. Rev. Lett.*, 93:207204, Nov 2004.

[54] Jutho Haegeman, J. Ignacio Cirac, Tobias J. Osborne, Iztok Pižorn, Henri Verschelde, and Frank Verstraete. Time-dependent variational principle for quantum lattices. *Physical Review Letters*, 107(7), August 2011.

[55] Jutho Haegeman, Christian Lubich, Ivan Oseledets, Bart Vandereycken, and Frank Verstraete. Unifying time evolution and optimization with matrix product states. *Phys. Rev. B*, 94:165116, Oct 2016.

[56] M. Gell-Mann and F. E. Low. Quantum electrodynamics at small distances. *Phys. Rev.*, 95:1300–1312, Sep 1954.

[57] F. J. Dyson. The radiation theories of tomonaga, schwinger, and feynman. *Phys. Rev.*, 75:486–502, Feb 1949.

[58] Julian Schwinger. Quantum electrodynamics. ii. vacuum polarization and self-energy. *Phys. Rev.*, 75:651–679, Feb 1949.

[59] J. C. Ward. An identity in quantum electrodynamics. *Phys. Rev.*, 78:182–182, Apr 1950.

[60] Y. Takahashi. On the generalized Ward identity. *Nuovo Cim.*, 6:371, 1957.

[61] Franz Gross, Eberhard Klempt, Stanley J. Brodsky, Andrzej J. Buras, Volker D. Burkert, Gudrun Heinrich, Karl Jakobs, Curtis A. Meyer, Kostas Orginos, Michael Strickland, Johanna Stachel, Giulia Zanderighi, Nora Brambilla, Peter Braun-Munzinger, Daniel Britzger, Simon Capstick, Tom Cohen, Volker Crede, Martha Constantinou, Christine Davies, Luigi Del Debbio, Achim Denig, Carleton DeTar, Alexandre Deur, Yuri Dokshitzer, Hans Günter Dosch, Jozef Dudek, Monica Dunford, Evgeny Epelbaum, Miguel A. Escobedo, Harald Fritzsch, Kenji Fukushima, Paolo Gambino, Dag Gillberg, Steven Gottlieb, Per Grafstrom, Massimiliano Grazzini, Boris Grube, Alexey Guskov, Toru Iijima, Xiangdong Ji, Frithjof Karsch, Stefan Kluth, John B. Kogut, Frank Krauss, Shunzo Kumano, Derek Leinweber, Heinrich Leutwyler, Hai-Bo Li, Yang Li, Bogdan Malaescu, Chiara Mariotti, Pieter Maris, Simone Marzani, Wally Melnitchouk, Johan Messchendorp, Harvey Meyer, Ryan Edward Mitchell, Chandan Mondal, Frank Nerling, Sebastian Neubert, Marco Pappagallo, Saori Pastore, José R. Peláez, Andrew Puckett, Jianwei Qiu, Klaus Rabbertz, Alberto Ramos, Patrizia Rossi, Anar Rustamov, Andreas Schäfer, Stefan Scherer, Matthias Schindler, Steven Schramm, Mikhail Shifman, Edward Shuryak, Torbjörn Sjöstrand, George Sterman, Iain W. Stewart, Joachim Stroth, Eric Swanson, Guy F. de Téramond, Ulrike Thoma, Antonio Vairo, Danny van Dyk, James Vary, Javier Virto, Marcel Vos, Christian Weiss, Markus Wobisch, Sau Lan Wu, Christopher Young, Feng Yuan, Xingbo Zhao, and Xiaorong Zhou. 50 years of quantum chromodynamics: Introduction and review. *The European Physical Journal C*, 83(12), December 2023.

[62] W. Pauli and F. Villars. On the invariant regularization in relativistic quantum theory. *Rev. Mod. Phys.*, 21:434–444, Jul 1949.

[63] Hermès Bélusca-Maïto, Amon Ilakovac, Paul Kühler, Marija Maor-Božinović, Dominik Stöckinger, and Matthias Weißwange. Introduction to renormalization theory and chiral gauge theories in dimensional regularization with non-anticommuting γ_5, 2023.

[64] Gerard 't Hooft and M. J. G. Veltman. Regularization and Renormalization of Gauge Fields. *Nucl. Phys. B*, 44:189–213, 1972.

[65] Kenneth G. Wilson. The renormalization group: Critical phenomena and the kondo problem. *Rev. Mod. Phys.*, 47:773–840, Oct 1975.

[66] N. N. Bogoliubov and O. S. Parasiuk. On the Multiplication of the causal function in the quantum theory of fields. *Acta Math.*, 97:227–266, 1957.

[67] Klaus Hepp. Proof of the Bogolyubov-Parasiuk theorem on renormalization. *Commun. Math. Phys.*, 2:301–326, 1966.

[68] W. Zimmermann. The power counting theorem for minkowski metric. *Commun. Math. Phys.*, 11:1–8, 1968.

[69] W. Zimmermann. Convergence of Bogolyubov's method of renormalization in momentum space. *Commun. Math. Phys.*, 15:208–234, 1969.

[70] J. Kondo. Resistance Minimum in Dilute Magnetic Alloys. *Prog. Theor. Phys.*, 32(1):37–49, 1964.

[71] B. Béri and N. R. Cooper. Topological kondo effect with majorana fermions. *Physical Review Letters*, 109(15), October 2012.

[72] Jonas B. Rigo and Andrew K. Mitchell. Unsupervised learning of effective quantum impurity models. *Phys. Rev. Res.*, 6:043044, Oct 2024.

[73] Martino Stefanini, Yi-Fan Qu, Tilman Esslinger, Sarang Gopalakrishnan, Eugene Demler, and Jamir Marino. Dissipative realization of Kondo models. *Communications Physics*, 8, 2025. Published 22 May 2025.

[74] H. R. Krishna-murthy, J. W. Wilkins, and K. G. Wilson. Renormalization-group approach to the anderson model of dilute magnetic alloys. i. static properties for the symmetric case. *Phys. Rev. B*, 21:1003–1043, Feb 1980.

[75] Ralf Bulla, Theo A. Costi, and Thomas Pruschke. Numerical renormalization group method for quantum impurity systems. *Rev. Mod. Phys.*, 80:395–450, Apr 2008.

[76] Steven R. White and Adrian E. Feiguin. Real-time evolution using the density matrix renormalization group. *Phys. Rev. Lett.*, 93:076401, Aug 2004.

[77] A J Daley, C Kollath, U Schollwöck, and G Vidal. Time-dependent density-matrix renormalization-group using adaptive effective hilbert spaces. *Journal of Statistical Mechanics: Theory and Experiment*, 2004(04):P04005, April 2004.

[78] Gabriele De Chiara, Matteo Rizzi, Davide Rossini, and Simone Montangero. Density matrix renormalization group for dummies. *Journal of Computational and Theoretical Nanoscience*, 5(7):1277–1288, July 2008.

[79] Ulrich Schollwöck. The density-matrix renormalization group in the age of matrix product states. *Annals of Physics*, 326(1):96–192, January 2011.

[80] U. Schollwöck. The density-matrix renormalization group. *Rev. Mod. Phys.*, 77:259–315, Apr 2005.

[81] U. Schollwoeck and S. R. White. Methods for time dependence in dmrg, 2006.

[82] A. L. Malvezzi. An introduction to numerical methods in low-dimensional quantum systems, 2003.

[83] Reinhard M. Noack. Diagonalization- and numerical renormalization-group-based methods for interacting quantum systems. In *AIP Conference Proceedings*, volume 789, page 93–163. AIP, 2005.

[84] I. Peschel, N. Kaulke, X. Q. Wang, and K. Hallberg, editors. *Density-matrix renormalization: A new numerical method in physics. Proceedings, Seminar and Workshop, Dresden, Germany, August 24-September 18, 1998*, Berlin, 1999. Springer.

[85] Karen A. Hallberg. New trends in density matrix renormalization. *Advances in Physics*, 55(5–6):477–526, July 2006.

[86] Sebastian Paeckel, Thomas Köhler, Andreas Swoboda, Salvatore R. Manmana, Ulrich Schollwöck, and Claudius Hubig. Time-evolution methods for matrix-product states. *Annals of Physics*, 411:167998, 2019.

[87] Michael Zwolak and Guifré Vidal. Mixed-state dynamics in one-dimensional quantum lattice systems: A time-dependent superoperator renormalization algorithm. *Phys. Rev. Lett.*, 93:207205, Nov 2004.

[88] Román Orús. A practical introduction to tensor networks: Matrix product states and projected entangled pair states. *Annals of physics*, 349:117–158, 2014.

[89] Guifré Vidal. Efficient simulation of one-dimensional quantum many-body systems. *Phys. Rev. Lett.*, 93:040502, Jul 2004.

[90] Hale F. Trotter. On the product of semi-groups of operators. *Proceedings of the American Mathematical Society*, 10(4):545–551, 1959. Accessed: 2025-05-25.

[91] Naomichi Hatano and Masuo Suzuki. *Finding Exponential Product Formulas of Higher Orders*, page 37–68. Springer Berlin Heidelberg, November 2005.

[92] Mingru Yang and Steven R. White. Time-dependent variational principle with ancillary krylov subspace. *Phys. Rev. B*, 102:094315, Sep 2020.

[93] Jutho Haegeman, J. Ignacio Cirac, Tobias J. Osborne, Iztok Pižorn, Henri Verschelde, and Frank Verstraete. Time-dependent variational principle for quantum lattices. *Phys. Rev. Lett.*, 107:070601, Aug 2011.

[94] Michael P. Zaletel, Roger S. K. Mong, Christoph Karrasch, Joel E. Moore, and Frank Pollmann. Time-evolving a matrix product state with long-ranged interactions. *Phys. Rev. B*, 91:165112, Apr 2015.

[95] Pengfei Zhang, Chunxiao Liu, and Xiao Chen. Subsystem rényi entropy of thermal ensembles for syk-like models. *SciPost Physics*, 8(6), June 2020.

[96] Mari Carmen Bañuls, Michal P. Heller, Karl Jansen, Johannes Knaute, and Viktor Svensson. Quantum information perspective on meson melting. *Physical Review D*, 108(7), October 2023.

[97] Simone Montangero, Enrique Rico, and Pietro Silvi. Loop-free tensor networks for high-energy physics. *Philosophical Transactions of the Royal Society A: Mathematical, Physical and Engineering Sciences*, 380(2216), December 2021.

[98] Mari Carmen Bañuls, Rainer Blatt, Jacopo Catani, Alessio Celi, Juan Ignacio Cirac, Marcello Dalmonte, Leonardo Fallani, Karl Jansen, Maciej Lewenstein, Simone Montangero, Christine A. Muschik, Benni Reznik, Enrique Rico, Luca Tagliacozzo, Karel Van Acoleyen, Frank Verstraete, Uwe-Jens Wiese, Matthew Wingate, Jakub Zakrzewski, and Peter Zoller. Simulating lattice gauge theories within quantum technologies. *The European Physical Journal D*, 74(8), August 2020.

[99] Milan Vujinovic. Tensor representations of lattice vertices from hypercubic symmetry, 2019.

[100] Julian Schuhmacher, Marco Ballarin, Alberto Baiardi, Giuseppe Magnifico, Francesco Tacchino, Simone Montangero, and Ivano Tavernelli. Hybrid tree tensor networks for quantum simulation. *PRX Quantum*, 6:010320, Jan 2025.

[101] Johnnie Gray and Garnet Kin-Lic Chan. Hyperoptimized approximate contraction of tensor networks with arbitrary geometry. *Phys. Rev. X*, 14:011009, Jan 2024.

[102] J. Ignacio Cirac, David Pérez-García, Norbert Schuch, and Frank Verstraete. Matrix product states and projected entangled pair states: Concepts, symmetries, theorems. *Rev. Mod. Phys.*, 93:045003, Dec 2021.

[103] Siddhartha Patra, Sukhbinder Singh, and Román Orús. Projected entangled pair states with flexible geometry. *Phys. Rev. Res.*, 7:L012002, Jan 2025.

[104] Ariel Kelman, Umberto Borla, Itay Gomelski, Jonathan Elyovich, Gertian Roose, Patrick Emonts, and Erez Zohar. Gauged gaussian projected entangled pair states: A high dimensional tensor network formulation for lattice gauge theories. *Physical Review D*, 110(5), September 2024.

[105] G. Vidal. Class of quantum many-body states that can be efficiently simulated. *Phys. Rev. Lett.*, 101:110501, Sep 2008.

[106] Mari Carmen Bañuls, Krzysztof Cichy, Hao-Ti Hung, Ying-Jer Kao, C. J. David Lin, and Amit Singh. Dynamical quantum phase transition and thermal equilibrium in the lattice thirring model, 2024.

[107] Mari Carmen Bañuls, Krzysztof Cichy, J. Ignacio Cirac, Karl Jansen, and Stefan Kühn. Tensor networks and their use for lattice gauge theories. In *Proceedings of The 36th Annual International Symposium on Lattice Field Theory — PoS(LATTICE2018)*, LATTICE2018, page 022. Sissa Medialab, May 2019.

[108] Ron Belyansky, Seth Whitsitt, Niklas Mueller, Ali Fahimniya, Elizabeth R. Bennewitz, Zohreh Davoudi, and Alexey V. Gorshkov. High-energy collision of quarks and mesons in the schwinger model: From tensor networks to circuit qed. *Phys. Rev. Lett.*, 132:091903, Feb 2024.

[109] Irene Papaefstathiou, Johannes Knolle, and Mari Carmen Bañuls. Real-time scattering in the lattice schwinger model. *Physical Review D*, 111(1), January 2025.

[110] João Barata and Enrique Rico. Real-time simulation of jet energy loss and entropy production in high-energy scattering with matter, 2025.

[111] Reinis Irmejs, Mari-Carmen Bañuls, and J. Ignacio Cirac. Quantum simulation of z_2 lattice gauge theory with minimal resources. *Phys. Rev. D*, 108:074503, Oct 2023.

[112] Patrick Emonts, Mari Carmen Bañuls, Ignacio Cirac, and Erez Zohar. Variational monte carlo simulation with tensor networks of a pure Z_3 gauge theory in $(2+1)$D. *Phys. Rev. D*, 102:074501, Oct 2020.

[113] Raghav G. Jha, Ashley Milsted, Dominik Neuenfeld, John Preskill, and Pedro Vieira. Real-time scattering in ising field theory using matrix product states, 2024.

[114] Ron Belyansky, Seth Whitsitt, Niklas Mueller, Ali Fahimniya, Elizabeth R. Bennewitz, Zohreh Davoudi, and Alexey V. Gorshkov. High-energy collision of quarks and mesons in the schwinger model: From tensor networks to circuit qed. *Physical Review Letters*, 132(9), February 2024.

[115] Manuel Schneider, Mari Carmen Bañuls, Krzysztof Cichy, and C.-J. David Lin. Parton distribution functions in the schwinger model with tensor networks. In *Proceedings of The 41st International Symposium on Lattice Field Theory — PoS(LATTICE2024)*, LATTICE2024, page 024. Sissa Medialab, February 2025.

[116] Mari Carmen Bañuls, Krzysztof Cichy, C. J. David Lin, and Manuel Schneider. Parton distribution functions in the schwinger model from tensor network states, 2025.

[117] Zhong-Bo Kang, Noah Moran, Peter Nguyen, and Wenyang Qian. Partonic distribution functions and amplitudes using tensor network methods. 1 2025.

[118] Mari Carmen Bañuls and Krzysztof Cichy. Review on novel methods for lattice gauge theories. *Reports on Progress in Physics*, 83(2):024401, January 2020.

[119] Giuseppe Magnifico, Giovanni Cataldi, Marco Rigobello, Peter Majcen, Daniel Jaschke, Pietro Silvi, and Simone Montangero. Tensor networks for lattice gauge theories beyond one dimension: a roadmap, 2024.

[120] L. Tagliacozzo, A. Celi, and M. Lewenstein. Tensor networks for lattice gauge theories with continuous groups. *Phys. Rev. X*, 4:041024, Nov 2014.

[121] Alessandro Roggero. Entanglement and many-body effects in collective neutrino oscillations. *Phys. Rev. D*, 104:103016, Nov 2021.

[122] Alessandro Roggero, Ermal Rrapaj, and Zewei Xiong. Entanglement and correlations in fast collective neutrino flavor oscillations. *Phys. Rev. D*, 106:043022, Aug 2022.

[123] Nicole F Bell, Andrew A Rawlinson, and RF Sawyer. Speed-up through entanglement—many-body effects in neutrino processes. *Physics Letters B*, 573:86–93, 2003.

[124] Ermal Rrapaj. Exact solution of multiangle quantum many-body collective neutrino-flavor oscillations. *Phys. Rev. C*, 101:065805, Jun 2020.

[125] Amol V. Patwardhan, Michael J. Cervia, and A. B. Balantekin. Spectral splits and entanglement entropy in collective neutrino oscillations. *Phys. Rev. D*, 104:123035, Dec 2021.

[126] Alessandro Roggero. Dynamical phase transitions in models of collective neutrino oscillations. *Phys. Rev. D*, 104:123023, Dec 2021.

[127] Benjamin Hall, Alessandro Roggero, Alessandro Baroni, and Joseph Carlson. Simulation of collective neutrino oscillations on a quantum computer. *Phys. Rev. D*, 104:063009, Sep 2021.

[128] Marc Illa and Martin J Savage. Basic elements for simulations of standard-model physics with quantum annealers: Multigrid and clock states. *Physical Review A*, 106(5):052605, 2022.

[129] Marc Illa and Martin J. Savage. Multi-neutrino entanglement and correlations in dense neutrino systems. *Phys. Rev. Lett.*, 130:221003, May 2023.

[130] Amol V Patwardhan, Michael J Cervia, Ermal Rrapaj, Pooja Siwach, and AB Balantekin. Many-body collective neutrino oscillations: recent developments. *arXiv preprint arXiv:2301.00342*, 2023.

[131] Natalie Klco, Alessandro Roggero, and Martin J Savage. Standard model physics and the digital quantum revolution: thoughts about the interface. *Reports on Progress in Physics*, 85(6):064301, may 2022.

[132] Ramya Bhaskar, Alessandro Roggero, and Martin J. Savage. Timescales in many-body fast-neutrino-flavor conversion. *Phys. Rev. C*, 110:045801, Oct 2024.

[133] A. Burrows and D. Vartanyan. Core-collapse supernova explosion theory. *Nature*, 589(7840):29–39, January 2021.

[134] B. Müller. Neutrino emission as diagnostics of core-collapse supernovae. *Annual Review of Nuclear and Particle Science*, 69(1):253–278, 2019.

[135] S. W. Bruenn, A. Mezzacappa, W. R. Hix, J. M. Blondin, P. Marronetti, O. E. B. Messer, C. J. Dirk, and S. Yoshida. 2D and 3D Core-Collapse Supernovae Simulation Results Obtained with the CHIMERA Code. *J. Phys. Conf. Ser.*, 180:012018, 2009.

[136] S. W. Bruenn, C. J. Dirk, A. Mezzacappa, J. C. Hayes, J. M. Blondin, W. R. Hix, and O. E. B. Messer. Modeling core collapse supernovae in 2 and 3 dimensions with spectral neutrino transport. *J. Phys. Conf. Ser.*, 46:393–402, 2006.

[137] R. L. Workman and Others. Review of Particle Physics. *PTEP*, 2022:083C01, 2022.

[138] G. M. Fuller, R. W. Mayle, J. R. Wilson, and D. N. Schramm. Resonant Neutrino Oscillations and Stellar Collapse. , 322:795, November 1987.

[139] V. Alan Kostelecký and Stuart Samuel. Self-maintained coherent oscillations in dense neutrino gases. *Phys. Rev. D*, 52:621–627, Jul 1995.

[140] Huaiyu Duan, George M. Fuller, and Yong-Zhong Qian. Collective neutrino flavor transformation in supernovae. *Phys. Rev. D*, 74:123004, Dec 2006.

[141] Huaiyu Duan, George M. Fuller, J. Carlson, and Yong-Zhong Qian. Simulation of coherent nonlinear neutrino flavor transformation in the supernova environment: Correlated neutrino trajectories. *Phys. Rev. D*, 74:105014, Nov 2006.

[142] Sovan Chakraborty, Rasmus Hansen, Ignacio Izaguirre, and Georg Raffelt. Collective neutrino flavor conversion: Recent developments. *Nuclear Physics B*, 908:366–381, 2016. Neutrino Oscillations: Celebrating the Nobel Prize in Physics 2015.

[143] Irene Tamborra and Shashank Shalgar. New developments in flavor evolution of a dense neutrino gas. *Annual Review of Nuclear and Particle Science*, 71(1):165–188, 2021.

[144] Hiroki Nagakura, Adam Burrows, Lucas Johns, and George M. Fuller. Where, when, and why: Occurrence of fast-pairwise collective neutrino oscillation in three-dimensional core-collapse supernova models. *Phys. Rev. D*, 104:083025, Oct 2021.

[145] Hiroki Nagakura. Roles of fast neutrino-flavor conversion on the neutrino-heating mechanism of core-collapse supernova. *Phys. Rev. Lett.*, 130:211401, May 2023.

[146] Alexey Vlasenko, George M. Fuller, and Vincenzo Cirigliano. Neutrino quantum kinetics. *Phys. Rev. D*, 89:105004, May 2014.

[147] Daniel N. Blaschke and Vincenzo Cirigliano. Neutrino quantum kinetic equations: The collision term. *Phys. Rev. D*, 94:033009, Aug 2016.

[148] Alexander Friedland and Cecilia Lunardini. Do many-particle neutrino interactions cause a novel coherent effect? *Journal of High Energy Physics*, 2003(10):043, 2003.

[149] Alexander Friedland and Cecilia Lunardini. Neutrino flavor conversion in a neutrino background: Single particle versus multiparticle description. *Phys. Rev. D*, 68:013007, 2003.

[150] RF Sawyer. " classical" instabilities and" quantum" speed-up in the evolution of neutrino clouds. *arXiv preprint hep-ph/0408265*, 2004.

[151] Michael J. Cervia, Amol V. Patwardhan, A. B. Balantekin, S. N. Coppersmith, and Calvin W. Johnson. Entanglement and collective flavor oscillations in a dense neutrino gas. *Phys. Rev. D*, 100:083001, Oct 2019.

[152] Zewei Xiong. Many-body effects of collective neutrino oscillations. *Phys. Rev. D*, 105:103002, May 2022.

[153] Michael J. Cervia, Pooja Siwach, Amol V. Patwardhan, A. B. Balantekin, S. N. Coppersmith, and Calvin W. Johnson. Collective neutrino oscillations with tensor networks using a time-dependent variational principle. *Phys. Rev. D*, 105:123025, Jun 2022.

[154] Denis Lacroix, A. B. Balantekin, Michael J. Cervia, Amol V. Patwardhan, and Pooja Siwach. Role of non-gaussian quantum fluctuations in neutrino entanglement. *Phys. Rev. D*, 106:123006, Dec 2022.

[155] Pooja Siwach, Anna M. Suliga, and A. Baha Balantekin. Entanglement in three-flavor collective neutrino oscillations. *Phys. Rev. D*, 107:023019, Jan 2023.

[156] Joshua D. Martin, Duff Neill, A. Roggero, Huaiyu Duan, and J. Carlson. Equilibration of quantum many-body fast neutrino flavor oscillations. *Phys. Rev. D*, 108:123010, Dec 2023.

[157] Shashank Shalgar and Irene Tamborra. Do we have enough evidence to invalidate the mean-field approximation adopted to model collective neutrino oscillations? *Phys. Rev. D*, 107(12):123004, 2023.

[158] Lucas Johns. Neutrino many-body correlations, 5 2023.

[159] John Preskill. Quantum computing in the nisq era and beyond. *Quantum*, 2:79, August 2018.

[160] Valentina Amitrano, Alessandro Roggero, Piero Luchi, Francesco Turro, Luca Vespucci, and Francesco Pederiva. Trapped-ion quantum simulation of collective neutrino oscillations. *Phys. Rev. D*, 107:023007, Jan 2023.

[161] Pooja Siwach, Kaytlin Harrison, and A. Baha Balantekin. Collective neutrino oscillations on a quantum computer with hybrid quantum-classical algorithm. *Phys. Rev. D*, 108:083039, Oct 2023.

[162] A. B. Balantekin, Michael J. Cervia, Amol V. Patwardhan, Ermal Rrapaj, and Pooja Siwach. Quantum information and quantum simulation of neutrino physics. *The European Physical Journal A*, 59(8), August 2023.

[163] Christian W. Bauer, Zohreh Davoudi, A. Baha Balantekin, Tanmoy Bhattacharya, Marcela Carena, Wibe A. de Jong, Patrick Draper, Aida El-Khadra, Nate Gemelke, Masanori Hanada, Dmitri Kharzeev, Henry Lamm, Ying-Ying Li, Junyu Liu, Mikhail Lukin, Yannick Meurice, Christopher Monroe, Benjamin Nachman, Guido Pagano,

John Preskill, Enrico Rinaldi, Alessandro Roggero, David I. Santiago, Martin J. Savage, Irfan Siddiqi, George Siopsis, David Van Zanten, Nathan Wiebe, Yukari Yamauchi, Kübra Yeter-Aydeniz, and Silvia Zorzetti. Quantum simulation for high-energy physics. *PRX Quantum*, 4:027001, May 2023.

[164] Damiano F. G. Fiorillo and Georg G. Raffelt. Slow and fast collective neutrino oscillations: Invariants and reciprocity. *Phys. Rev. D*, 107:043024, Feb 2023.

[165] Ian Padilla-Gay, Irene Tamborra, and Georg G. Raffelt. Neutrino flavor pendulum reloaded: The case of fast pairwise conversion. *Phys. Rev. Lett.*, 128:121102, Mar 2022.

[166] M. Heyl, A. Polkovnikov, and S. Kehrein. Dynamical quantum phase transitions in the transverse-field ising model. *Phys. Rev. Lett.*, 110:135704, Mar 2013.

[167] Markus Heyl. Dynamical quantum phase transitions: a review. *Reports on Progress in Physics*, 81(5):054001, 2018.

[168] Bojan Žunkovič, Markus Heyl, Michael Knap, and Alessandro Silva. Dynamical quantum phase transitions in spin chains with long-range interactions: Merging different concepts of nonequilibrium criticality. *Phys. Rev. Lett.*, 120:130601, Mar 2018.

[169] M. Heyl. Dynamical quantum phase transitions in systems with broken-symmetry phases. *Phys. Rev. Lett.*, 113:205701, Nov 2014.

[170] Arka Banerjee, Amol Dighe, and Georg Raffelt. Linearized flavor-stability analysis of dense neutrino streams. *Phys. Rev. D*, 84:053013, Sep 2011.

[171] Ignacio Izaguirre, Georg Raffelt, and Irene Tamborra. Fast pairwise conversion of supernova neutrinos: A dispersion relation approach. *Physical review letters*, 118(2):021101, 2017.

[172] Sagar Airen, Francesco Capozzi, Sovan Chakraborty, Basudeb Dasgupta, Georg Raffelt, and Tobias Stirner. Normal-mode analysis for collective neutrino oscillations. *Journal of Cosmology and Astroparticle Physics*, 2018(12):019, dec 2018.

[173] Subir Sachdev. Quantum phase transitions. *Physics world*, 12(4):33, 1999.

[174] Giancarlo Calvanese Strinati, Pierbiagio Pieri, Gerd Röpke, Peter Schuck, and Michael Urban. The bcs–bec crossover: From ultra-cold fermi gases to nuclear systems. *Physics Reports*, 738:1–76, 2018.

[175] Markus Heyl. Scaling and universality at dynamical quantum phase transitions. *Physical Review Letters*, 115(14):140602, 2015.

[176] P Jurcevic, H Shen, P Hauke, C Maier, T Brydges, C Hempel, BP Lanyon, Markus Heyl, R Blatt, and CF Roos. Direct observation of dynamical quantum phase transitions in an interacting many-body system. *Physical review letters*, 119(8):080501, 2017.

[177] Christian Gogolin and Jens Eisert. Equilibration, thermalisation, and the emergence of statistical mechanics in closed quantum systems. *Reports on Progress in Physics*, 79(5):056001, 2016.

[178] Aditi Mitra. Quantum quench dynamics. *Annual Review of Condensed Matter Physics*, 9:245–259, 2018.

[179] Thomas Gorin, Tomaž Prosen, Thomas H Seligman, and Marko Žnidarič. Dynamics of loschmidt echoes and fidelity decay. *Physics Reports*, 435(2-5):33–156, 2006.

[180] Alessandro Silva. Statistics of the work done on a quantum critical system by quenching a control parameter. *Phys. Rev. Lett.*, 101:120603, Sep 2008.

[181] Andrea Gambassi and Alessandro Silva. Large deviations and universality in quantum quenches. *Phys. Rev. Lett.*, 109:250602, Dec 2012.

[182] Matthew Fishman, Steven R. White, and E. Miles Stoudenmire. The ITensor Software Library for Tensor Network Calculations. *SciPost Phys. Codebases*, page 4, 2022.

[183] Sebastian Paeckel, Thomas Köhler, Andreas Swoboda, Salvatore R Manmana, Ulrich Schollwöck, and Claudius Hubig. Time-evolution methods for matrix-product states. *Annals of Physics*, 411:167998, 2019.

[184] Masuo Suzuki. Generalized trotter's formula and systematic approximants of exponential operators and inner derivations with applications to many-body problems. *Communications in Mathematical Physics*, 51(2):183–190, 1976.

[185] Michael L. Wagman and Martin J. Savage. Statistics of baryon correlation functions in lattice qcd. *Phys. Rev. D*, 96:114508, Dec 2017.

[186] George M Fuller and Yong-Zhong Qian. Simultaneous flavor transformation of neutrinos and antineutrinos with dominant potentials from neutrino-neutrino forward scattering. *Physical Review D*, 73(2):023004, 2006.

[187] Bradley S. Meyer, Gail C. McLaughlin, and George M. Fuller. Neutrino capture and r-process nucleosynthesis. *Phys. Rev. C*, 58:3696–3710, Dec 1998.

[188] AB Balantekin and H Yüksel. Neutrino mixing and nucleosynthesis in core-collapse supernovae. *New Journal of Physics*, 7(1):51, 2005.

[189] Takashi Yoshida, Toshitaka Kajino, Hidekazu Yokomakura, Keiichi Kimura, Akira Takamura, and Dieter H. Hartmann. Supernova neutrino nucleosynthesis of light elements with neutrino oscillations. *Phys. Rev. Lett.*, 96:091101, Mar 2006.

[190] Milad Delfan Azari, Shoichi Yamada, Taiki Morinaga, Hiroki Nagakura, Shun Furusawa, Akira Harada, Hirotada Okawa, Wakana Iwakami, and Kohsuke Sumiyoshi. Fast collective neutrino oscillations inside the neutrino sphere in core-collapse supernovae. *Phys. Rev. D*, 101:023018, Jan 2020.

[191] G Martínez-Pinedo, T Fischer, and L Huther. Supernova neutrinos and nucleosynthesis. *Journal of Physics G: Nuclear and Particle Physics*, 41(4):044008, 2014.

[192] Zewei Xiong, Andre Sieverding, Manibrata Sen, and Yong-Zhong Qian. Potential impact of fast flavor oscillations on neutrino-driven winds and their nucleosynthesis. *The Astrophysical Journal*, 900(2):144, 2020.

[193] Francesco Capozzi, Madhurima Chakraborty, Sovan Chakraborty, and Manibrata Sen. Mu-tau neutrinos: Influencing fast flavor conversions in supernovae. *Phys. Rev. Lett.*, 125:251801, Dec 2020.

[194] Raymond F Sawyer. Neutrino cloud instabilities just above the neutrino sphere of a supernova. *Physical Review Letters*, 116(8):081101, 2016.

[195] Alaina M. Green, A. Elben, C. Huerta Alderete, Lata Kh Joshi, Nhung H. Nguyen, Torsten V. Zache, Yingyue Zhu, Bhuvanesh Sundar, and Norbert M. Linke. Experimental measurement of out-of-time-ordered correlators at finite temperature. *Phys. Rev. Lett.*, 128:140601, Apr 2022.

[196] Xinfang Nie, Bo-Bo Wei, Xi Chen, Ze Zhang, Xiuzhu Zhao, Chudan Qiu, Yu Tian, Yunlan Ji, Tao Xin, Dawei Lu, and Jun Li. Experimental observation of equilibrium and dynamical quantum phase transitions via out-of-time-ordered correlators. *Phys. Rev. Lett.*, 124:250601, Jun 2020.

[197] Manoj K. Joshi, Andreas Elben, Benoît Vermersch, Tiff Brydges, Christine Maier, Peter Zoller, Rainer Blatt, and Christian F. Roos. Quantum information scrambling in a trapped-ion quantum simulator with tunable range interactions. *Phys. Rev. Lett.*, 124:240505, Jun 2020.

[198] Lorenzo Leone, Salvatore F. E. Oliviero, and Alioscia Hamma. Stabilizer rényi entropy. *Phys. Rev. Lett.*, 128:050402, Feb 2022.

[199] Brian Swingle, Gregory Bentsen, Monika Schleier-Smith, and Patrick Hayden. Measuring the scrambling of quantum information. *Phys. Rev. A*, 94:040302, Oct 2016.

[200] Markus Heyl, Frank Pollmann, and Balázs Dóra. Detecting equilibrium and dynamical quantum phase transitions in ising chains via out-of-time-ordered correlators. *Phys. Rev. Lett.*, 121:016801, Jul 2018.

[201] Ceren B. Dağ, Kai Sun, and L.-M. Duan. Detection of quantum phases via out-of-time-order correlators. *Phys. Rev. Lett.*, 123:140602, Oct 2019.

[202] Nitesh Jaiswal, Mamta Gautam, Ankit Gill, and Tapobrata Sarkar. Fotoc complexity in the lipkin–meshkov–glick model and its variant. *The European Physical Journal B*, 97(1):5, 2024.

[203] R. J. Lewis-Swan, S. R. Muleady, and A. M. Rey. Detecting out-of-time-order correlations via quasiadiabatic echoes as a tool to reveal quantum coherence in equilibrium quantum phase transitions. *Phys. Rev. Lett.*, 125:240605, Dec 2020.

[204] Zheng-Hang Sun, Jia-Qi Cai, Qi-Cheng Tang, Yong Hu, and Heng Fan. Out-of-time-order correlators and quantum phase transitions in the rabi and dicke models. *Annalen der Physik*, 532(4):1900270, 2020.

[205] Qian Bin, Liang-Liang Wan, Franco Nori, Ying Wu, and Xin-You Lü. Out-of-time-order correlation as a witness for topological phase transitions. *Phys. Rev. B*, 107:L020202, Jan 2023.

[206] Kanato Goto, Taozhi Guo, Tomoki Nosaka, Masahiro Nozaki, Shinsei Ryu, and Kotaro Tamaoka. Spatial deformation of many-body quantum chaotic systems and quantum information scrambling. *Phys. Rev. B*, 109:054301, Feb 2024.

[207] Varadharajan Muruganandam, Manas Sajjan, and Sabre Kais. Defect-induced localization of information scrambling in 1d kitaev model. *Physica Scripta*, 99(10):105123, sep 2024.

[208] Arash Ahmadi and Eliska Greplova. Quantifying non-stabilizerness via information scrambling. *SciPost Physics*, 16(2), February 2024.

[209] Debabrata Mondal, Sudip Sinha, and S. Sinha. Chaos and quantum scars in a coupled top model. *Phys. Rev. E*, 102:020101, Aug 2020.

[210] Martyna Sedlmayr, Hadi Cheraghi, and Nicholas Sedlmayr. Information trapping by topologically protected edge states: Scrambling and the butterfly velocity. *Phys. Rev. B*, 108:184303, Nov 2023.

[211] Namit Anand and Paolo Zanardi. Brotocs and quantum information scrambling at finite temperature. *Quantum*, 6:746, June 2022.

[212] Sudip Sinha, Sayak Ray, and Subhasis Sinha. Fingerprint of chaos and quantum scars in kicked dicke model: an out-of-time-order correlator study. *Journal of Physics: Condensed Matter*, 33(17):174005, apr 2021.

[213] W. Kirkby, D. H. J. O'Dell, and J. Mumford. False signals of chaos from quantum probes. *Phys. Rev. A*, 104:043308, Oct 2021.

[214] Liang-Jun Zhai and Shuai Yin. Out-of-time-ordered correlator in non-hermitian quantum systems. *Phys. Rev. B*, 102:054303, Aug 2020.

[215] Qian Wang and Francisco Pérez-Bernal. Probing an excited-state quantum phase transition in a quantum many-body system via an out-of-time-order correlator. *Phys. Rev. A*, 100:062113, Dec 2019.

[216] Rohit Kumar Shukla, Gautam Kamalakar Naik, and Sunil Kumar Mishra. Out-of-time-order correlation and detection of phase structure in floquet transverse ising spin system. *Europhysics Letters*, 132(4):47003, jan 2021.

[217] Kate Scholberg. Supernova neutrino detection. *Annual Review of Nuclear and Particle Science*, 62(1):81–103, November 2012.

[218] Nicole Yunger Halpern. Jarzynski-like equality for the out-of-time-ordered correlator. *Phys. Rev. A*, 95:012120, Jan 2017.

[219] Nicole Yunger Halpern. Jarzynski-like equality for the out-of-time-ordered correlator. *Physical Review A*, 95(1), January 2017.

[220] Nicole Yunger Halpern, Brian Swingle, and Justin Dressel. Quasiprobability behind the out-of-time-ordered correlator. *Phys. Rev. A*, 97:042105, Apr 2018.

[221] Stefano Gherardini and Gabriele De Chiara. Quasiprobabilities in quantum thermodynamics and many-body systems. *PRX Quantum*, 5:030201, Sep 2024.

[222] Xinhua Peng, Hui Zhou, Bo-Bo Wei, Jiangyu Cui, Jiangfeng Du, and Ren-Bao Liu. Experimental observation of lee-yang zeros. *Phys. Rev. Lett.*, 114:010601, Jan 2015.

[223] Francesco Turro, Ivan A. Chernyshev, Ramya Bhaskar, and Marc Illa. Qutrit and qubit circuits for three-flavor collective neutrino oscillations. *Phys. Rev. D*, 111:043038, Feb 2025.

[224] Daniel Gottesman. Fault tolerant quantum computation with higher dimensional systems. *Chaos Solitons Fractals*, 10:1749–1758, 1999.

[225] Anthony Ciavarella, Natalie Klco, and Martin J. Savage. Trailhead for quantum simulation of SU(3) Yang-Mills lattice gauge theory in the local multiplet basis. *Phys. Rev. D*, 103(9):094501, 2021.

[226] Erik J. Gustafson. Prospects for simulating a qudit-based model of $(1 + 1)$D scalar qed. *Phys. Rev. D*, 103:114505, Jun 2021.

[227] Manuel Calixto, Alberto Mayorgas, and Julio Guerrero. Entanglement and U(D)-spin squeezing in symmetric multi-quDit systems and applications to quantum phase transitions in Lipkin–Meshkov–Glick D-level atom models. *Quantum Inf. Process.*, 20:304, 2021.

[228] Erik Gustafson. Noise Improvements in Quantum Simulations of sQED using Qutrits, 1 2022.

[229] Daniel González-Cuadra, Torsten V. Zache, Jose Carrasco, Barbara Kraus, and Peter Zoller. Hardware Efficient Quantum Simulation of Non-Abelian Gauge Theories with Qudits on Rydberg Platforms. *Phys. Rev. Lett.*, 129(16):160501, 2022.

[230] Erik J. Gustafson, Henry Lamm, Felicity Lovelace, and Damian Musk. Primitive quantum gates for an SU(2) discrete subgroup: Binary tetrahedral. *Phys. Rev. D*, 106(11):114501, 2022.

[231] Erik J. Gustafson and Henry Lamm. Robustness of Gauge Digitization to Quantum Noise, 1 2023.

[232] Torsten V. Zache, Daniel González-Cuadra, and Peter Zoller. Fermion-qudit quantum processors for simulating lattice gauge theories with matter. *Quantum*, 7:1140, 2023.

[233] Marc Illa, Caroline E. P. Robin, and Martin J. Savage. Quantum simulations of SO(5) many-fermion systems using qudits. *Phys. Rev. C*, 108(6):064306, 2023.

[234] Pavel P. Popov, Michael Meth, Maciej Lewenstein, Philipp Hauke, Martin Ringbauer, Erez Zohar, and Valentin Kasper. Variational quantum simulation of U(1) lattice gauge theories with qudit systems. *Phys. Rev. Res.*, 6(1):013202, 2024.

[235] Michael Meth et al. Simulating 2D lattice gauge theories on a qudit quantum computer, 10 2023.

[236] Giuseppe Calajò, Giuseppe Magnifico, Claire Edmunds, Martin Ringbauer, Simone Montangero, and Pietro Silvi. Digital quantum simulation of a (1+1)D SU(2) lattice gauge theory with ion qudits, 2 2024.

[237] Marcela Carena, Henry Lamm, Ying-Ying Li, and Wanqiang Liu. Quantum error thresholds for gauge-redundant digitizations of lattice field theories, 2 2024.

[238] Marc Illa, Caroline E. P. Robin, and Martin J. Savage. Qu8its for Quantum Simulations of Lattice Quantum Chromodynamics, 3 2024.

[239] Erik J. Gustafson, Yao Ji, Henry Lamm, Edison M. Murairi, and Shuchen Zhu. Primitive Quantum Gates for an SU(3) Discrete Subgroup: $\Sigma(36 \times 3)$, 4 2024.

[240] Pei Jiang Low, Brendan M. White, Andrew A. Cox, Matthew L. Day, and Crystal Senko. Practical trapped-ion protocols for universal qudit-based quantum computing. *Phys. Rev. Res.*, 2:033128, Jul 2020.

[241] Martin Ringbauer, Michael Meth, Lukas Postler, Roman Stricker, Rainer Blatt, Philipp Schindler, and Thomas Monz. A universal qudit quantum processor with trapped ions. *Nature Phys.*, 18(9):1053–1057, 2022.

[242] Pei Jiang Low, Brendan White, and Crystal Senko. Control and Readout of a 13-level Trapped Ion Qudit, 6 2023.

[243] Ilia V. Zalivako et al. Towards multiqudit quantum processor based on a $^{171}Yb^{+}$ ion string: Realizing basic quantum algorithms, 2 2024.

[244] Anastasiia S. Nikolaeva et al. Scalable improvement of the generalized Toffoli gate realization using trapped-ion-based qutrits, 7 2024.

[245] M. S. Blok, V. V. Ramasesh, T. Schuster, K. O'Brien, J. M. Kreikebaum, D. Dahlen, A. Morvan, B. Yoshida, N. Y. Yao, and I. Siddiqi. Quantum information scrambling on a superconducting qutrit processor. *Phys. Rev. X*, 11(2):021010, 2021.

[246] Lennart Maximilian Seifert, Ziqian Li, Tanay Roy, David I. Schuster, Frederic T. Chong, and Jonathan M. Baker. Exploring ququart computation on a transmon using optimal control. *Phys. Rev. A*, 108(6):062609, 2023.

[247] Long B. Nguyen, Noah Goss, Karthik Siva, Yosep Kim, Younis, Bingcheng Qing, Akel Hashim, David I. Santiago, and Irfan Siddiqi. Empowering high-dimensional quantum computing by traversing the dual bosonic ladder, 12 2023.

[248] Elizabeth Champion, Zihao Wang, Rayleigh Parker, and Machiel Blok. Multifrequency control and measurement of a spin-7/2 system encoded in a transmon qudit, 5 2024.

[249] Tanay Roy, Taeyoon Kim, Alexander Romanenko, and Anna Grassellino. Qudit-based quantum computing with SRF cavities at Fermilab. *PoS*, LATTICE2023:127, 2024.

[250] Yulin Chi et al. A programmable qudit-based quantum processor. *Nat. Commun.*, 13:1166, March 2022.

[251] Nicolas J. Cerf, Mohamed Bourennane, Anders Karlsson, and Nicolas Gisin. Security of Quantum Key Distribution Using d-Level Systems. *Phys. Rev. Lett.*, 88(12):127902, March 2002.

[252] Z. Gedik, I. A. Silva, B. Çakmak, G. Karpat, E. L. G. Vidoto, D. O. Soares-Pinto, E. R. Deazevedo, and F. F. Fanchini. Computational speed-up with a single qudit. *Sci. Rep.*, 5:14671, October 2015.

[253] Pranav Gokhale, Jonathan M Baker, Casey Duckering, Natalie C Brown, Kenneth R Brown, and Frederic T Chong. Asymptotic improvements to quantum circuits via qutrits. In *Proceedings of the 46th International Symposium on Computer Architecture*, pages 554–566, 2019.

[254] Jonathan M. Baker, Casey Duckering, and Frederic T. Chong. Efficient quantum circuit decompositions via intermediate qudits. In *2020 IEEE 50th International Symposium on Multiple-Valued Logic (ISMVL)*, pages 303–308, 2020.

[255] Sumin Lim, Junjie Liu, and Arzhang Ardavan. Fault-tolerant qubit encoding using a spin-7/2 qudit. *Phys. Rev. A*, 108(6):062403, 2023.

[256] Yuchen Wang, Zixuan Hu, Barry C. Sanders, and Sabre Kais. Qudits and high-dimensional quantum computing. *Front. Phys.*, 8:479, November 2020.

[257] M. A. Yurtalan, J. Shi, M. Kononenko, A. Lupascu, and S. Ashhab. Implementation of a Walsh-Hadamard Gate in a Superconducting Qutrit. *Phys. Rev. Lett.*, 125(18):180504, October 2020.

[258] A. Morvan, V. V. Ramasesh, M. S. Blok, J. M. Kreikebaum, K. O'Brien, L. Chen, B. K. Mitchell, R. K. Naik, D. I. Santiago, and I. Siddiqi. Qutrit randomized benchmarking. *Phys. Rev. Lett.*, 126:210504, May 2021.

[259] Alba Cervera-Lierta, Mario Krenn, Alán Aspuru-Guzik, and Alexey Galda. Experimental high-dimensional Greenberger-Horne-Zeilinger entanglement with superconducting transmon qutrits. *Phys. Rev. Applied*, 17:024062, 2022.

[260] Pavel Hrmo, Benjamin Wilhelm, Lukas Gerster, Martin W. van Mourik, Marcus Huber, Rainer Blatt, Philipp Schindler, Thomas Monz, and Martin Ringbauer. Native qudit entanglement in a trapped ion quantum processor. *Nature Commun.*, 14(1):2242, 2023.

[261] Noah Goss et al. High-fidelity qutrit entangling gates for superconducting circuits. *Nature Commun.*, 13(1):7481, 2022. [Erratum: Nature Commun. 14, 4256 (2023)].

[262] Mahadevan Subramanian and Adrian Lupascu. Efficient two-qutrit gates in superconducting circuits using parametric coupling. *Phys. Rev. A*, 108(6):062616, 2023.

[263] James Pantaleone. Dirac neutrinos in dense matter. *Phys. Rev. D*, 46:510–523, Jul 1992.

[264] James T. Pantaleone. Neutrino oscillations at high densities. *Phys. Lett. B*, 287:128–132, 1992.

[265] Yong Zhong Qian and George M. Fuller. Neutrino-neutrino scattering and matter enhanced neutrino flavor transformation in Supernovae. *Phys. Rev. D*, 51:1479–1494, 1995.

[266] Sergio Pastor and Georg Raffelt. Flavor oscillations in the supernova hot bubble region: Nonlinear effects of neutrino background. *Phys. Rev. Lett.*, 89:191101, 2002.

[267] Alessandro Mirizzi, Irene Tamborra, Hans-Thomas Janka, Ninetta Saviano, Kate Scholberg, Robert Bollig, Lorenz Hudepohl, and Sovan Chakraborty. Supernova Neutrinos: Production, Oscillations and Detection. *Riv. Nuovo Cim.*, 39(1-2):1–112, 2016.

[268] A. Malkus, J. P. Kneller, G. C. McLaughlin, and R. Surman. Neutrino oscillations above black hole accretion disks: disks with electron-flavor emission. *Phys. Rev. D*, 86:085015, 2012.

[269] A. Malkus, G. C. McLaughlin, and R. Surman. Symmetric and Standard Matter-Neutrino Resonances Above Merging Compact Objects. *Phys. Rev. D*, 93(4):045021, 2016.

[270] Yong-Lin Zhu, Albino Perego, and Gail C. McLaughlin. Matter Neutrino Resonance Transitions above a Neutron Star Merger Remnant. *Phys. Rev. D*, 94(10):105006, 2016.

[271] Maik Frensel, Meng-Ru Wu, Cristina Volpe, and Albino Perego. Neutrino Flavor Evolution in Binary Neutron Star Merger Remnants. *Phys. Rev. D*, 95(2):023011, 2017.

[272] Amélie Chatelain and Cristina Volpe. Helicity coherence in binary neutron star mergers and non-linear feedback. *Phys. Rev. D*, 95(4):043005, 2017.

[273] Meng-Ru Wu and Irene Tamborra. Fast neutrino conversions: Ubiquitous in compact binary merger remnants. *Phys. Rev. D*, 95(10):103007, 2017.

[274] James Y. Tian, Amol V. Patwardhan, and George M. Fuller. Neutrino Flavor Evolution in Neutron Star Mergers. *Phys. Rev. D*, 96(4):043001, 2017.

[275] Henry Purcell, Sherwood Richers, Amol V. Patwardhan, and Francois Foucart. Three-flavor, Full Momentum Space Neutrino Spin Oscillations in Neutron Star Mergers, 4 2024.

[276] G. M. Fuller and B. S. Meyer. Neutrino capture and supernova nucleosynthesis. *Astrophys. J.*, 453:792–809, 1995.

[277] A. B. Balantekin and H. Yuksel. Neutrino mixing and nucleosynthesis in core-collapse supernovae. *New J. Phys.*, 7:51, 2005.

[278] Huaiyu Duan, Alexander Friedland, GailC. McLaughlin, and Rebecca Surman. The influence of collective neutrino oscillations on a supernova r-process. *J. Phys. G*, 38:035201, 2011.

[279] Zewei Xiong, Andre Sieverding, Manibrata Sen, and Yong-Zhong Qian. Potential Impact of Fast Flavor Oscillations on Neutrino-driven Winds and Their Nucleosynthesis. *Astrophys. J.*, 900(2):144, 2020.

[280] A. Baha Balantekin, Michael J. Cervia, Amol V. Patwardhan, Rebecca Surman, and Xilu Wang. Collective Neutrino Oscillations and Heavy-element Nucleosynthesis in Supernovae: Exploring Potential Effects of Many-body Neutrino Correlations. *Astrophys. J.*, 967(2):146, 2024.

[281] Huaiyu Duan and James P Kneller. Neutrino flavour transformation in supernovae. *J. Phys. G*, 36:113201, 2009.

[282] Huaiyu Duan, George M. Fuller, and Yong-Zhong Qian. Collective Neutrino Oscillations. *Ann. Rev. Nucl. Part. Sci.*, 60:569–594, 2010.

[283] Irene Tamborra and Shashank Shalgar. New Developments in Flavor Evolution of a Dense Neutrino Gas. *Ann. Rev. Nucl. Part. Sci.*, 71:165–188, 2021.

[284] Francesco Capozzi and Ninetta Saviano. Neutrino Flavor Conversions in High-Density Astrophysical and Cosmological Environments. *Universe*, 8(2):94, 2022.

[285] Sherwood Richers and Manibrata Sen. *Fast Flavor Transformations*, pages 1–17. Springer Nature Singapore, Singapore, 2022.

[286] Amol V. Patwardhan, Michael J. Cervia, Ermal Rrapaj, Pooja Siwach, and A. B. Balantekin. *Many-Body Collective Neutrino Oscillations: Recent Developments*, pages 1–16. Springer Nature Singapore, Singapore, 2023.

[287] M. Cristina Volpe. Neutrinos from dense environments: Flavor mechanisms, theoretical approaches, observations, and new directions. *Rev. Mod. Phys.*, 96(2):025004, 2024.

[288] A. B. Balantekin, Michael J. Cervia, Amol V. Patwardhan, Ermal Rrapaj, and Pooja Siwach. Quantum information and quantum simulation of neutrino physics. *Eur. Phys. J. A*, 59(8):186, 2023.

[289] Stuart Samuel. Neutrino oscillations in dense neutrino gases. *Phys. Rev. D*, 48:1462–1477, 1993.

[290] V. Alan Kostelecky, James T. Pantaleone, and Stuart Samuel. Neutrino oscillation in the early universe. *Phys. Lett. B*, 315:46–50, 1993.

[291] V. Alan Kostelecky and Stuart Samuel. Neutrino oscillations in the early universe with an inverted neutrino mass hierarchy. *Phys. Lett. B*, 318:127–133, 1993.

[292] V. Alan Kostelecky and Stuart Samuel. Nonlinear neutrino oscillations in the expanding universe. *Phys. Rev. D*, 49:1740–1757, 1994.

[293] V. Alan Kostelecky and Stuart Samuel. Neutrino oscillations in the early universe with nonequilibrium neutrino distributions. *Phys. Rev. D*, 52:3184–3201, 1995.

[294] L. Wolfenstein. Neutrino oscillations in matter. *Phys. Rev. D*, 17:2369–2374, May 1978.

[295] L. Wolfenstein. Neutrino oscillations and stellar collapse. *Phys. Rev. D*, 20:2634–2635, Nov 1979.

[296] S. P. Mikheyev and A. Yu. Smirnov. Resonant amplification of neutrino oscillations in matter and solar neutrino spectroscopy. *Nuovo Cim. C*, 9:17–26, 1986.

[297] S. P. Mikheyev and A. Yu. Smirnov. Resonant neutrino oscillations in matter. *Prog. Part. Nucl. Phys.*, 23:41–136, 1989.

[298] G. M. Fuller, R. W. Mayle, J. R. Wilson, and D. N. Schramm. Resonant Neutrino Oscillations and Stellar Collapse. , 322:795, November 1987.

[299] Dirk Notzold and Georg Raffelt. Neutrino dispersion at finite temperature and density. *Nucl. Phys. B*, 307:924–936, 1988.

[300] Martin J. Savage, Robert A. Malaney, and George M. Fuller. Neutrino Oscillations and the Leptonic Charge of the Universe. *Astrophys. J.*, 368:1–11, 1991.

[301] G. Sigl and G. Raffelt. General kinetic description of relativistic mixed neutrinos. *Nuclear Physics B*, 406(1):423–451, September 1993.

[302] Stuart Samuel. Bimodal coherence in dense selfinteracting neutrino gases. *Phys. Rev. D*, 53:5382–5393, 1996.

[303] R. D. Hoffman, S. E. Woosley, and Y. Z. Qian. Nucleosynthesis in neutrino driven winds: 2. Implications for heavy element synthesis. *Astrophys. J.*, 482:951, 1997.

[304] A. B. Balantekin and Y. Pehlivan. Neutrino-Neutrino Interactions and Flavor Mixing in Dense Matter. *J. Phys. G*, 34:47–66, 2007.

[305] Basudeb Dasgupta and Manibrata Sen. Fast Neutrino Flavor Conversion as Oscillations in a Quartic Potential. *Phys. Rev. D*, 97(2):023017, 2018.

[306] Damiano F. G. Fiorillo, Georg G. Raffelt, and Günter Sigl. Collective neutrino-antineutrino oscillations in dense neutrino environments? *Phys. Rev. D*, 109(4):043031, 2024.

[307] Vincenzo Cirigliano, Srimoyee Sen, and Yukari Yamauchi. Neutrino many-body flavor evolution: the full Hamiltonian, 4 2024.

[308] Huaiyu Duan, George M. Fuller, J. Carlson, and Yong-Zhong Qian. Coherent Development of Neutrino Flavor in the Supernova Environment. *Phys. Rev. Lett.*, 97:241101, 2006.

[309] Huaiyu Duan, George M. Fuller, J Carlson, and Yong-Zhong Qian. Simulation of Coherent Non-Linear Neutrino Flavor Transformation in the Supernova Environment. 1. Correlated Neutrino Trajectories. *Phys. Rev. D*, 74:105014, 2006.

[310] Ignacio Izaguirre, Georg Raffelt, and Irene Tamborra. Fast Pairwise Conversion of Supernova Neutrinos: A Dispersion-Relation Approach. *Phys. Rev. Lett.*, 118(2):021101, 2017.

[311] Francesco Capozzi, Madhurima Chakraborty, Sovan Chakraborty, and Manibrata Sen. Fast flavor conversions in supernovae: the rise of mu-tau neutrinos. *Phys. Rev. Lett.*, 125:251801, 2020.

[312] Damiano F. G. Fiorillo and Georg G. Raffelt. Slow and fast collective neutrino oscillations: Invariants and reciprocity. *Phys. Rev. D*, 107(4):043024, 2023.

[313] Damiano F. G. Fiorillo and Georg G. Raffelt. Flavor solitons in dense neutrino gases. *Phys. Rev. D*, 107(12):123024, 2023.

[314] Damiano F. G. Fiorillo, Georg G. Raffelt, and Günter Sigl. Inhomogeneous Kinetic Equation for Mixed Neutrinos: Tracing the Missing Energy. *Phys. Rev. Lett.*, 133(2):021002, 2024.

[315] Alessandro Roggero. Entanglement and many-body effects in collective neutrino oscillations. *Phys. Rev. D*, 104:103016, Nov 2021.

[316] Zewei Xiong. Many-body effects of collective neutrino oscillations. *Phys. Rev. D*, 105(10):103002, 2022.

[317] Alessandro Roggero, Ermal Rrapaj, and Zewei Xiong. Entanglement and correlations in fast collective neutrino flavor oscillations. *Phys. Rev. D*, 106(4):043022, 2022.

[318] Anson Kost, Lucas Johns, and Huaiyu Duan. Once-in-a-lifetime encounter models for neutrino media: From coherent oscillations to flavor equilibration. *Phys. Rev. D*, 109(10):103037, 2024.

[319] Benjamin Hall, Alessandro Roggero, Alessandro Baroni, and Joseph Carlson. Simulation of collective neutrino oscillations on a quantum computer. *Phys. Rev. D*, 104(6):063009, 2021.

[320] Kübra Yeter-Aydeniz, Shikha Bangar, George Siopsis, and Raphael C. Pooser. Collective neutrino oscillations on a quantum computer. *Quantum Inf. Process*, 21(3):84, 2022.

[321] Marc Illa and Martin J. Savage. Basic elements for simulations of standard-model physics with quantum annealers: Multigrid and clock states. *Phys. Rev. A*, 106(5):052605, 2022.

[322] Valentina Amitrano, Alessandro Roggero, Piero Luchi, Francesco Turro, Luca Vespucci, and Francesco Pederiva. Trapped-ion quantum simulation of collective neutrino oscillations. *Phys. Rev. D*, 107(2):023007, 2023.

[323] Marc Illa and Martin J. Savage. Multi-Neutrino Entanglement and Correlations in Dense Neutrino Systems. *Phys. Rev. Lett.*, 130(22):221003, 2023.

[324] Pooja Siwach, Kaytlin Harrison, and A. Baha Balantekin. Collective neutrino oscillations on a quantum computer with hybrid quantum-classical algorithm. *Phys. Rev. D*, 108(8):083039, 2023.

[325] Richard P. Feynman. Simulating physics with computers. *Int. J. Theor. Phys.*, 21:467–488, 1982.

[326] Ermal Rrapaj. Exact solution of multiangle quantum many-body collective neutrino-flavor oscillations. *Phys. Rev. C*, 101(6):065805, 2020.

[327] Amol V. Patwardhan, Michael J. Cervia, and A. Baha Balantekin. Eigenvalues and eigenstates of the many-body collective neutrino oscillation problem. *Phys. Rev. D*, 99:123013, Jun 2019.

[328] Amol V. Patwardhan, Michael J. Cervia, and A. B. Balantekin. Spectral splits and entanglement entropy in collective neutrino oscillations. *Phys. Rev. D*, 104(12):123035, 2021.

[329] Duff Neill, Hanqing Liu, Joshua Martin, and Alessandro Roggero. Scattering Neutrinos, Spin Models, and Permutations, 6 2024.

[330] Pooja Siwach, Anna M. Suliga, and A. Baha Balantekin. Entanglement in three-flavor collective neutrino oscillations. *Phys. Rev. D*, 107(2):023019, 2023.

[331] Ivan A. Chernyshev. Three-flavor Collective Neutrino Oscillations on D-Wave's Advantage Quantum Annealer, 2024.

[332] IBM Quantum, 2021.

[333] Y. Pehlivan, A. B. Balantekin, Toshitaka Kajino, and Takashi Yoshida. Invariants of Collective Neutrino Oscillations. *Phys. Rev. D*, 84:065008, 2011.

[334] Michael J. Cervia, Pooja Siwach, Amol V. Patwardhan, A. B. Balantekin, S. N. Coppersmith, and Calvin W. Johnson. Collective neutrino oscillations with tensor networks using a time-dependent variational principle. *Phys. Rev. D*, 105(12):123025, 2022.

[335] P. F. de Salas, D. V. Forero, S. Gariazzo, P. Martínez-Miravé, O. Mena, C. A. Ternes, M. Tórtola, and J. W. F. Valle. 2020 global reassessment of the neutrino oscillation picture. *JHEP*, 02:071, 2021.

[336] Francesco Capozzi, Eleonora Di Valentino, Eligio Lisi, Antonio Marrone, Alessandro Melchiorri, and Antonio Palazzo. Unfinished fabric of the three neutrino paradigm. *Phys. Rev. D*, 104(8):083031, 2021.

[337] Ha C. Nguyen, Bao G. Bach, Tien D. Nguyen, Duc M. Tran, Duy V. Nguyen, and Hung Q. Nguyen. Simulating neutrino oscillations on a superconducting qutrit. *Phys. Rev. D*, 108(2):023013, 2023.

[338] Ian D. Kivlichan, Jarrod McClean, Nathan Wiebe, Craig Gidney, Alán Aspuru-Guzik, Garnet Kin-Lic Chan, and Ryan Babbush. Quantum simulation of electronic structure with linear depth and connectivity. *Phys. Rev. Lett.*, 120:110501, Mar 2018.

[339] Bryan O'Gorman, William J. Huggins, Eleanor G. Rieffel, and K. Birgitta Whaley. Generalized swap networks for near-term quantum computing, 5 2019.

[340] Masuo Suzuki. Fractal decomposition of exponential operators with applications to many-body theories and Monte Carlo simulations. *Phys. Lett. A*, 146(6):319–323, June 1990.

[341] Masuo Suzuki. General theory of fractal path integrals with applications to many-body theories and statistical physics. *J. Math. Phys.*, 32(2):400–407, February 1991.

[342] C. A. Argüelles and B. J. P. Jones. Neutrino Oscillations in a Quantum Processor. *Phys. Rev. Research.*, 1:033176, 2019.

[343] Farrokh Vatan and Colin Williams. Optimal quantum circuits for general two-qubit gates. *Phys. Rev. A*, 69(3):032315, March 2004.

[344] G. Vidal and C. M. Dawson. Universal quantum circuit for two-qubit transformations with three controlled-not gates. *Phys. Rev. A*, 69:010301, Jan 2004.

[345] Mark W. Coffey, Ron Deiotte, and Torey Semi. Comment on "Universal quantum circuit for two-qubit transformations with three controlled-NOT gates" and "Recognizing small-circuit structure in two-qubit operators". *Phys. Rev. A*, 77:066301, Jun 2008.

[346] M. J. Molewski and B. J. P. Jones. Scalable qubit representations of neutrino mixing matrices. *Phys. Rev. D*, 105(5):056024, 2022.

[347] Qiskit contributors. Qiskit 1.0.2: An open-source framework for quantum computing, 2024.

[348] Ali Javadi-Abhari et al. Quantum computing with Qiskit, 5 2024.

[349] Seyon Sivarajah, Silas Dilkes, Alexander Cowtan, Will Simmons, Alec Edgington, and Ross Duncan. t|ket⟩: a retargetable compiler for NISQ devices. *Quantum Sci. Technol.*, 6(1):014003, 2020.

[350] V.V. Shende, S.S. Bullock, and I.L. Markov. Synthesis of quantum-logic circuits. *IEEE Trans. on Computer-Aided Design*, 25(6):1000–1010, 2006.

[351] M. Mottonen and J. J. Vartiainen. Decompositions of general quantum gates. In Susan Shannon, editor, *Trends in Quantum Computing Research*, chapter 7. NOVA Science Publishers, Inc., USA, 2006.

[352] Maximilian Balthasar Mansky, Santiago Londoño Castillo, Victor Ramos Puigvert, and Claudia Linnhoff-Popien. Near-optimal quantum circuit construction via Cartan decomposition. *Phys. Rev. A*, 108(5):052607, 2023.

[353] Anna M. Krol and Zaid Al-Ars. Beyond Quantum Shannon: Circuit Construction for General n-Qubit Gates Based on Block ZXZ-Decomposition, 3 2024.

[354] John Preskill. Quantum Computing in the NISQ era and beyond. *Quantum*, 2:79, 2018.

[355] Ying Li and Simon C. Benjamin. Efficient Variational Quantum Simulator Incorporating Active Error Minimization. *Phys. Rev. X*, 7(2):021050, 2017.

[356] Kristan Temme, Sergey Bravyi, and Jay M. Gambetta. Error Mitigation for Short-Depth Quantum Circuits. *Phys. Rev. Lett.*, 119(18):180509, 2017.

[357] Tudor Giurgica-Tiron, Yousef Hindy, Ryan LaRose, Andrea Mari, and William J. Zeng. Digital zero noise extrapolation for quantum error mitigation. In *2020 IEEE International Conference on Quantum Computing and Engineering (QCE)*, pages 306–316, 2020.

[358] Ewout van den Berg, Zlatko K. Minev, Abhinav Kandala, and Kristan Temme. Probabilistic error cancellation with sparse Pauli–Lindblad models on noisy quantum processors. *Nat. Phys.*, 19(8):1116–1121, 2023.

[359] Miroslav Urbanek, Benjamin Nachman, Vincent R. Pascuzzi, Andre He, Christian W. Bauer, and Wibe A. de Jong. Mitigating depolarizing noise on quantum computers with noise-estimation circuits. *Phys. Rev. Lett.*, 127:270502, Dec 2021.

[360] Sarmed A Rahman, Randy Lewis, Emanuele Mendicelli, and Sarah Powell. Self-mitigating trotter circuits for su(2) lattice gauge theory on a quantum computer. *Phys. Rev. D*, 106:074502, Oct 2022.

[361] Roland C. Farrell, Ivan A. Chernyshev, Sarah J. M. Powell, Nikita A. Zemlevskiy, Marc Illa, and Martin J. Savage. Preparations for quantum simulations of quantum chromodynamics in 1+1 dimensions. I. Axial gauge. *Phys. Rev. D*, 107(5):054512, 2023.

[362] Anthony N. Ciavarella. Quantum simulation of lattice QCD with improved Hamiltonians. *Phys. Rev. D*, 108(9):094513, 2023.

[363] Roland C. Farrell, Marc Illa, Anthony N. Ciavarella, and Martin J. Savage. Scalable Circuits for Preparing Ground States on Digital Quantum Computers: The Schwinger Model Vacuum on 100 Qubits. *PRX Quantum*, 5(2):020315, 2024.

[364] Roland C. Farrell, Marc Illa, Anthony N. Ciavarella, and Martin J. Savage. Quantum simulations of hadron dynamics in the Schwinger model using 112 qubits. *Phys. Rev. D*, 109(11):114510, 2024.

[365] Anthony N. Ciavarella and Christian W. Bauer. Quantum Simulation of SU(3) Lattice Yang Mills Theory at Leading Order in Large N, 2 2024.

[366] Nhung H. Nguyen, Minh C. Tran, Yingyue Zhu, Alaina M. Green, C. Huerta Alderete, Zohreh Davoudi, and Norbert M. Linke. Digital Quantum Simulation of the Schwinger Model and Symmetry Protection with Trapped Ions. *PRX Quantum*, 3(2):020324, 2022.

[367] Joel J. Wallman and Joseph Emerson. Noise tailoring for scalable quantum computation via randomized compiling. *Phys. Rev. A*, 94(5):052325, 2016.

[368] Akel Hashim et al. Randomized Compiling for Scalable Quantum Computing on a Noisy Superconducting Quantum Processor. *Phys. Rev. X*, 11(4):041039, 2021.

[369] Lorenza Viola and Seth Lloyd. Dynamical suppression of decoherence in two-state quantum systems. *Phys. Rev. A*, 58:2733–2744, Oct 1998.

[370] A. M. Souza, G. A. Álvarez, and D. Suter. Robust dynamical decoupling. *Phil. Trans. R. Soc.*, 370(1976):4748–4769, October 2012.

[371] Nic Ezzell, Bibek Pokharel, Lina Tewala, Gregory Quiroz, and Daniel A. Lidar. Dynamical decoupling for superconducting qubits: A performance survey. *Phys. Rev. Applied*, 20(6):064027, 2023.

[372] Paul D. Nation, Hwajung Kang, Neereja Sundaresan, and Jay M. Gambetta. Scalable Mitigation of Measurement Errors on Quantum Computers. *PRX Quantum*, 2(4):040326, 2021.

[373] Natalie Klco and Martin J. Savage. Minimally entangled state preparation of localized wave functions on quantum computers. *Phys. Rev. A*, 102(1):012612, 2020.

[374] John A. Smolin, Jay M. Gambetta, and Graeme Smith. Efficient method for computing the maximum-likelihood quantum state from measurements with additive gaussian noise. *Phys. Rev. Lett.*, 108:070502, Feb 2012.

[375] Hsin-Yuan Huang, Richard Kueng, and John Preskill. Predicting many properties of a quantum system from very few measurements. *Nature Phys.*, 16(10):1050–1057, 2020.

[376] Atithi Acharya, Siddhartha Saha, and Anirvan M. Sengupta. Shadow tomography based on informationally complete positive operator-valued measure. *Phys. Rev. A*, 104:052418, Nov 2021.

[377] Mario Motta, Chong Sun, Adrian Teck Keng Tan, Matthew J. O' Rourke, Erika Ye, Austin J. Minnich, Fernando G. S. L. Brandão, and Garnet Kin-Lic Chan. Determining eigenstates and thermal states on a quantum computer using quantum imaginary time evolution. *Nature Phys.*, 16:205–210, 2019.

[378] R. Sagastizabal, S. P. Premaratne, B. A. Klaver, M. A. Rol, V. Negîrneac, M. S. Moreira, X. Zou, S. Johri, N. Muthusubramanian, M. Beekman, C. Zachariadis, V. P. Ostroukh, N. Haider, A. Bruno, A. Y. Matsuura, and L. DiCarlo. Variational preparation of finite-temperature states on a quantum computer. *npj Quantum Inf.*, 7:130, January 2021.

[379] Francesco Turro. Quantum imaginary time propagation algorithm for preparing thermal states, 2023.

[380] Zohreh Davoudi, Niklas Mueller, and Connor Powers. Towards Quantum Computing Phase Diagrams of Gauge Theories with Thermal Pure Quantum States. *Phys. Rev. Lett.*, 131(8):081901, 2023.

[381] Abhishek Rajput, Alessandro Roggero, and Nathan Wiebe. Hybridized Methods for Quantum Simulation in the Interaction Picture. *Quantum*, 6:780, 2022.

[382] Maolin Wang, Yu Pan, Zenglin Xu, Guangxi Li, Xiangli Yang, Danilo Mandic, and Andrzej Cichocki. Tensor networks meet neural networks: A survey and future perspectives, 2025.

[383] Y.-Y. Shi, L.-M. Duan, and G. Vidal. Classical simulation of quantum many-body systems with a tree tensor network. *Phys. Rev. A*, 74:022320, Aug 2006.

[384] L. Tagliacozzo, G. Evenbly, and G. Vidal. Simulation of two-dimensional quantum systems using a tree tensor network that exploits the entropic area law. *Phys. Rev. B*, 80:235127, Dec 2009.

[385] Wei Li, Jan von Delft, and Tao Xiang. Efficient simulation of infinite tree tensor network states on the bethe lattice. *Phys. Rev. B*, 86:195137, Nov 2012.

[386] Turban-D.H.P. Musser A.J. et al. Schröder, F.A.Y.N. Tensor network simulation of multi-environmental open quantum dynamics via machine learning and entanglement renormalisation. *Nature Communications*, 10(1062), 2019.

[387] Silas R. Beane, David B. Kaplan, Natalie Klco, and Martin J. Savage. Entanglement Suppression and Emergent Symmetries of Strong Interactions. *Phys. Rev. Lett.*, 122(10):102001, 2019.

[388] Xhek Turkeshi, Emanuele Tirrito, and Piotr Sierant. Magic spreading in random quantum circuits. *Nature Commun.*, 16(1):2575, 2025.

[389] Poetri Sonya Tarabunga and Emanuele Tirrito. Magic transition in measurement-only circuits. 7 2024.

[390] Caroline E. P. Robin and Martin J. Savage. The Magic in Nuclear and Hypernuclear Forces. 5 2024.

[391] Ivan Chernyshev, Caroline E. P. Robin, and Martin J. Savage. Quantum Magic and Computational Complexity in the Neutrino Sector. 11 2024.

[392] Natalie Klco, D. H. Beck, and Martin J. Savage. Entanglement structures in quantum field theories: Negativity cores and bound entanglement in the vacuum. *Phys. Rev. A*, 107(1):012415, 2023.

[393] Boyu Gao and Natalie Klco. Detecting spacelike vacuum entanglement at all distances and promoting negativity to a necessary and sufficient entanglement measure in many-body regimes. 10 2024.

[394] N. Chamel, S. Goriely, J. M. Pearson, and M. Onsi. Unified description of neutron superfluidity in the neutron-star crust with analogy to anisotropic multiband bcs superconductors. *Phys. Rev. C*, 81:045804, Apr 2010.

[395] Gordon Baym, Christopher Pethick, and David Pines. Superfluidity in neutron stars. *Nature*, 224:673–674, November 1969.

[396] Y. Pehlivan, A. L. Subaşı, N. Ghazanfari, S. Birol, and H. Yüksel. Spectral splits of neutrinos as a BCS-BEC crossover type phenomenon. *Phys. Rev. D*, 95(6):063022, 2017.

[397] S. Ramanan and M. Urban. Bec-bcs crossover in neutron matter with renormalization-group-based effective interactions. *Phys. Rev. C*, 88:054315, Nov 2013.

[398] Giancarlo Calvanese Strinati, Pierbiagio Pieri, Gerd Röpke, Peter Schuck, and Michael Urban. The BCS–BEC crossover: From ultra-cold Fermi gases to nuclear systems. *Phys. Rept.*, 738:1–76, 2018.

[399] Pedro R. Nicácio Falcão, Piotr Sierant, Jakub Zakrzewski, and Emanuele Tirrito. Magic dynamics in many-body localized systems, 2025.

[400] Vincenzo Cirigliano, Srimoyee Sen, and Yukari Yamauchi. Neutrino many-body flavor evolution: The full hamiltonian. *Phys. Rev. D*, 110:123028, Dec 2024.

[401] Alberto Di Meglio, Karl Jansen, Ivano Tavernelli, Constantia Alexandrou, Srinivasan Arunachalam, Christian W. Bauer, Kerstin Borras, Stefano Carrazza, Arianna Crippa, Vincent Croft, Roland de Putter, Andrea Delgado, Vedran Dunjko, Daniel J. Egger, Elias Fernández-Combarro, Elina Fuchs, Lena Funcke, Daniel González-Cuadra, Michele Grossi, Jad C. Halimeh, Zoë Holmes, Stefan Kühn, Denis Lacroix, Randy

Lewis, Donatella Lucchesi, Miriam Lucio Martinez, Federico Meloni, Antonio Mezzacapo, Simone Montangero, Lento Nagano, Vincent R. Pascuzzi, Voica Radescu, Enrique Rico Ortega, Alessandro Roggero, Julian Schuhmacher, Joao Seixas, Pietro Silvi, Panagiotis Spentzouris, Francesco Tacchino, Kristan Temme, Koji Terashi, Jordi Tura, Cenk Tüysüz, Sofia Vallecorsa, Uwe-Jens Wiese, Shinjae Yoo, and Jinglei Zhang. Quantum computing for high-energy physics: State of the art and challenges. *PRX Quantum*, 5(3), August 2024.

[402] Christian W. Bauer, Zohreh Davoudi, A. Baha Balantekin, Tanmoy Bhattacharya, Marcela Carena, Wibe A. de Jong, Patrick Draper, Aida El-Khadra, Nate Gemelke, Masanori Hanada, Dmitri Kharzeev, Henry Lamm, Ying-Ying Li, Junyu Liu, Mikhail Lukin, Yannick Meurice, Christopher Monroe, Benjamin Nachman, Guido Pagano, John Preskill, Enrico Rinaldi, Alessandro Roggero, David I. Santiago, Martin J. Savage, Irfan Siddiqi, George Siopsis, David Van Zanten, Nathan Wiebe, Yukari Yamauchi, Kübra Yeter-Aydeniz, and Silvia Zorzetti. Quantum simulation for high-energy physics. *PRX Quantum*, 4:027001, May 2023.

[403] Robert Frederik Uy and Dorian A. Gangloff. Qudit-based quantum error-correcting codes from irreducible representations of su(d), 2024.

[404] Priya J. Nadkarni and Shayan Srinivasa Garani. Quantum error correction architecture for qudit stabilizer codes. *Phys. Rev. A*, 103:042420, Apr 2021.

[405] Benjamin L. Brock, Shraddha Singh, Alec Eickbusch, Volodymyr V. Sivak, Andy Z. Ding, Luigi Frunzio, Steven M. Girvin, and Michel H. Devoret. Quantum error correction of qudits beyond break-even. *Nature*, 641(8063):612–618, 2025.

[406] Jeff Bezanson, Alan Edelman, Stefan Karpinski, and Viral B Shah. Julia: A fresh approach to numerical computing. *SIAM Review*, 59(1):65–98, 2017.

[407] Wolfram Research, Inc. Mathematica, Version 13.0.1, 2022. Champaign, IL.

[408] Guido Van Rossum and Fred L. Drake. *Python 3 Reference Manual*. CreateSpace, Scotts Valley, CA, 2009.

[409] Anaconda Inc. Anaconda Software Distribution, Vers. 2-2.4.0, 2020.

[410] J. D. Hunter. Matplotlib: A 2D graphics environment. *Comput. Sci. Eng.*, 9(3):90–95, 2007.

[411] Fernando Pérez and Brian E. Granger. IPython: a System for Interactive Scientific Computing. *Comput. Sci. Eng.*, 9(3):21–29, May 2007.

[412] Hiroki Nagakura, Kohsuke Sumiyoshi, and Shoichi Yamada. Possible early linear acceleration of proto-neutron stars via asymmetric neutrino emission in core-collapse supernovae. *The Astrophysical Journal*, 880(2):L28, 2019.

[413] Hiroki Nagakura, Taiki Morinaga, Chinami Kato, and Shoichi Yamada. Fast-pairwise collective neutrino oscillations associated with asymmetric neutrino emissions in core-collapse supernovae. *The Astrophysical Journal*, 886(2):139, 2019.

[414] Projjwal Banerjee, W. C. Haxton, and Yong-Zhong Qian. Long, cold, early r process? neutrino-induced nucleosynthesis in he shells revisited. *Phys. Rev. Lett.*, 106:201104, May 2011.

[415] Taiki Morinaga. Fast neutrino flavor instability and neutrino flavor lepton number crossings. *Phys. Rev. D*, 105:L101301, May 2022.

[416] Basudeb Dasgupta, Alessandro Mirizzi, and Manibrata Sen. Simple method of diagnosing fast flavor conversions of supernova neutrinos. *Phys. Rev. D*, 98:103001, Nov 2018.

[417] Francesco Capozzi and Ninetta Saviano. Neutrino flavor conversions in high-density astrophysical and cosmological environments. *Universe*, 8(2):94, 2022.

[418] Huaiyu Duan, George M. Fuller, J. Carlson, and Yong-Zhong Qian. Analysis of collective neutrino flavor transformation in supernovae. *Phys. Rev. D*, 75:125005, Jun 2007.

[419] Francesco Capozzi, Georg Raffelt, and Tobias Stirner. Fast neutrino flavor conversion: collective motion vs. decoherence. *Journal of Cosmology and Astroparticle Physics*, 2019(09):002, 2019.

[420] Francesco Capozzi, Basudeb Dasgupta, Eligio Lisi, Antonio Marrone, and Alessandro Mirizzi. Fast flavor conversions of supernova neutrinos: Classifying instabilities via dispersion relations. *Phys. Rev. D*, 96:043016, Aug 2017.

[421] Sajad Abbar and Maria Cristina Volpe. On fast neutrino flavor conversion modes in the nonlinear regime. *Physics Letters B*, 790:545–550, 2019.

[422] Huaiyu Duan, Alexander Friedland, Gail C McLaughlin, and Rebecca Surman. The influence of collective neutrino oscillations on a supernova r process. *Journal of Physics G: Nuclear and Particle Physics*, 38(3):035201, 2011.

[423] Sovan Chakraborty, Rasmus Sloth Hansen, Ignacio Izaguirre, and Georg G Raffelt. Self-induced neutrino flavor conversion without flavor mixing. *Journal of Cosmology and Astroparticle Physics*, 2016(03):042, 2016.

[424] Sovan Chakraborty, Rasmus Hansen, Ignacio Izaguirre, and Georg Raffelt. Collective neutrino flavor conversion: Recent developments. *Nuclear Physics B*, 908:366–381, 2016.

[425] Hans-Thomas Janka. Explosion mechanisms of core-collapse supernovae. *Annual Review of Nuclear and Particle Science*, 62:407–451, 2012.

[426] Basudeb Dasgupta. Collective neutrino flavor instability requires a crossing. *Physical Review Letters*, 128(8):081102, 2022.

[427] Bojan Žunkovič, Alessandro Silva, and Michele Fabrizio. Dynamical phase transitions and loschmidt echo in the infinite-range xy model. *Philosophical Transactions of the Royal Society A: Mathematical, Physical and Engineering Sciences*, 374(2069):20150160, 2016.

[428] Changhao Yi, Lei Ma, Joshua D Martin, and Huaiyu Duan. Dispersion relation of the fast neutrino oscillation wave. *Physical Review D*, 99(6):063005, 2019.

[429] Ian Padilla-Gay, Irene Tamborra, and Georg G Raffelt. Neutrino fast flavor pendulum. ii. collisional damping. *Physical Review D*, 106(10):103031, 2022.

[430] Soumya Bhattacharyya and Basudeb Dasgupta. Elaborating the ultimate fate of fast collective neutrino flavor oscillations. *Physical Review D*, 106(10):103039, 2022.

[431] Fernando G. S. L. Brandão, Matthias Christandl, and Jon Yard. Faithful squashed entanglement. *Communications in Mathematical Physics*, 306(3):805–830, August 2011.

[432] Andi Gu, Lorenzo Leone, Soumik Ghosh, Jens Eisert, Susanne F. Yelin, and Yihui Quek. Pseudomagic quantum states. *Physical Review Letters*, 132(21), May 2024.

[433] Andi Gu, Yihui Quek, Susanne Yelin, Jens Eisert, and Lorenzo Leone. Simulating quantum chaos without chaos, 2024.

[434] Noah Lupu-Gladstein, Y. Batuhan Yilmaz, David R. M. Arvidsson-Shukur, Aharon Brodutch, Arthur O. T. Pang, Aephraim M. Steinberg, and Nicole Yunger Halpern. Negative quasiprobabilities enhance phase estimation in quantum-optics experiment. *Phys. Rev. Lett.*, 128:220504, Jun 2022.

[435] Sebastiano Peotta, Fredrik Brange, Aydin Deger, Teemu Ojanen, and Christian Flindt. Determination of dynamical quantum phase transitions in strongly correlated many-body systems using loschmidt cumulants. *Phys. Rev. X*, 11:041018, Oct 2021.

[436] Baczewski Andrew, Christian Bauer, Bestwick Andrew, Chen Yong, Clark Susan, van Dam Wim, de Leon Nathalie, Dionne Jen, Eriksson Mark, Koch Jens, Laurence Ted, Joseph M. Lukens, McClean Jarrod, McGuire Michael, Perez Max, Roetteler Martin, Scholten Travis L., Tobar Michael, and Zorzetti Silvia. 2024 quantum information science applications roadmap, 2024.

[437] S.F.E. Oliviero, L. Leone, A. Hamma, and et al. Measuring magic on a quantum processor. *npj Quantum Inf*, 8, 2022.

[438] Lucas Johns and Zewei Xiong. Collisional instabilities of neutrinos and their interplay with fast flavor conversion in compact objects. *Phys. Rev. D*, 106(10):103029, 2022.

[439] Weiran Wang and Miguel Á. Carreira-Perpiñán. Projection onto the probability simplex: An efficient algorithm with a simple proof, and an application, 2013.

[440] James Pantaleone. Neutrino oscillations at high densities. *Physics Letters B*, 287(1):128–132, 1992.

[441] Shi-Jie Wei and Gui-Lu Long. Duality quantum computer and the efficient quantum simulations. *Quantum Information Processing*, 15(3):1189–1212, March 2016.

[442] Laurie Walk, Irene Tamborra, Hans-Thomas Janka, and Alexander Summa. Effects of the standing accretion-shock instability and the lepton-emission self-sustained asymmetry in the neutrino emission of rotating supernovae. *Phys. Rev. D*, 100:063018, Sep 2019.

[443] Abhishek Kumar Jha, Akshay Chatla, and Bindu A. Bambah. Neutrinos as qubits and qutrits. *Eur. Phys. J. Plus*, 139(1):68, 2024.

[444] Sevcan Çorbaci, Mikail Doğuş Karakaş, and Azmi Gençten. Construction of two qutrit entanglement by using magnetic resonance selective pulse sequences. In *J. Phys.: Conf. Ser.*, volume 766, page 012014, 2016.

[445] Huaiyu Duan, George M. Fuller, and Yong-Zhong Qian. Collective neutrino flavor transformation in supernovae. *Phys. Rev. D*, 74:123004, 2006.

[446] Steen Hannestad, Georg G. Raffelt, Gunter Sigl, and Yvonne Y. Y. Wong. Self-induced conversion in dense neutrino gases: Pendulum in flavour space. *Phys. Rev. D*, 74:105010, 2006. [Erratum: Phys.Rev.D 76, 029901 (2007)].

[447] John Preskill. Quantum Computing in the NISQ era and beyond. *Quantum*, 2:79, August 2018.

[448] Alexander Friedland and Cecilia Lunardini. Do many particle neutrino interactions cause a novel coherent effect? *JHEP*, 10:043, 2003.

[449] N. F. Bell, A. A. Rawlinson, and R. F. Sawyer. Speedup through entanglement: Many-body effects in neutrino processes. *Phys. Lett. B*, 573:86–90, 2003.

[450] A. Friedland, B. H. J. McKellar, and I. Okuniewicz. Construction and analysis of a simplified many-body neutrino model. *Phys. Rev. D*, 73:093002, 2006.

[451] Savas Birol, Y. Pehlivan, A. B. Balantekin, and T. Kajino. Neutrino spectral split in the exact many-body formalism. *Phys. Rev. D*, 98:083002, 2018.

[452] M. J. Cervia, A. V. Patwardhan, Akif Baha Balantekin, S. N. Coppersmith, and C. W. Johnson. Entanglement and collective flavor oscillations in a dense neutrino gas. *Phys. Rev. D*, 100(8):083001, 2019.

[453] Denis Lacroix, A. B. Balantekin, Michael J. Cervia, Amol V. Patwardhan, and Pooja Siwach. Role of non-Gaussian quantum fluctuations in neutrino entanglement. *Phys. Rev. D*, 106:123006, 2022.

[454] A Borrelli, L. Maiani, G.C. Rossi, R. Sisto, and M. Testa. Neutrinos on the lattice. the regularization of a chiral gauge theory. *Nuclear Physics B*, 333(2):335–356, 1990.

[455] David B. Kaplan. A method for simulating chiral fermions on the lattice. *Physics Letters B*, 288(3):342–347, 1992.

[456] David B. Kaplan. Chiral gauge theory at the boundary between topological phases. *Phys. Rev. Lett.*, 132:141603, Apr 2024.

[457] David B. Kaplan and Srimoyee Sen. Weyl fermions on a finite lattice. *Phys. Rev. Lett.*, 132:141604, Apr 2024.

[458] Leo P. Kadanoff. Scaling laws for ising models near T_c. *Physics Physique Fizika*, 2:263–272, Jun 1966.

[459] Thorsten B. Wahl, Arijeet Pal, and Steven H. Simon. Efficient representation of fully many-body localized systems using tensor networks. *Phys. Rev. X*, 7:021018, May 2017.

[460] Michael E. Peskin and Daniel V. Schroeder. *An Introduction to quantum field theory.* Addison-Wesley, Reading, USA, 1995.

[461] C. G. Bollini and J. J. Giambiagi. Dimensional Renormalization: The Number of Dimensions as a Regularizing Parameter. *Nuovo Cim. B*, 12:20–26, 1972.

Appendix A

THE MANY-BODY NEUTRINO SYSTEM MODEL

This section seeks to provide context on the model used in the works contained in this document, justify its usage and then finally explicitly define it, such that the reader may be able to reconstruct the very same model on their own. We will introduce two commonly used *truncated* versions of the neutrino many-body Hamiltonian: the single angle approximation, and the multi-angle approximation (a straightforward extension of the single-angle approximation). Finally we will touch on the main differences between this *truncated* version of the neutrino many-body Hamiltonian and the *full* neutrino many-body Hamiltonian.

The work presented in this dissertation focuses on the bulb model put forth by Duan *et al* [141] for systems of finite neutrino number N. Neutrino emission from the surface of the proto-neutron star is assumed to be uniform, and neutrinos are emitted as a pure eigenstate of either of the two flavors used in this work: ν_e the electron flavor or $\nu_{\tau+\mu} = \nu_x$ the heavy flavor. Later chapters cover work where neutrinos are assumed to be emitted as pure eigenstates of all three possible flavors: ν_e, ν_τ, and ν_μ.

A.1 Single-Angle Approximation

The single-angle approximation is an assumption sometimes made in the bulb model, and takes into account all neutrinos in the system but assumes that they undergo evolution of flavor ν_x along propagation direction ℓ. A simple schematic is detailed below in Fig. A.1. This approximation assumes that all of the neutrino-neutrino interactions average out to zero. A unit vector, $\hat{z}$, is oriented in the radially outwards from the proto-neutron core and is perpendicular to the neutrino emission surface, while $\hat{\varphi}$ measures the longitudinal direction (azimuthal angle) and $\hat{\theta}$ measures the latitude direction.

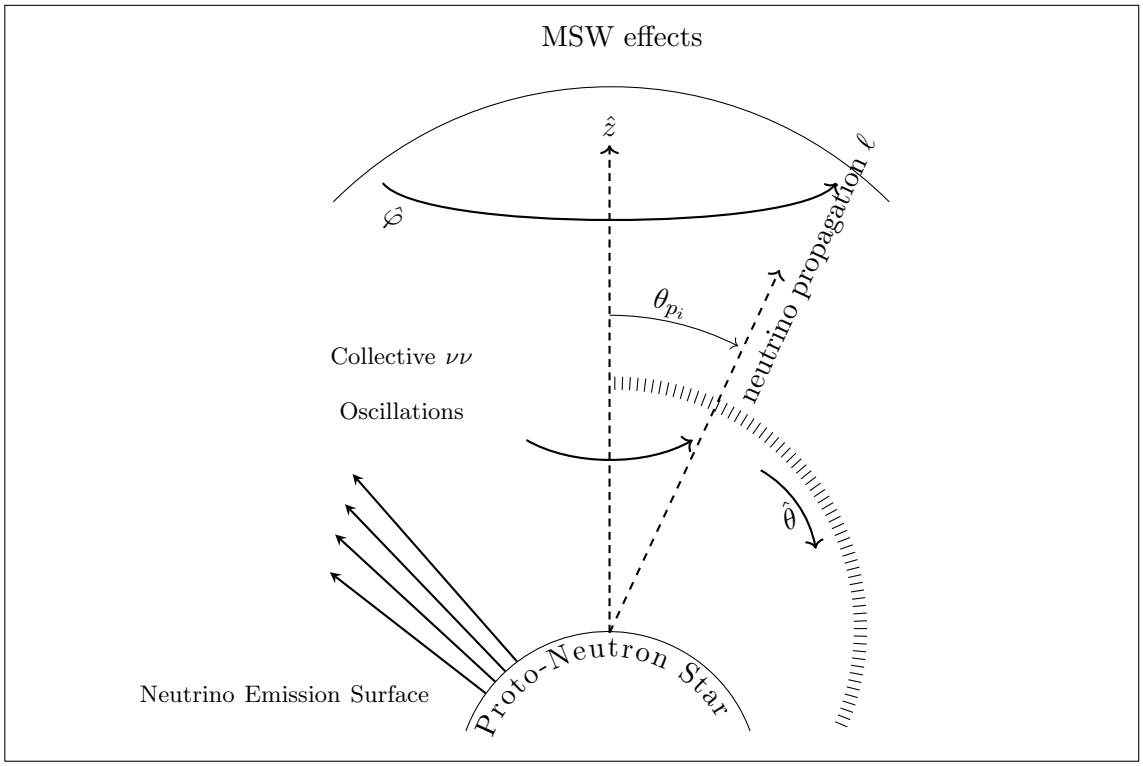

Figure A.1: Single angle schematic of core-collapse supernova region where collective neutrino flavor oscillations take place.

Our simplified H is restated below:

$$H = \frac{\sqrt{2}G_f n_\nu}{2N} \sum_{i<j}^{N} \mathcal{J}_{ij} \sigma_i^z \sigma_j^z \tag{A.1}$$

Here, we wish to define the $\mathcal{J}_{ij}$ coupling matrix term, starting from the diagram of the neutrino-neutrino interaction, in the single angle approximation. Doing the solid angle integrations for $\mathcal{J}_{ij} = (1 - \cos\theta_1 \cos\theta_2)$, we need to be careful to not overload our variables θ_1, θ_2 and θ's in general. For the single angle approximation, we need to average/ integrate around ϕ and θ, whereas for the multi-angle approximation, we only need to average/integrate around the azimuthal angle θ only. For reference, the surface area element of a unit sphere $r = 1$:

$$d\Omega = \sin\theta d\theta d\phi \tag{A.2}$$

And for the single angle, we assume one angle, so we want to integrate from 0 to some θ.

$$\begin{aligned}\iint d\Omega &= \int_0^{2\pi}\int_0^{\theta} \sin\theta' d\theta' d\phi' \\ &= 2\pi[1-\cos\theta]\end{aligned}$$

And above is how to obtain the coupling matrix for the single angle approximation. The H_{single} is then:

$$\begin{aligned}H_{\text{single}} &= \frac{\sqrt{2}G_F n_\nu}{2N}\sum_{i<j}^{N}\mathcal{J}_{ij}\sigma_i^z\sigma_j^z \\ &= \frac{\sqrt{2}G_F}{2V}\sum_{i<j}^{N}2\pi[1-\cos\theta_{ij}]\sigma_p = i^z\sigma_j^z\end{aligned} \tag{A.3}$$

where we note that $V = \frac{n_\nu}{N}$ where n_ν is neutrino number density and N is the total number of neutrinos.

A.2 Multi-Angle Approximation

In this section we detail the model in the schematic shown in Fig. A.2.

In Eq.(1.9), for a given pair of emitted neutrinos p_i, p_j, the coupling angle between them in flavor space is: $\theta_i - \theta_j = \theta_{ij}$. Rewriting the cosine term containing θ_{ij} in Eq.(1.9) in terms of its constituent neutrino trajectory vectors $\vec{p}_i, \vec{p}_j$:

$$H_{\nu\nu} = \frac{\mu}{2N}\sum_{i<j}^{N}(1-\left(\frac{\vec{p}_i\cdot\vec{p}_j}{||\vec{p}_i||||\vec{p}_j||}\right))\sigma_i\sigma_j \tag{A.4}$$

where $\vec{p}_i$ is one neutrino beam (a single flavor of either ν_e or $\nu_{\tau,\mu}$), and $\mu = \sqrt{2}G_F n_\nu$.

We work in spherical coordinates, and relabel our individual neutrino vectors as such:

$$\vec{p}_i = (r_i\sin(\theta_i)\cos(\theta_i), r_i\sin(\theta_i)\sin(\theta_i), r_i\cos(\theta_i)) \tag{A.5}$$

$$\vec{p}_j = (r_j\sin(\theta_j)\cos(\theta_j), r_j\sin(\theta_j)\sin(\theta_j), r_j\cos(\theta_j)) \tag{A.6}$$

and note that the angle formed between $\vec{p}_i$ and $\hat{z}$ is θ_i, and $\vec{p}_j$ and $\hat{z}$ is θ_j. For convenience later on, note that:

$$\begin{aligned}\vec{p}_i\cdot\vec{p}_j &= r_i r_j\sin\theta_j\sin\theta_i\cos\phi_i\cos\phi_j \\ &+ r_i r_j\sin\theta_i\sin\theta_j\sin\phi_i\sin\phi_j \\ &+ r_i r_j\cos\theta_i\cos\theta_j\end{aligned} \tag{A.7}$$

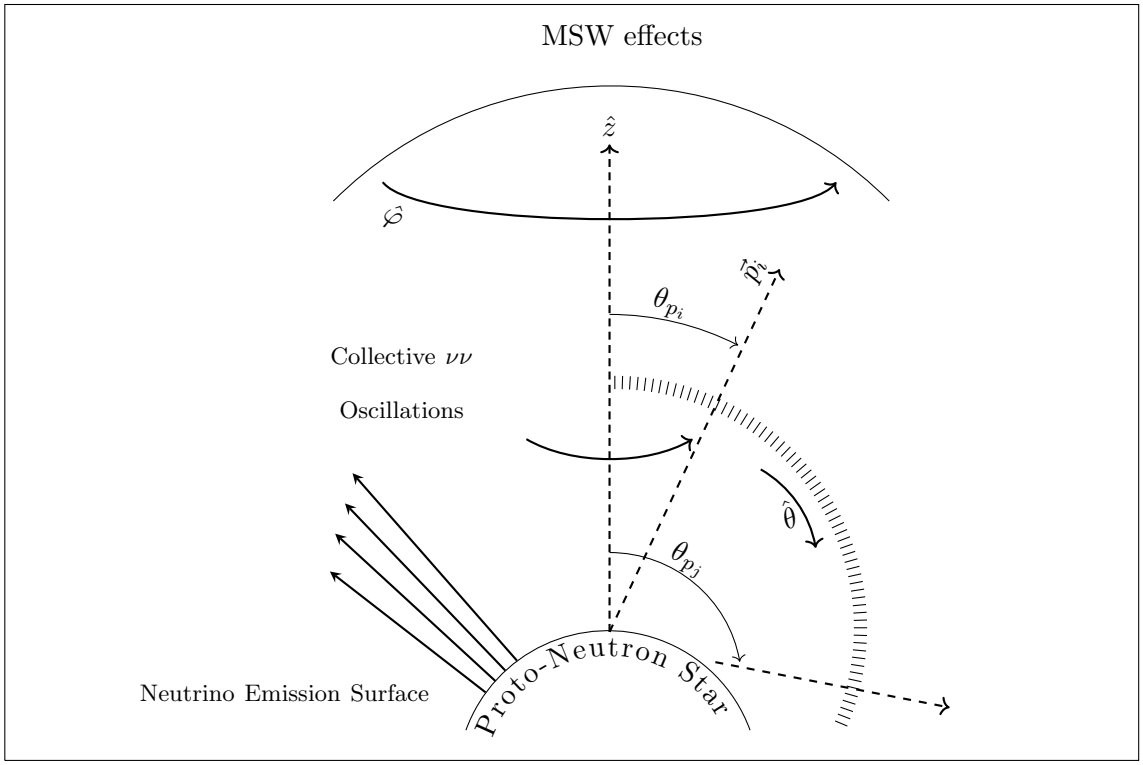

Figure A.2: Multi-Angle schematic of core-collapse supernova region where collective neutrino flavor oscillations take place. The systems in this work seek to approximate conditions found in this region, following the simplifications taken by the bulb model.

as well as:

$$||\vec{p}_i|| = \sqrt{(r_i \sin\theta_i \cos\phi_i)^2 + (r_i \sin\theta_i \sin\phi_i)^2 + (r_i cos\phi_i)^2} \tag{A.8}$$

$$= \sqrt{r_i^2(\sin\theta_i^2(\cos\phi_i^2 + \sin\phi_i^2) + cos\phi_i^2)} \tag{A.9}$$

which goes similarly for $||\vec{p}_j||$.

We now proceed to show explicitly what the interaction term

$$(1 - \left(\frac{\vec{p}_i \cdot \vec{p}_j}{||\vec{p}_i||||\vec{p}_j||}\right))$$

in Eq. A.4 transforms to, in spherical coordinates.

We proceed as follows:

$$(1 - \left(\frac{\vec{p}_i \cdot \vec{p}_j}{||\vec{p}_i||||\vec{p}_j||}\right)) = \tag{A.10}$$

$$= 1 - \frac{r_i r_j \sin\theta_j \sin\theta_i \cos\phi_i \cos\phi_j + r_i r_j \sin\theta_i \sin\theta_j \sin\phi_i \sin\phi_j + r_i r_j \cos\theta_i \cos\theta_j}{\sqrt{r_i^2(\sin\theta_i^2(\cos\phi_i^2 + \sin\phi_i^2) + \cos\phi_i^2)} \cdot \sqrt{r_j^2(\sin\theta_j^2(\cos\phi_j^2 + \sin\phi_j^2) + \cos\phi_j^2)}} \tag{A.11}$$

$$= 1 - \frac{r_i r_j(\sin\theta_j \sin\theta_i \cos\phi_i \cos\phi_j + \sin\theta_i \sin\theta_j \sin\phi_i \sin\phi_j + \cos\theta_i \cos\theta_j)}{r_i r_j \sqrt{(\sin\theta_i^2(\cos\phi_i^2 + \sin\phi_i^2) + \cos\phi_i^2)} \cdot \sqrt{(\sin\theta_j^2(\cos\phi_j^2 + \sin\phi_j^2) + \cos\phi_j^2)}} \tag{A.12}$$

$$= 1 - \frac{\sin\theta_j \sin\theta_i(\cos\phi_i \cos\phi_j + \sin\phi_i \sin\phi_j) + \cos\theta_i \cos\theta_j}{\sqrt{(\sin\theta_i^2(\cos\phi_i^2 + \sin\phi_i^2) + \cos\phi_i^2)} \cdot \sqrt{(\sin\theta_j^2(\cos\phi_j^2 + \sin\phi_j^2) + \cos\phi_j^2)}} \tag{A.13}$$

via trigonometric identities the denominator then becomes:

$$= 1 - \frac{\sin\theta_j \sin\theta_i(\cos\phi_i \cos\phi_j + \sin\phi_i \sin\phi_j) + \cos\theta_i \cos\theta_j}{1 \cdot 1}$$

Using the following shorthand: $\cos\theta_i = \mathrm{c}_{\theta_i}$, $\cos\varphi_i = \mathrm{c}_{\varphi_i}$, $\sin\theta_i = \mathrm{s}_{\theta_i}$, $\sin\varphi_i = \mathrm{s}_{\varphi_i}$, the cosine term in spherical coordinates, can be written as:

$$1 - \frac{\vec{p}_i \cdot \vec{p}_j}{||\vec{p}_i||||\vec{p}_j||} = 1 - (\mathrm{s}_{\theta_i}\mathrm{s}_{\theta_j}(\mathrm{c}_{\varphi_i}\mathrm{c}_{\varphi_j} + \mathrm{s}_{\varphi_i}\mathrm{s}_{\varphi_j}) + \mathrm{c}_{\theta_i}\mathrm{c}_{\theta_j}) \tag{A.14}$$

With this construction, for all potential neutrino trajectories $\vec{p}_i$, the $\hat{r}$ component makes no contribution, as the denominator's value of $r_i r_j$ is canceled out by a factor of $r_i r_j$ in the

numerator. We are only interested trajectories that are axisymmetric about the azimuthal angle; to make this simplification we integrate the above expression over each $\hat{\varphi}_i, \hat{\varphi}_j$, for each $\vec{p}_i, \vec{p}_j$, prefixed by a normalization constant of $\frac{1}{4\pi^2}$:

$$\begin{aligned} &\frac{1}{4\pi^2}\int_0^{2\pi} d\varphi_j \int_0^{2\pi} d\varphi_i (\mathrm{s}_{\theta_i}\mathrm{s}_{\theta_j}(\mathrm{c}_{\varphi_i}\mathrm{c}_{\varphi_j} + \mathrm{s}_{\varphi_i}\mathrm{s}_{\varphi_j}) + \mathrm{c}_{\theta_i}\mathrm{c}_{\theta_j}) \\ &= \frac{1}{4\pi^2}(1 - \mathrm{c}_{\theta_i}\mathrm{c}_{\theta_j}) \end{aligned} \tag{A.15}$$

If we wanted to work in the single angle approximation we would integrate again over $d\theta_i, d\theta_j$ as well, as we did in the previous section.

Since we do not, and are interested in heterogenous neutrino flavor-momenta, we insert Eq. A.15 after integration into Eq. A.4, absorb the normalization constant $\frac{1}{4\pi^2}$ into μ and get:

$$\begin{aligned} H_{\nu\nu} &= \frac{\mu}{2N}\sum_{i<j}^{N}(1 - \mathrm{c}_{\theta_i}\mathrm{c}_{\theta_j})\vec{\sigma_i}\vec{\sigma_j} \\ H_{\nu\nu} &= \frac{\mu}{2N}\sum_{i<j}^{N}\mathcal{J}_{ij}\vec{\sigma_i}\vec{\sigma_j} \end{aligned} \tag{A.16}$$

With Eq. (A.16), the coupling term $\mathcal{J}_{ij}$ for each pair of neutrinos σ_i, σ_j in the all-to-all connected system can be represented as an $N \times N$ matrix of products of cosines of neutrino trajectory angles subtracted from 1.

Appendix B

STATISTICS OF THE NEUTRINO COUPLING MATRICES

To gain further insight into the presence of two peaks in the Loschmidt echo crossing times, the medians of the $\mathcal{J}_{ij}$ coupling terms are examined. Figure B.1 shows the distributions of the median $\mathcal{J}_{ij}$ for each ensemble as a function of $w_\times$ [132].

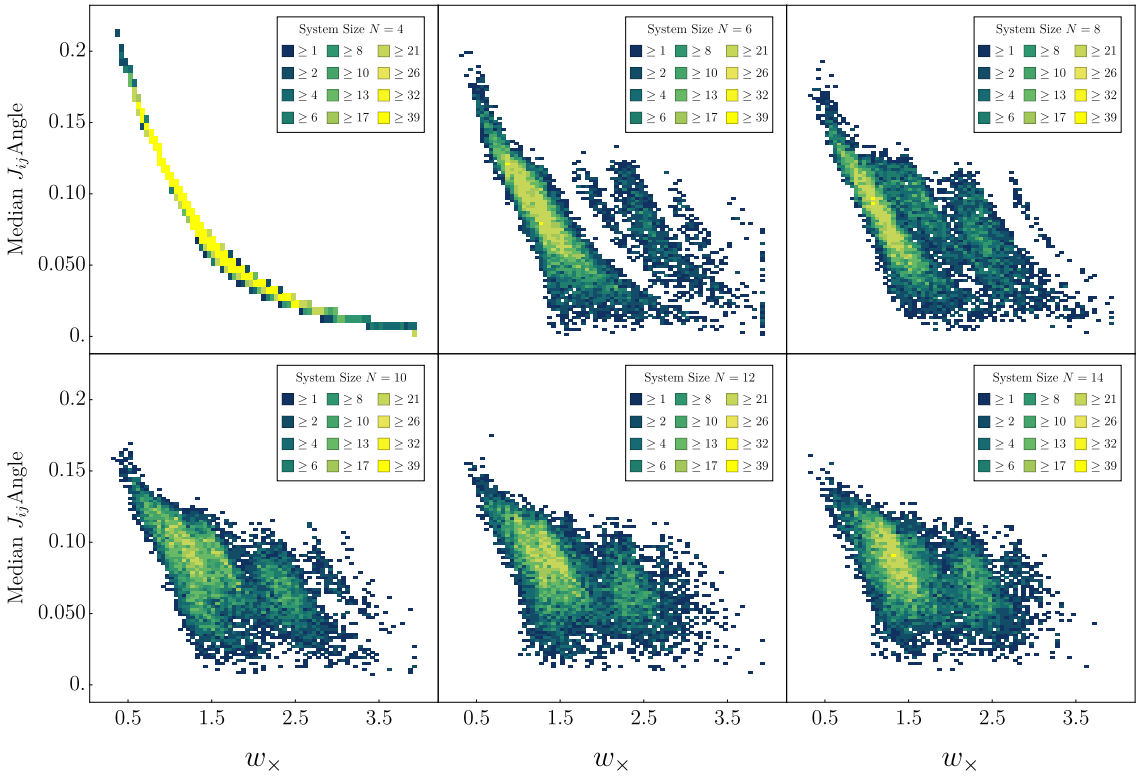

Figure B.1: Density histograms of the median $\mathcal{J}_{ij}$ for each element in the ensembles versus $w_\times$, defined in Eq. (2.25), for the systems corresponding to the histograms shown in Fig. 2.3 and described in the accompanying text. A total of 10500 systems with unique $\mathcal{J}_{ij}$'s were profiled for each density histogram in this figure.

For $N = 4$ there is essentially a 1-to-1 correspondence between the median $\mathcal{J}_{ij}$ and $t_{\mathcal{L}_\times}$,

and a single peak in the histogram of crossing times follows naturally. As the number of neutrinos increases, the distribution forms from an increasing number of bands, that merge into regions.

Medians of the $\mathcal{J}_{ij}$ coupling terms were also examined in an attempt to understand the presence of two DQPT timescales in $\log t_{\mathcal{L}_\times}$ histograms. Medians rather than means of $\mathcal{J}_{ij}$s were considered in order to avoid over representing outlier entries in the $\mathcal{J}_{ij}$s. Plotting $\mathcal{J}_{ij}$ medians as a function of $\log t_{\mathcal{L}_\times}$ for each system, scatter plots visualized a correlation between high $\mathcal{J}_{ij}$ median values and fast $t_{\mathcal{L}_\times}$'s (as seen in Figure B.1).

Preliminary results for the small N systems profiled do not support $\mathcal{J}_{ij}$ medians as a predictive tool for $t_{\mathcal{L}_\times}$. However, given that the median $\mathcal{J}_{ij}$ value for a given system is associated with that system's energy scale, we could have expected to find that for each unique $\mathcal{J}_{ij}$, $t_{\mathcal{L}_\times} * \mu * \text{median}(\mathcal{J}_{ij}) = \text{const}$. If taking N to the asymptotic limit, Fig. B.1 does not indicate that at all, however it does reveal an interesting separation of two groups of average energy scales in the systems profiled for each N.

While two distributions are seen to emerge, it remains the case that the shortest times correspond to the largest median values. While we have not explored this in detail, and leave it to future work, we anticipate that the band structure is related to the integrability of these systems, and the overlap of the initial state onto different sectors.

Appendix C

FURTHER RESULTS FROM THE LINEAR STABILITY ANALYSIS

In this Appendix [132], we show further results produced using the linear stability analysis described in Sec. 2.2. As noted there, the results are qualitatively independent of the size of the system and the choice of angular distribution: we always observe unstable modes with relatively large imaginary part $|\Gamma|$ and a second set of modes with much lower values of $|\Gamma|$ which, within numerical precision, correspond to the zero mode. The typical values of $|\Gamma|$, or equivalently the instability time scale $1/|\Gamma|$, are seen to be independent of the system size, while they are shifted by changing the angular range and shape.

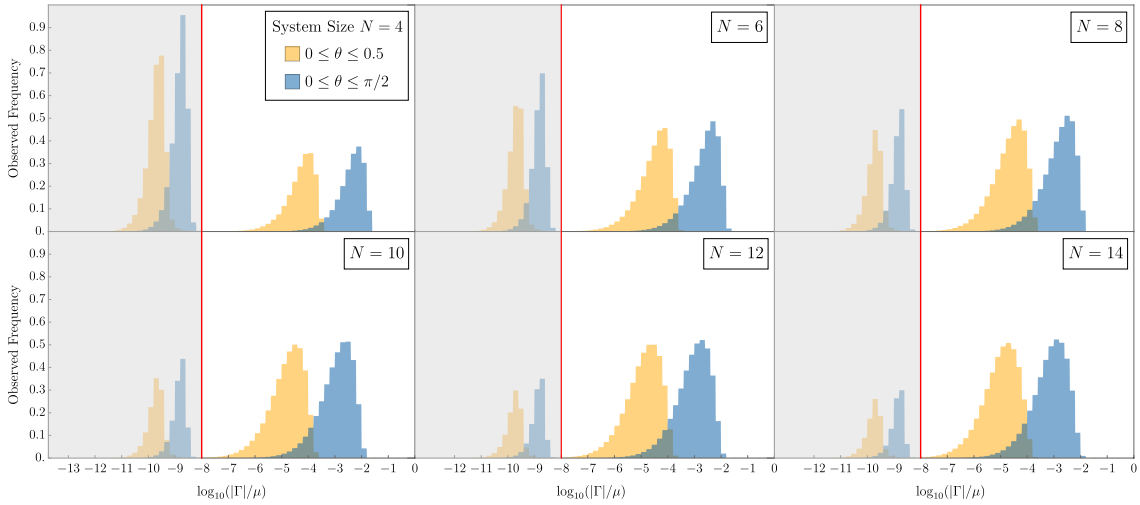

Figure C.1: Observed distribution of unstable time scales $\mu/|\Gamma|$ obtained through linear stability analysis of systems with size ranging from $N = 4$ (top left) to $N = 14$ (bottom right). Each panel shows two curves: the blue line corresponds to angles θ_j sampled uniformly in $[0, 0.5]$ while the orange line corresponds to angles sampled on a wider interval $[0, \pi/2]$. Results showing time scales longer than $10^8\mu^{-1}$ are strongly affected by numerical errors and correspond to zero-frequency modes. In order to highlight the region affected by numerical precision, we show it with a grey background and indicate its boundary as a vertical red line.

This is shown in Fig. C.1 for a range of system sizes, ranging from $N = 4$ to $N = 14$ (the same considered in the full simulation presented in Sec. 2.4), and for two angular distributions where θ_j is distributed uniformly in $[0, 0.5]$, shown as blue lines and corresponding to the results shown in Sec. 2.4, and a wider distribution with θ_j uniform in the range $[0, \pi/2]$, shown as orange lines. As expected from the definition of the coupling matrix $\mathcal{J}_{ij}$ in Eq. (2.2), the second set of results corresponding to a wider angular distribution are found to produce faster modes (on average). In order to more clearly highlight the region of time-scales affected by numerical errors, it is shown by a grey background with a boundary indicated by a vertical red line: results found in this region are numerically indistinguishable to the zero mode. Finally we note that the fraction of observations corresponding to the zero mode is progressively reduced as we increase the size of the system: this a consequence of the fact that the number of unstable modes with finite frequencies grows as a function of system size while the zero mode remains one (or, within numerical precision, a single pair of complex conjugate eigenvalues). We thus expect that in the limit of large systems, the overwhelming majority of unstable modes have finite time-scales.

Appendix D

FLAVOR DISPERSION ANALYSIS

Building upon our observations of $t_{\mathcal{L}_\times}$'s bimodal distributions, we focus our attention to potential correlations between the initial flavor configuration of the system Eq.(A.16) and $t_{\mathcal{L}_\times}$ occurrence times that arise when looking at large families of $\mathcal{J}_{ij}$ configuration matrices [132]. The XLN of a single neutrino mode is a measure of how much of that neutrino mode is in the ν_e or $\nu_{\tau,\mu}$ state, or some mixture of both. Previous work has established the predictive value of XLN angular distributions with respect to CFCs [194, 420, 171, 419, 165, 429], and recently, XLN crossings' direct relationship to CFCs and DQPTs [428, 122, 415, 426].

Following the work by Capozzi *et al* [419], within the same bulb model approximation, we consider only: a monochromatic system where all of the neutrinos' energies are the same and symmetry about the $\hat{z}$ axis. The $\hat{z}$ axial symmetry means that each i-th neutrino emitted at θ_i corresponds to one neutrino mode consisting of a conical shell of neutrinos all emitted at that θ_i; from here on we will refer to each neutrino in our system as a neutrino mode. With these simplifications, the orientation of each spin (neutrino mode) along $\hat{z}$ gives the XLN, in accordance with Fig. A.2. We can then redefine the dimensionless XLN angle distribution as $G(u)$, for each neutrino mode in our system:

$$G(u) = \frac{1}{n_\nu} \sum_i \langle \sigma_i^z \rangle \delta(u - u_i), \tag{D.1}$$

where we have normalized $G(u)$ with the sum of the total neutrino number densities of both flavors in the system. Within the delta function, we define $u = \cos\theta$, with θ able to take on any trajectory value between. Given this construction, we have N $G(u)$s, one for each neutrino mode in a system of size N.

To contextualize the XLN angle distribution's connection to neutrino flavor coherence, we begin with the equations of motion describing flavor coherence and occupation number

dynamics in flavor space, as defined in Eq.(1) of Dasgupta *et al* [416]. The background matter interaction and vacuum contribution term continue to be neglected here. Linearizing this kinetic equation allows us to focus on the neutrino density matrices describing a two flavor system, in our case $\nu_e, \nu_{\tau+\mu}$ [424, 416]:

$$\varrho = \frac{f_{\nu_e} + f_{\nu_{\tau+\mu}}}{2} \begin{pmatrix} 1 & 0 \\ 0 & 1 \end{pmatrix} + \frac{f_{\nu_e} - f_{\nu_{\tau+\mu}}}{2} \begin{pmatrix} s & S \\ S^* & -s \end{pmatrix}. \tag{D.2}$$

Occupation number densities for both flavors are $f_{\nu_e}, f_{\nu_{\tau+\mu}}$; a sign flip $(-f_{\nu_e}, -f_{\nu_{\tau+\mu}})$ yields occupation number densities for antineutrinos. The real-valued diagonal components contain the neutrino number densities and the complex-valued off-diagonal components S (S^*) describe the neutrino (antineutrino) flavor coherence.

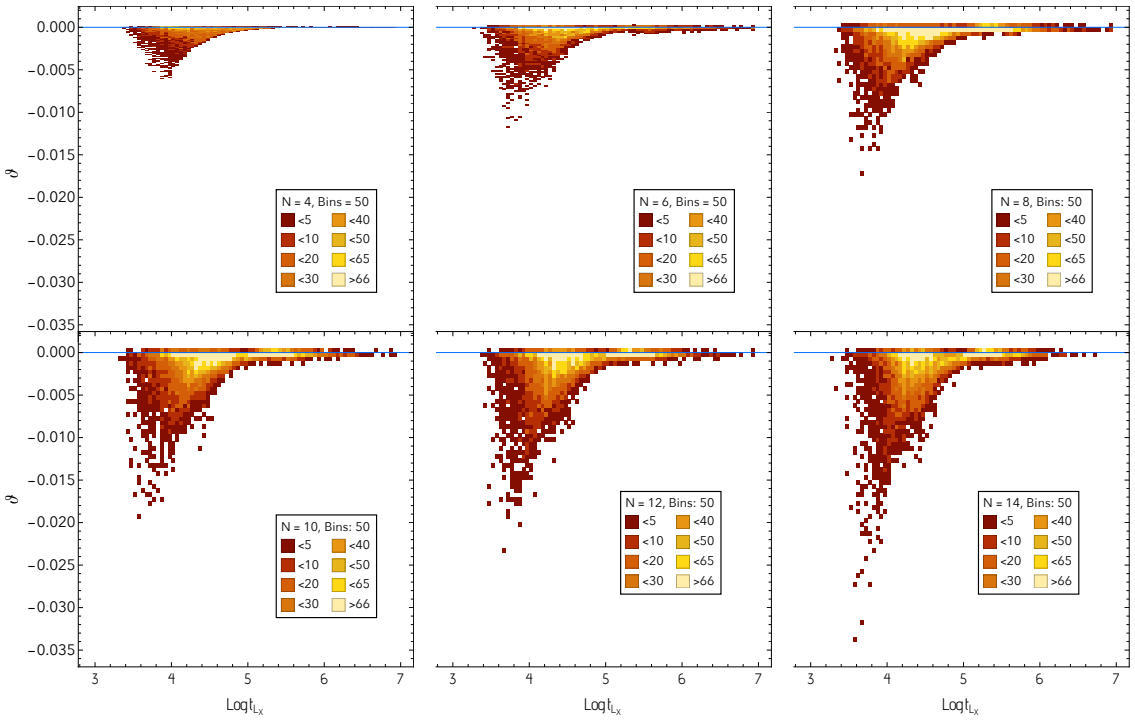

Figure D.1: Density scatter plots of the discriminant ϑ (Eq.(D.6) on vertical axis) as a function of $\log t_{\mathcal{L}_\times}$ (on the horizontal axis) for system sizes $N = 4, 6, 8, 10, 12, 14$. Coupling angles for each neutrino flavor were sampled from random uniform distributions constrained to lie between $[0.0, 0.5]$ radians. For all N, 60 bins were used for the intensity plots, with $10,500$ unique $\mathcal{J}_{ij}$ configurations studied for each N.

Because our system consists of a single cone of multiple flavor modes (many flavor modes all contained within one flavor wave packet), the inhomogeneity wave vector $\mathbf{k} = 0$. With this simplification, when we write solutions to the linearized equation of motion of neutrino flavor coherence S_u in Fourier space as done in Ref.[416] we can neglect the wave number-dependent exponential term, which yields:

$$S(t) = Q(\Omega)e^{-i(\Omega t)}, \tag{D.3}$$

where Ω is the oscillation frequency of a propagating neutrino wave packet that a stationary observer would see. Restricting attention to the fast flavor conversion modes of an axisym-

metric distribution around $\hat{z}$, we seek solutions to the neutrino flavor coherence portion of the linearized kinetic equation, S, in terms of Ω:

$$\Omega = -\mu \frac{\mathcal{G}_0 - \mathcal{G}_2 \pm \sqrt{(\mathcal{G}_0 + \mathcal{G}_2)^2 - 4\mathcal{G}_1^2}}{2}, \tag{D.4}$$

where the coherent neutrino CFC frequency Ω is formulated in terms of $\mathcal{G}_n$ distributions, which consist of higher order moments of Eq.(D.1)–as articulated previously in Refs.[416, 419]:

$$\mathcal{G}_n = \sum_{i=1}^{N} G(u)(\cos\theta_i)^n. \tag{D.5}$$

Unlike in Ref.[419], our system is discretized to N individual neutrino modes, so rather than an integral we use a discreet sum made up of higher moments of our XLN angle distribution Eq.(D.1) for our system's $\mathcal{G}_n$ distribution. As defined in Eq.(A.16), each θ_i corresponds to a u-th neutrino mode for every unique $\mathcal{J}_{ij}$. Since there is a one-to-one correspondence between each θ_i and $G(u)$ for a given system, we can also iterate the sum in Eq.(D.5) over u, which is effectively the same as iterating over i.

Looking closely at Ω's definition, we can see that the discriminant of Eq.(D.4):

$$\vartheta = (\mathcal{G}_0 + \mathcal{G}_2)^2 - 4\mathcal{G}_1^2, \tag{D.6}$$

determines whether we have exponentially growing flavor coherence, depending on whether Eq. (D.6) takes on a complex value or not. Note that ϑ is a property of a particular system's initial state flavor configuration, at time $t = 0$ when that system's quench $\mathcal{J}_{ij}$ is first applied. Histograms of ϑ did not reveal any meaningful structure. In investigating the correlation between the discriminant ϑ and $t_{\mathcal{L}_\times}$, where Eq. D.6 is studied as a function of the $t_{\mathcal{L}_\times}$. As N increases, $\vartheta(t_{\mathcal{L}_\times})$ separates into two statistically significant modes within the scatter plots of Fig. D.1.

At $N = 6$ a split emerges in the same location as where the histograms of $\log t_{\mathcal{L}_\times}$ separate into two modes. Two concentrations of negative ϑs close to the x-axis develop in the two separated regions; the clustering indicates two modes made up of amplifying frequencies Ω spanning two different ranges. As N increases, the first mode consistently contains the greatest amplified Ωs. While negative or positive values of Eq. (D.6) within 0 ± 0.0020 can

correspond to any value of $\log t_{\mathcal{L}_\times}$, negative discriminant values less than -0.0025 indicate a clear correlation with being located in the first mode of the bimodal $\log t_{\mathcal{L}_\times}$ histogram, for all N. As noted in [416], modes with complex Ω can potentially cause exponentially growing instabilities, motivating further study of systems with relatively lower negative ϑ values.

Whether the discriminant can be used as an initial state tool to predict when a system's $t_{\mathcal{L}_\times}$ would occur, given a particular $\mathcal{J}_{ij}$ configuration, requires additional study. This could be done in the form of exploring its predictive strength for larger N, as well as analyzing its relationship to the second, third, or later $t_{\mathcal{L}_\times}$s. We have found that for large negative values of ϑs, there is a non-negligible correlation to fast $t_{\mathcal{L}_\times}$s, but for slower $t_{\mathcal{L}_\times}$s, it becomes increasingly difficult to use ϑs as a predictive tool, though this appears to improve with larger N.

Appendix E

DIMENSIONAL REGULARIZATION-INSPIRED MEDIAN ABSOLUTE DEVIATION SCALING METHOD FOR HIGH-DIMENSIONAL PARAMETER SPACES

Here, we introduce a novel statistics analysis technique, for establishing correctly-scaled parameter ranges given a high-dimensional fit function, inspired by dimensional regularization [132]. When fitting a function to a set of data, the number of correlated parameters in the fitting function can determine how many potentially good fits fall within certain confidence interval (CI), before a specific fit is no longer of sufficient quality. However, for functions with many parameter spaces the number of fits whose χ^2/dof fall within a specified CI bound increases.

In such situations, estimating the boundaries of the CI interval can only be done via numerically searching the parameter space of the function, selecting only fits whose uncorrelated χ^2/dof falls within the specified CI. However, when fitting functions with high numbers of parameters, it is possible to conduct an aggressive search through the parameter spaces of the function, and find not just fits that lie within the CI threshold, with parameter values lying within reasonable expected ranges, but outlier fits, which contain parameter values that wildly deviate away from the norm of parameters belonging to functional fits within the CI.

In this case, the standard approaches for understanding the CI range for each parameter fail to capture realistically what is really being sampled during the fit finding, or account for the higher dimensional parameter space that is being traversed through. A simple range calculation over-estimates a true range of acceptable values for a given parameter, and yet so does a straightforward median absolute deviation (MAD) calculation as well. What is needed is an accurate standard deviation, scaled appropriately to the parameter space by some factor ξ, but determining ξ is the issue, when working with a high number of parameter spaces.

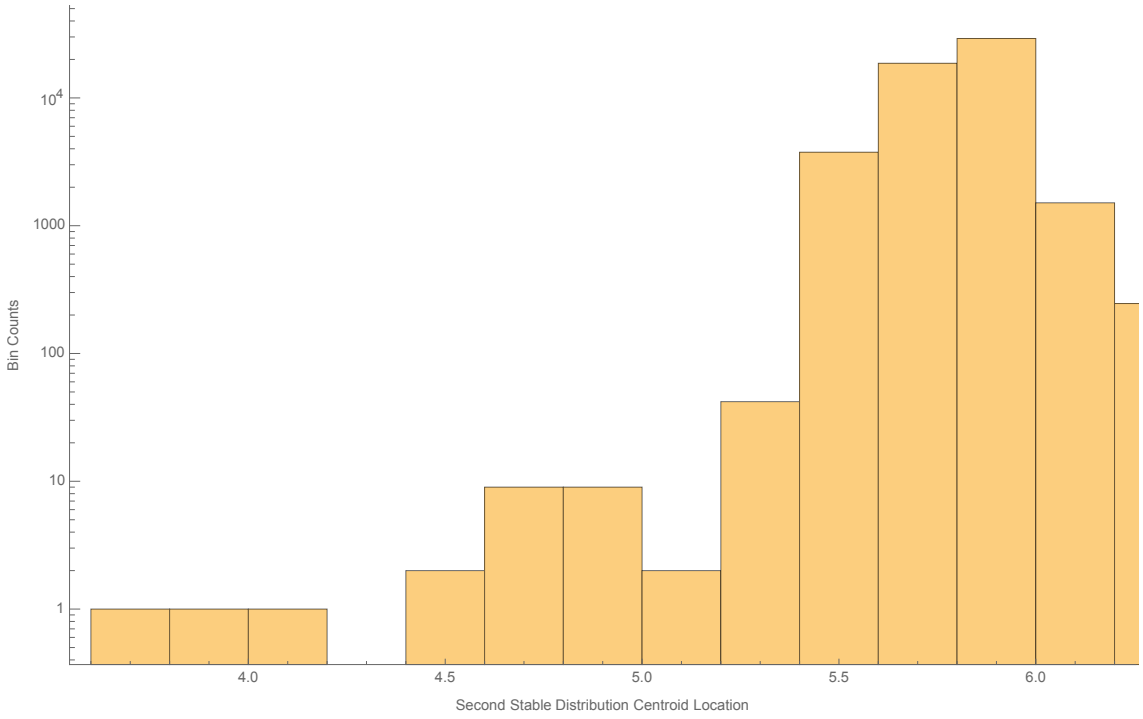

Figure E.1: Example of outlier values of a parameter, when looking at distribution of parameter values for accepted fits within a confidence interval bound. Histogram is log-scaled on the y-axis to highlight presence of outlier parameter values. Making a simple range estimate to assess the parameter space of accepted values would be misleading, as it is not a uniform nor even continuous distribution of values within such a range.

A solution to this is implementing a dimensional-regularization approach on the parameter space. This translates to taking a count of how many parameter spaces are being searched when finding fits that lie within a CI threshold, say n. Then, approximate the search over each parameter space to be of some distribution representative of how the candidate parameter values are being sampled from the parameter spaces, and the approximating that distribution to lie within an n-dimensional sphere. We wish to understand how this translates to one dimension, a single parameter, so integrate out all $n-1$ dimensions, till we are left with a ξ in one dimension.

For our case, our sampling procedure over each parameter space was uniformly distributed. We worked in a 10 dimensional parameter space, for the function we wished to

fit, so we initially start out with a 10-dimensional sphere describing the geometry our 10-dimensional parameter space. Defining the volume of an n-dimensional sphere via the $\Gamma(R)$ function:

$$V_n = \frac{\pi^{\frac{n}{2}} R^n}{\Gamma(\frac{n}{2}+1)} \tag{E.1}$$

Where for $n = 10$ we have: $V_{10} = \frac{\pi^5 R^{10}}{120}$, and thus the probability distribution function (PDF) would look like:

$$V_n = \begin{cases} \frac{120}{\pi^5 R^{10}}, R \geq \sqrt{a^2 + b^2 + ... + i^2 + j^2} \\ 0 \quad \text{elsewhere} \end{cases} \tag{E.2}$$

We then simply integrate out $n = 1$ dimensions from the PDF, in this case nine dimensions from ten. Now that we have projected down to one dimension, we are left with a constant–in our case, our constant is 0.2058(6). This is our scale parameter ξ such that:

$$\text{standard deviation}_k = \xi \cdot \text{MAD}_k \tag{E.3}$$

Where k stands for any given parameter in our ten parameter space.

Appendix F

ADDITIONAL STATISTICAL ANALYSES OF ECHO TIME SCALES

This portion of the appendices focuses on additional analyses conducted when large collections of unique $\mathcal{J}_{ij}$ configurations are studied for systems with $N = 4, 6, 8, 10, 12,$ & 14 sites [132]. A bimodal distribution emerged in the configurations' collective echo crossing behavior, as N increased (Fig. 2.3), in histograms of $t_{\mathcal{L}_\times}$ for each N. While ultimately three distributions were examined, (see Table G.1), the primary focus of this document is on systems with coupling angles constituting $\mathcal{J}_{ij}$ drawn from random uniform distributions, though triangular and Gaussian distributions were also studied.

Prior to fitting the distributions in Fig. 2.3 with the stable distributions as defined in Eq. 2.27, the bimodal features of Fig. 2.3 initially presented as being best described by either a single gaussian G_1 or a double "bimodal" gaussian G_2. Thus, initially, both G_1 and G_2 were fit to Fig. F.1's histograms via Mathematica's Nonlinear Model Fitter (NLFM) function:

$$G_1 = a_1 e^{\frac{-(x-\mu_1)^2}{2\sigma_1^2}} \tag{F.1}$$

$$G_2 = a_1 e^{\frac{-(x-\mu_1)^2}{2\sigma_1^2}} + a_2 e^{\frac{-(x-\mu_2)^2}{2\sigma_2^2}} \tag{F.2}$$

For G_1 and G_2, a_1 and a_2 are amplitudes for each Gaussian peak, μ_1, μ_2 are the locations of the peak means, and σ_1, σ_2 are the standard deviations of each peak. For each histogram bin number, the functions G_1, G_2 were given a guess for the amplitudes a_i, peak mean locations μ_i, and standard deviations σ_i of each mode. From there, NLFM used a least squares objective function to fit G_1, G_2–given a new set of initial guesses for $a_1, a_2, \mu_1, \mu_2, \sigma_1, \sigma_2$– to each histogram of $t_{\mathcal{L}_\times}$s, for a range of histogram bin numbers Υ.

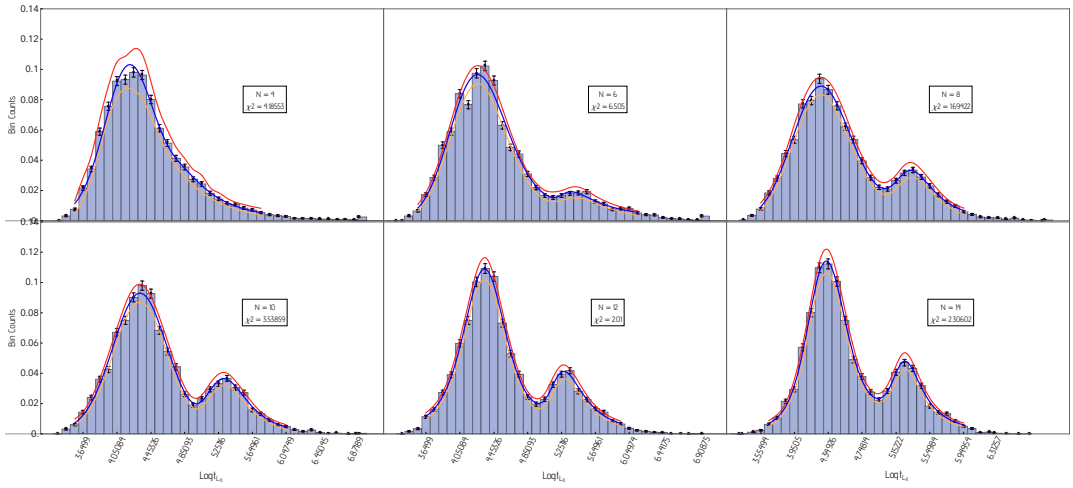

Figure F.1: Histograms of the Loschmidt echo crossing times are presented for system sizes of $N = 4, 6, 8, 10, 12$ & 14 neutrinos. Vertical axis measures histograms bin counts (30 bins used $\forall$ N), the horizontal axis measures the $t_{\mathcal{L}_\times}$ in units of μ^{-1} on log scale. Coupling angles for each neutrino flavor were sampled from random uniform distributions constrained between $[0.0, 0.5]$, with 3,500 unique configurations sampled for each N. Dark orange pickets mark standard error, gold curves trace the double Gaussian fit generated via Mathematica's NonlinearModelFit (NLMF) function. At $N = 4$ the histogram contains only one mode, but as N increases, a gradual split emerges. Both means of the bimodal distribution remain constant as N increases, whereas each mode's spread gradually decreases, as both the primary and secondary peaks become sharper with increasing site number N.

Taking a closer look at Fig. F.1, in the first panel where $N = 4$, a Gaussian fit with a single mode Eq. F.1 seemed to dominate the histogram, though Eq (F.2) still produced a better fit. At around $N = 6$ sites, the echo crossing distributions gradually begin to separate into two modes (second panel), then beginning at $N = 8$ sites (through $N = 14$), a bimodal distribution of $\log(t_{\mathcal{L}_\times})$ emerges and becomes increasingly sharply peaked as each mode for G_2 increases in amplitude a_1, a_2 and decreases in standard deviation σ_1, σ_2, while their means μ_1, μ_2 remained constant, as N increased. Below is a table of the best fit parameters used when fitting G_2 to Fig. F.1, in the initial analysis. We focus on G_2 rather than G_1 as G_2 yielded consistently better quality fits as determined by the uncorrelated χ^2 values,

which are also contained within this section.

Statistical verification of results focused on evaluating the quality of NLFM's G_1, G_2 fits, as well as their stability. Goodness of fit was defined by the uncorrelated χ^2 of both G_1, G_2 fitted to the histogram (see Fig. F.2 in this section), which consistently demonstrated worse fit values for G_1 than for G_2 over a bin number range of $25 - 100$. Stability of the G_1, G_2 fits was defined via the the mean values of the two modes as a function of bin size, (see Fig. F.2 in appendix), with mean values remaining relatively consistent over a bin number range of 25 to 100. The same process was repeated for varying time step sizes of $t_{step} = [0.02\mu^{-1}, 0.05\mu^{-1}, 0.07\mu^{-1}, 0.1\mu^{-1}]$.

Uncorrelated χ^2 was chosen over correlated χ^2 as the latter assumes correlation while the former acts as a worst case lower bound when assessing the NLFM's fitting of Eqs. F.1 & F.2. For each N's histogram of $\log t_{\mathcal{L}_\times}$, the χ^2 was calculated as:

$$\delta_{\Upsilon_j^{\mathcal{S}},G_i} = \left|G_{i,\Upsilon_j} - \Upsilon_j^{\mathcal{S}}\right|; i \in 1,2 \tag{F.3}$$

$$\chi^2_{G_i} = \sum_{j=1}^{\Upsilon^{\mathcal{S}}_{totalbins}} (\delta_{\Upsilon_j^{\mathcal{S}},G_i})^2 \frac{1}{\sigma^2_{\Upsilon^{\mathcal{S}}}} \tag{F.4}$$

where $\delta_{\Upsilon_j^{\mathcal{S}},G_i}$ is the fit residuals: the distance between Mathematica's NLFM function's fitted G_1 or G_2 values for a histogram with a particular bin size $\mathcal{S}$, and the Histogram's actual bin heights $\Upsilon_j^{\mathcal{S}}$, at each bin j. The variance of bin heights $\sigma^2_{\Upsilon^{\mathcal{S}}}$ for each histogram with a certain bin size $\mathcal{S}$ was calculated only with bins of non-zero height, with $\sigma^2_{\Upsilon^{\mathcal{S}}} = \langle(\Upsilon_j^{\mathcal{S}})^2\rangle - (\overline{\Upsilon^{\mathcal{S}}})^2$, where $\overline{\Upsilon^{\mathcal{S}}}$ is the mean bin height for all j bins, given a bin sizing $\mathcal{S}$. The NLFM fit's degrees of freedom were undetermined and thus was not factored into the calculation of χ^2.

Table F.1: Table of best fit parameters used in fitting the double Gaussian G_2 to the Loschmidt echo crossing $t_{\mathcal{L}_\times}$ histograms for each system size N studied in Fig. F.1. Each parameter is accompanied by their respective standard error in parenthesis, eg: $(\sigma_{\hat{\mu_1}})$. Each row in the table corresponds to a particular best fit parameter accompanied by its respective standard error in the previously described format, as follows: the first Gaussian mode's amplitude is $a_1(\sigma_{\hat{a_1}})$, the first Gaussian mode's mean is $\mu_1(\sigma_{\hat{\mu_1}})$, the first Gaussian mode's variance is $\sigma_1(\sigma_{\hat{\sigma_1}})$, the second Gaussian mode's amplitude is $a_2(\sigma_{\hat{a_2}})$, the second mode's mean is $\mu_2(\sigma_{\hat{\mu_2}})$, the second Gaussian mode's variance is $\sigma_2(\sigma_{\hat{\sigma_2}})$.

G_2 Parameters	$N=4$	$N=6$	$N=8$	$N=10$	$N=12$	$N=14$
$a_1(\sigma_{\hat{a_1}})$	330(24)	332(11)	303.9(7.7)	319.9(8.1)	347.5(9.1)	381(10)
$\mu_1(\sigma_{\hat{\mu_1}})$	4.204(13)	4.267(10)	4.275(10)	4.317(09)	4.319(09)	4.328(07)
$\sigma_1(\sigma_{\hat{\sigma_1}})$	0.280(14)	0.308(08)	0.324(08)	0.319(07)	0.282(07)	0.252(06)
$a_2(\sigma_{\hat{a_2}})$	85.9(13)	58.8(3.7)	98.4(4.4)	104.3(4.9)	110.7(4.8)	121.5(5.1)
$\mu_2(\sigma_{\hat{\mu_2}})$	4.84371(85)	5.24376(28)	5.34337(61)	5.39714(41)	5.3362(42)	5.27536(35)
$\sigma_2(\sigma_{\hat{\sigma_2}})$	0.492655(35)	0.594945(62)	0.364758(92)	0.310463(79)	0.349641(87)	0.327(14)

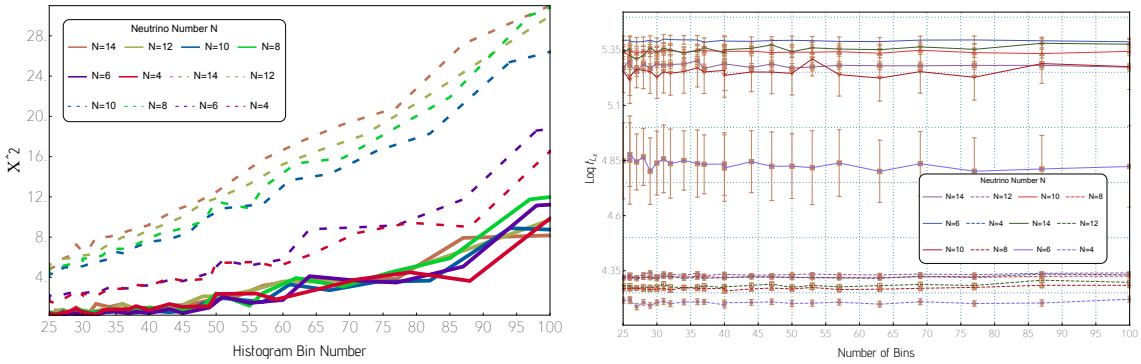

Figure F.2: The left figure contains results of uncorrelated χ^2/dof fits to the NLFM-approximated fits of a Gaussian with one centroid (Eq.(F.1)) and a Gaussian with two centroids (Eq. (F.2)), to histograms of $\log t_{\mathcal{L}_\times}$. Uncorrelated χ^2/dof of fits of a Gaussian with a single mode are denoted in dashed lines; those of a Gaussian with two modes are denoted by thick solid lines. Fit values (vertical axis) were calculated as a function of histogram bin size (horizontal axis).

The right figure contains both mode medians for the double Gaussian fitted to the histograms of $\log t_{\mathcal{L}_\times}$ for systems of N neutrinos, as a function of the histogram bin size. Dashed lines correspond to the first mode's median and solid lines to the second mode's. Dark orange bars denote standard error. As N increased, the NLFM-approximated centroids of both modes for each histogram settled into two distinct values which remained stable over bin size.

Stability of Mathematica's NLFM's fits of G_1, G_2 in Fig. F.1 was assessed via the above definition of χ^2 for both G_1, G_2, and was supported by visual analysis of the adjusted $\mathcal{R}^2$ for both G_1, G_2, and by the clear separation of mean values in Fig. F.2. The second mode's stability improves as the number of system sites N increases. The relatively consistent difference between the mean values of both the modes indicates that the modes are distinct from one another, and not an artifact of bin number.

Using the definition in Eq. F.4, χ^2s of NLFM fits of $\mathrm{G}_1, \mathrm{G}_2$ in Fig. F.1 reliably demonstrates a closer fit, as seen by G_2's consistently higher χ^2's than G_1, regardless of bin size $\mathcal{S}$, in Fig, F.2. This qualified the G_2 function as a more accurate fit for the bimodal $t_{\mathcal{L}_\times}$ distribution in Fig. F.1. Stability of the G_2 function fit to Fig. F.1 was confirmed by tracking the means of both modes of G_2, as seen in Fig. F.2, as a function of bin size $\mathcal{S}$. The

relatively consistent difference between the mean values of both the modes indicates that the modes are consistently distinct from one another, and not an artifact of bin number. The stability of the fit is quantified by the mean values of each mode: as N increases both modes settle into two stable $\log t_{\mathcal{L}_\times}$s, at around around $\log t_{\mathcal{L}_\times} = 4.2$ and $\log t_{\mathcal{L}_\times} = 5.37$, see Fig. F.2.

Though Fig. F.2's uncorrelated χ^2s show the quality of both the single and double Gaussian fits degrading past optimal bin numbers, the better quality of fit of double Gaussian fits (solid lines) over the single Gaussian fits (dashed lines) is consistently demonstrated, since regardless of the bin size $\mathcal{S}$ and for all system sizes N the $\chi^2_{\mathrm{G}_2}$ is always lower than $\chi^2_{\mathrm{G}_1}$. Coupled with Fig. F.2, the stability of the bimodal distribution–and its independence of the number of neutrinos N– is further substantiated.

While G_1 and G_2 provided initial evidence confirming the presence of two distinct modes emerging from the Loschmidt analysis, they were ultimately discarded in favor of the stability distributions as defined in Eq. 2.27. This was due to the higher quality fits that Eq. 2.27 provided, as validated by the χ^2/dof values in Table 2.1.

Appendix G

ADDITIONAL ANGULAR DISTRIBUTIONS STUDIED

Spherically asymmetric neutrino emission has previously been studied in models similar to the multi-angle approach used in this work [413, 144]. Previous studies have also taken into account heterogenous distributions of various quantities such as neutrino emission angles, colors or species [425, 412, 144], where emission asymmetries of such neutrino attributes can be credited to the non-uniform hydrodynamics occurring in the accretion layers of a collapsing supernova core.

In line with these physically relevant observable asymmetries, Gaussian distributions were also studied to roughly approximate angularly asymmetric neutrino flavor emission. Triangular distributions were chosen simply as a statistical edge case, to verify consistency of observations due to its frequent use in situations where data is insufficient and its relatively extreme angular asymmetry. Studies varying the amount of neutrino species relative to one another in the initial system, as well as studying a multi-chromatic system warrant further exploration.

Table G.1: Table of distribution types and corresponding probability density functions and angular ranges used in the MPS TEBD simulations for systems sizes $N = 4, 6, 8, 10, 12, 14$. For the random uniform distribution, $a = \theta_{max}, b = \theta_{min}$ bound the angular range the distribution was sampled for. For the Gaussian distribution, with mean μ and variance σ, values sampled were constrained to lie within $p(x)$'s range at $[0.0, 0.5]$ with resampling conducted as necessary. For the Triangular distribution, l, m, r are the left endpoint, location of the peak, and the right endpoint of $p(x)$, respectively.

Distribution Type	Probability Density Function	Angular Range
Random Uniform	$p(x) = \frac{1}{a-b}$	$a = 0.50$ $b = 0.00$
Gaussian	$p(x) = \frac{1}{\sqrt{2\pi\sigma^2}} e^{\frac{(x-\mu)^2}{2\sigma^2}}$	$\mu = 0.25$ $\sigma = 0.15$
Triangular	$p(x, l, m, r) = \frac{2(x-l)}{(r-l)(m-l)}$ for $l \leq x \leq m$ and $p(x, l, m, r) = \frac{2(r-x)}{(r-l)(r-m)}$ for $m \leq x \leq r$	$l = 0.00$ $m = 0.25$ $r = 0.50$

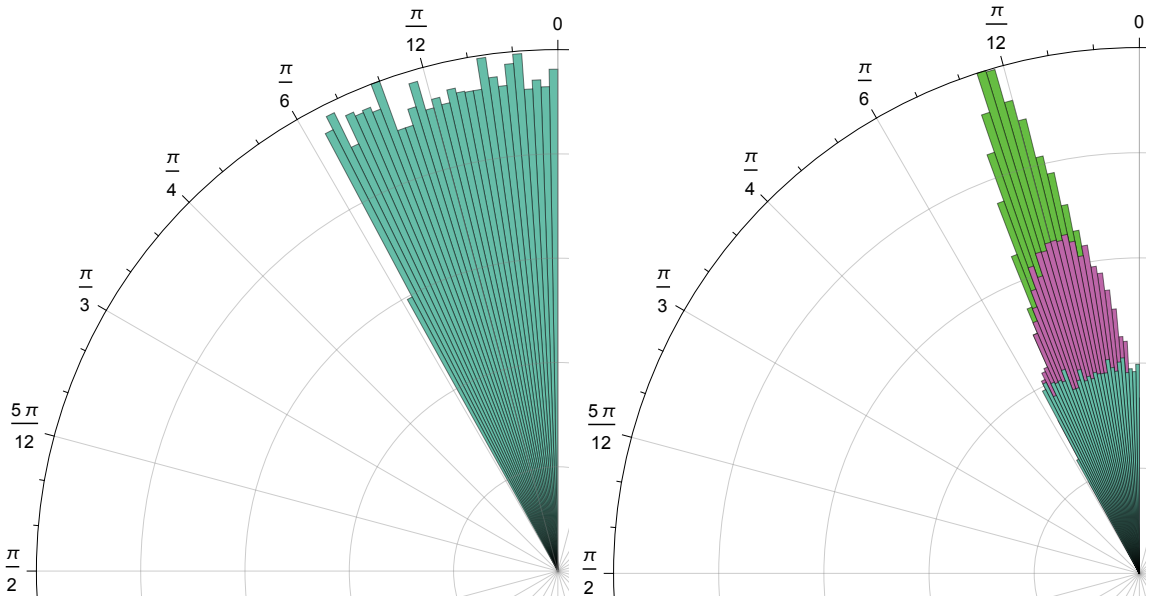

Figure G.1: The leftmost figure contains a visualization of the $\mathcal{J}_{ij}$ angle spectra that were sampled. To focus on forward peaked neutrino trajectories, θ_is were constrained to the $[0.0, 0.5]$ range. Actual θ_is sampled from the random uniform distribution is in the angular histogram above. The rightmost figure contains angular histogram of θ_is constituting the $\mathcal{J}_{ij}$s of Eq.(A.16) for all three distributions that were ultimately studied in this document. Angles sampled from a random uniform distribution were constrained to a lie within a range of $[0.0, 0.5]$ radians. In the rightmost composite angular histogram are triangular (bright green), Gaussian (magenta) and random uniform distributions (teal blue). For each distribution, θ_is constituting the $\mathcal{J}_{ij}$s were sampled from and the subsequent families of H were studied.

When building $\mathcal{J}_{ij}$s, neutrino trajectory angles θ_i, θ_j were sampled from angle ranges θ_Δ much smaller than $\frac{\pi}{2}$, as physically relevant angle ranges for the model used allowed only for trajectories emitting outwards from the neutrino-emission sphere surface, see Fig. G.1 for visualizations. Neutrino trajectory angles θ_i's were sampled from several probability distributions, with random uniform distributions being the main focus in this study.

Random uniform distributions were chosen for their relevance to the bulb model's assumption of uniform neutrino emission from the proto-neutron star surface. For the analysis described in this paper, distributions were constrained to lie within an angle range of

$\theta_\Delta = [0.0, 0.5]$, since the angle range was small enough to qualify only physically relevant trajectories, while spanning a substantially larger range of angles than those investigated in previous works. Different random angular distributions were also studied, constrained within various θ_Δs, and demonstrated similar qualitative behavior; for more details please refer to later sections in this chapter.

For brevity we present results only for the parameters listed in Table (G.1). We found the results of $\mathcal{J}_{ij}$s composed of both Gaussian and Triangular angular distributions asymptotically consistent with those of the random uniform distributions. A bimodal distribution of log-scaled Loschmidt echo crossing times $\log t_{\mathcal{L}_\times}$ emerges in families of $\mathcal{J}_{ij}$ populated by randomly selected angles from Gaussian and Triangular distributions (see Fig. G.2 and G.2) also constrained to lie within $[0.0, 0.5]$ radians. For the Gaussian $\mathcal{J}_{ij}$ family a second centroid emerged at $N = 6$, as it did in the Random Uniform $\mathcal{J}_{ij}$ family. Also as in the Random Uniform $\mathcal{J}_{ij}$ family, as N increased, the secondary centroid became progressively more pronounced as its amplitude a_2 increased while its spread σ_2 steadily decreased.

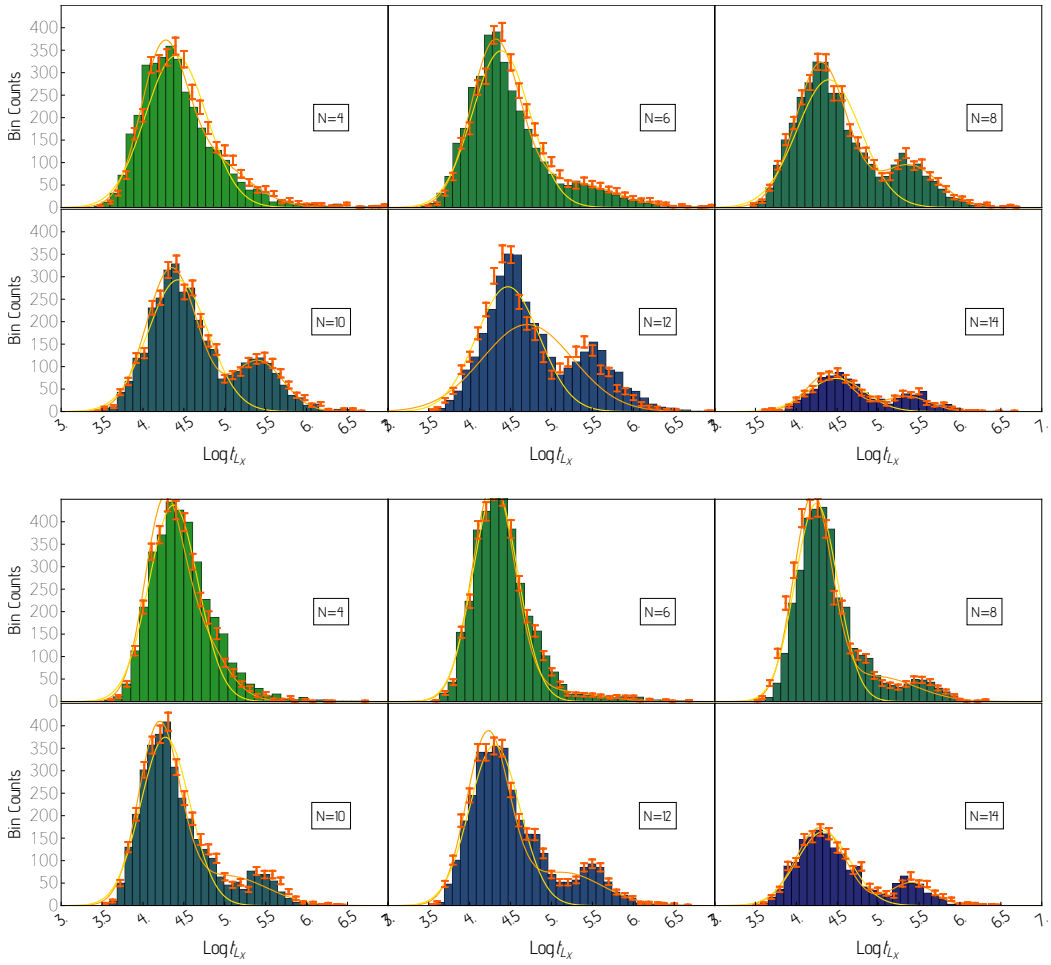

Figure G.2: Histograms of the Loschmidt echo crossing times are presented for system sizes of $N = 4, 6, 8, 10, 12$ & 14 neutrinos. The vertical axis measures the histograms bin counts (30 bins were used for each N) and the horizontal axis measures the $t_{\mathcal{L}_\times}$ in units of μ^{-1} on a log scale. For the topmost double panel, coupling angles for each neutrino flavor were randomly sampled from Gaussian distributions constrained to lie between $[0.0, 0.5]$ radians, with 3,500 unique $\mathcal{J}_{ij}$ configurations sampled for each N. For the bottommost double panel, coupling angles for each neutrino flavor were randomly sampled from Triangular distributions constrained to lie between $[0.0, 0.5]$ radians, with 3,500 unique $\mathcal{J}_{ij}$ configurations sampled for each N.
For both figures, dark orange bars denote standard errors, yellow curves show the result of a double Gaussian fit generated via Mathematica's NonlinearModelFit (NLMF) function.

With the distribution behavior of the Gaussian $\mathcal{J}_{ij}$ family consistent with the Random Uniform $\mathcal{J}_{ij}$ family, we understood this to also support the validity the the results witnessed from the Random Uniform $\mathcal{J}_{ij}$ family to not be distribution dependent. Further bolstering this were the consistent results from studying the Triangular $\mathcal{J}_{ij}$ family, where a second centroid in the $\log t_{\mathcal{L}_\times}$ histogram emerges at $N = 8$, and continues to grow in amplitude and whose σ_2 steadily decreased while N increased. These results suggested again–for a different $\mathcal{J}_{ij}$ distribution family–that the bimodal $\log t_{\mathcal{L}_\times}$ histogram behavior continues when taking N to the thermodynamic limit.

Appendix H

GELL-MANN MATRICES

Our notation for the Gell-Mann matrices is as follows,

$$\lambda_1 = \begin{pmatrix} 0 & 1 & 0 \\ 1 & 0 & 0 \\ 0 & 0 & 0 \end{pmatrix}, \ \lambda_2 = \begin{pmatrix} 0 & -i & 0 \\ i & 0 & 0 \\ 0 & 0 & 0 \end{pmatrix}, \ \lambda_3 = \begin{pmatrix} 1 & 0 & 0 \\ 0 & -1 & 0 \\ 0 & 0 & 0 \end{pmatrix},$$

$$\lambda_4 = \begin{pmatrix} 0 & 0 & 1 \\ 0 & 0 & 0 \\ 1 & 0 & 0 \end{pmatrix}, \ \lambda_5 = \begin{pmatrix} 0 & 0 & -i \\ 0 & 0 & 0 \\ i & 0 & 0 \end{pmatrix},$$

$$\lambda_6 = \begin{pmatrix} 0 & 0 & 0 \\ 0 & 0 & 1 \\ 0 & 1 & 0 \end{pmatrix}, \ \lambda_7 = \begin{pmatrix} 0 & 0 & 0 \\ 0 & 0 & -i \\ 0 & i & 0 \end{pmatrix},$$

$$\lambda_8 = \sqrt{\frac{1}{3}} \begin{pmatrix} 1 & 0 & 0 \\ 0 & 1 & 0 \\ 0 & 0 & -2 \end{pmatrix}. \tag{H.1}$$

Appendix I

QUTRIT GATES

This portion of the appendices writes the explicit matrix representation of the qutrit gates [223]. The single-qutrit gates used in the circuits described in the main text are [261]

$$X_{\alpha}^{12} = \begin{pmatrix} 1 & 0 & 0 \\ 0 & \cos\frac{\alpha}{2} & -i\sin\frac{\alpha}{2} \\ 0 & -i\sin\frac{\alpha}{2} & \cos\frac{\alpha}{2} \end{pmatrix} , \tag{I.1}$$

$$R_{y}^{01}(\alpha) = \begin{pmatrix} \cos\frac{\alpha}{2} & -\sin\frac{\alpha}{2} & 0 \\ \sin\frac{\alpha}{2} & \cos\frac{\alpha}{2} & 0 \\ 0 & 0 & 1 \end{pmatrix} , \tag{I.2}$$

$$R_{y}^{12}(\alpha) = \begin{pmatrix} 1 & 0 & 0 \\ 0 & \cos\frac{\alpha}{2} & -\sin\frac{\alpha}{2} \\ 0 & \sin\frac{\alpha}{2} & \cos\frac{\alpha}{2} \end{pmatrix} , \tag{I.3}$$

$$\mathrm{Ph}(\theta,\phi,\lambda) = \begin{pmatrix} e^{i\theta} & 0 & 0 \\ 0 & e^{i\phi} & 0 \\ 0 & 0 & e^{i\lambda} \end{pmatrix} , \tag{I.4}$$

$$R_{Z}^{01}(\theta) = \mathrm{Ph}(-\frac{\theta}{2},\frac{\theta}{2},0) , \tag{I.5}$$

$$R_{Z}^{12}(\phi) = \mathrm{Ph}(0,-\frac{\phi}{2},\frac{\phi}{2}) . \tag{I.6}$$

The two-qutrit CX gate, whose action is given by $CX\,|x,y\rangle = |x, \mathrm{mod}(x+y,3)\rangle$, implements the following operation,

$$CX = \begin{pmatrix} 1 & 0 & 0 & 0 & 0 & 0 & 0 & 0 & 0 \\ 0 & 1 & 0 & 0 & 0 & 0 & 0 & 0 & 0 \\ 0 & 0 & 1 & 0 & 0 & 0 & 0 & 0 & 0 \\ 0 & 0 & 0 & 0 & 1 & 0 & 0 & 0 & 0 \\ 0 & 0 & 0 & 0 & 0 & 1 & 0 & 0 & 0 \\ 0 & 0 & 0 & 1 & 0 & 0 & 0 & 0 & 0 \\ 0 & 0 & 0 & 0 & 0 & 0 & 0 & 0 & 1 \\ 0 & 0 & 0 & 0 & 0 & 0 & 1 & 0 & 0 \\ 0 & 0 & 0 & 0 & 0 & 0 & 0 & 1 & 0 \end{pmatrix} . \tag{I.7}$$

While the CX gate might not be a native two-qutrit gate on current qutrit quantum devices, it is straightforward to transform to alternative entangling gates, like the CZ gate [261],

$$CZ = \sum_{i,j\in\{0,1,2\}} \tilde{\omega}^{ij} |ij\rangle\langle ij| \ , \quad \tilde{\omega} = e^{i\frac{2\pi}{3}} \ . \tag{I.8}$$

Using the qutrit Hadamard gate [258], the CX gate can transformed into a CZ gate,

$$CZ = (1 \otimes H^\dagger) \cdot CX \cdot (1 \otimes H) \ , \quad H = \frac{1}{\sqrt{3}} \begin{pmatrix} 1 & 1 & 1 \\ 1 & \tilde{\omega} & \tilde{\omega}^2 \\ 1 & \tilde{\omega}^2 & \tilde{\omega} \end{pmatrix} \ , \tag{I.9}$$

with a similar transformation for $CX^\dagger$.

Appendix J

QUANTINUUM EMULATOR

Results from `H1-1` and its emulator for the four neutrino dynamics is reported in Fig. J.1 [223]. DR and the pHS post-selecting procedure were implemented in both cases. The emulator's results (empty symbols) were observed to be compatible with the `H1-1` device's results (solid symbols).

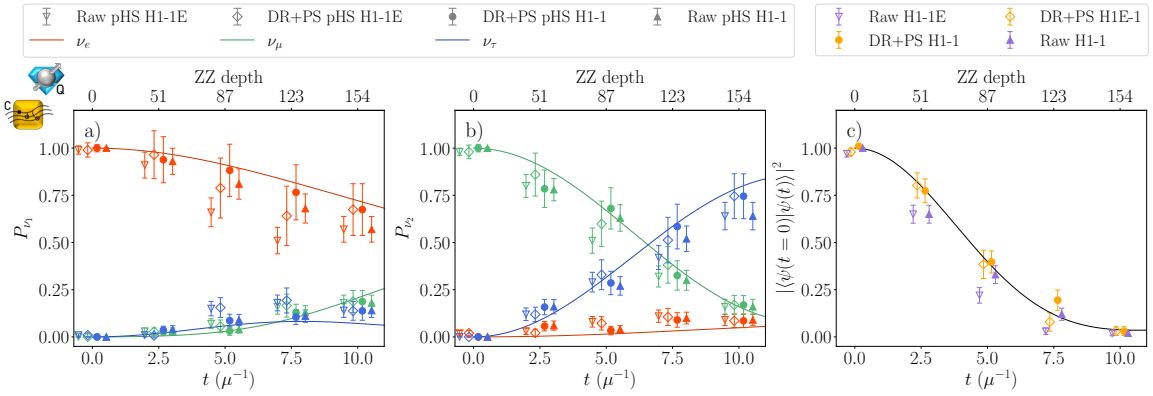

Figure J.1: Flavor evolution for four neutrinos as a function of time from the `H1-1E` emulator and `H1-1` device. Empty triangles and circles represent the emulator's raw and DR+PS results, respectively. Solid symbols show the corresponding results from `H1-1`. We use the same conventions as in Fig. 4.7.

Appendix K

SIMULATIONS OF EIGHT NEUTRINOS ON IBM QUANTUM COMPUTER

Figure K.1 shows the results from the evolution of eight neutrinos starting from the non-symmetric state $|\nu_e\nu_\mu\nu_e\nu_\tau\nu_e\nu_\mu\nu_e\nu_\tau\rangle$ [223]. Compared to the results in Fig. 4.11, the averaging procedure appears helpful for averaging out device errors. A clear example is the electron flavor evolution for the fourth neutrino, displayed in panel (b).

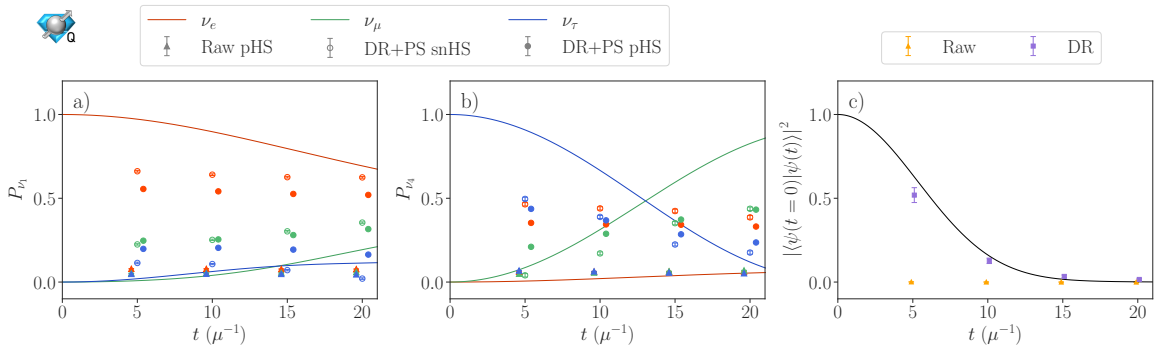

Figure K.1: Flavor evolution for eight neutrinos as a function of time obtained from the `ibm_torino` device, with $|\nu_e\nu_\mu\nu_e\nu_\tau\nu_e\nu_\mu\nu_e\nu_\tau\rangle$ as the initial state. Panels (a) and (b) show the flavor evolution of the first and fourth neutrinos, respectively. Panel (c) shows the persistence probability of the initial state. We use the same conventions as in Fig. 4.7.

Appendix L

DETAILS ABOUT THE TOMOGRAPHY STUDY

This App. contains details on the operator pool used to reconstruct the density matrix. Each row in Tables L.1, L.2, L.3 shows how to evaluate the coefficient c_i from Eq. (4.24) [223]. The second column contains the operator needed to change the basis in which to measure the two qubits. By measuring the state probability P_i with the expression in the third column, the value of c_i is recovered. Note that the operators for λ_3, λ_8, and λ_9 are identity operators, thus the operator pool is composed of 7 independent operators (instead of 9).

λ_i	Operator	Probability
λ_1	$\frac{1}{\sqrt{2}}\begin{pmatrix} 1 & 1 & 0 & 0 \\ 1 & -1 & 0 & 0 \\ 0 & 0 & \sqrt{2} & 0 \\ 0 & 0 & 0 & \sqrt{2} \end{pmatrix}$	$c_1 = \frac{1}{2}(P_{00} - P_{01})$
λ_2	$\frac{1}{\sqrt{2}}\begin{pmatrix} 1 & -i & 0 & 0 \\ 1 & i & 0 & 0 \\ 0 & 0 & \sqrt{2} & 0 \\ 0 & 0 & 0 & \sqrt{2} \end{pmatrix}$	$c_2 = \frac{1}{2}(P_{00} - P_{01})$

Table L.1: Tomographic pool for computing $c_i = \mathrm{Tr}(\rho\lambda_i)/\mathcal{A}_i$, where λ_i represents the Gell-Mann matrix. We perform the change of basis by implementing the operator shown in the second column. The coefficient c_i are then given by the linear combination of the obtained probabilities $P_{ij} = \{P_{00}, P_{01}, P_{10}, P_{11}\}$ given in the third column. This table contains the tomography pool for operators λ_1, λ_2.

The goal of the algorithm from Ref. [376] is to find the closest positive semi-definite

density matrix to the one obtained from `ibm_torino`. The general idea of the algorithm is to find the the density matrix ρ_{CpDM} that minimizes the trace distance with ρ_{IBM} while having all eigenvalues positive. This is done by shifting the eigenvalues of ρ_{IBM} using the algorithm of Ref. [439], while leaving the eigenvectors of ρ_{IBM} unmodified.

λ_i	Operator	Probability
λ_3	$\begin{pmatrix} 1 & 0 & 0 & 0 \\ 0 & 1 & 0 & 0 \\ 0 & 0 & 1 & 0 \\ 0 & 0 & 0 & 1 \end{pmatrix}$	$c_3 = \frac{1}{2}(P_{00} - P_{01})$
λ_4	$\frac{1}{\sqrt{2}}\begin{pmatrix} 1 & 0 & 1 & 0 \\ 0 & \sqrt{2} & 0 & 0 \\ 1 & 0 & -1 & 0 \\ 0 & 0 & 0 & \sqrt{2} \end{pmatrix}$	$c_4 = \frac{1}{2}(P_{00} - P_{10})$
λ_5	$\frac{1}{\sqrt{2}}\begin{pmatrix} 1 & 0 & -i & 0 \\ 0 & \sqrt{2} & 0 & 0 \\ 1 & 0 & i & 0 \\ 0 & 0 & 0 & \sqrt{2} \end{pmatrix}$	$c_5 = \frac{1}{2}(P_{00} - P_{10})$
λ_6	$\frac{1}{\sqrt{2}}\begin{pmatrix} \sqrt{2} & 0 & 0 & 0 \\ 0 & 1 & 1 & 0 \\ 0 & 1 & -1 & 0 \\ 0 & 0 & 0 & \sqrt{2} \end{pmatrix}$	$c_6 = \frac{1}{2}(P_{01} - P_{10})$

Table L.2: Tomographic pool for computing $c_i = \text{Tr}(\rho\lambda_i)/\mathcal{A}_i$, where λ_i represents the Gell-Mann matrix. We perform the change of basis by implementing the operator shown in the second column. The coefficient c_i are then given by the linear combination of the obtained probabilities $P_{ij} = \{P_{00}, P_{01}, P_{10}, P_{11}\}$ given in the third column. This table contains the tomography pool for operators $\lambda_3, \lambda_4, \lambda_5, \lambda_6$.

λ_i	Operator	Probability
λ_7	$\frac{1}{\sqrt{2}}\begin{pmatrix}\sqrt{2} & 0 & 0 & 0\\ 0 & 1 & -i & 0\\ 0 & 1 & i & 0\\ 0 & 0 & 0 & \sqrt{2}\end{pmatrix}$	$c_7 = \frac{1}{2}(P_{01} - P_{10})$
λ_8	$\begin{pmatrix}1 & 0 & 0 & 0\\ 0 & 1 & 0 & 0\\ 0 & 0 & 1 & 0\\ 0 & 0 & 0 & 1\end{pmatrix}$	$c_8 = \frac{1}{2\sqrt{3}}(P_{00} + P_{01} - 2\,P_{10})$
λ_9	$\begin{pmatrix}1 & 0 & 0 & 0\\ 0 & 1 & 0 & 0\\ 0 & 0 & 1 & 0\\ 0 & 0 & 0 & 1\end{pmatrix}$	$c_9 = \frac{1}{3}(P_{00} + P_{01} + P_{10})$

Table L.3: Tomographic pool for computing $c_i = \mathrm{Tr}(\rho\lambda_i)/\mathcal{A}_i$, where λ_i represents the Gell-Mann matrix. We perform the change of basis by implementing the operator shown in the second column. The coefficient c_i are then given by the linear combination of the obtained probabilities $P_{ij} = \{P_{00}, P_{01}, P_{10}, P_{11}\}$ given in the third column. This table contains the tomography pool for operators $\lambda_7, \lambda_8, \lambda_9$.

Appendix M

DEVICE PARAMETERS

This appendix contains the experimental parameters of the quantum computers used in the work contained in Chapter 4 [223]. Table M.1, contains the Quantinuum `H1-1` device parameters and Table M.2, contains the IBM `ibm_torino` device parameters.

Total number of qubits	20
Typical Single-qubit gate infidelity	$2 \cdot 10^{-5}$
Typical Two-qubit gate infidelity	$1 \cdot 10^{-3}$
SPAM error	$2 \cdot 10^{-4}$

Table M.1: Quantinuum H1-1 device parameters (Ref. [3]).

Total number of qubits	133		
Neutrinos	2	4	8
Date accessed	6/12/24	6/21/24	6/25/14
Number of qubits used	4	8	16
Median T1 coherence time (μs)	150	133	142
Median T2 coherence time (μs)	147	127	151
Median X-gate error	$3.2 \cdot 10^{-4}$	$3.3 \cdot 10^{-4}$	$2.8 \cdot 10^{-4}$
Median CZ-gate error	$9.4 \cdot 10^{-3}$	$7.8 \cdot 10^{-3}$	$4.0 \cdot 10^{-3}$
Median readout error	$2.6 \cdot 10^{-2}$	$2.9 \cdot 10^{-2}$	$2.3 \cdot 10^{-2}$

Table M.2: IBM `ibm_torino` device parameters.